

X-Shooting ULLYSES: Massive stars at low metallicity

V. Effect of metallicity on surface abundances of O stars

F. Martins¹, J.-C. Bouret², D.J. Hillier³, S.A. Brands⁴, P.A. Crowther⁵, A. Herrero^{6,7}, F. Najarro⁸, D. Pauli⁹, J. Puls¹⁰,
V. Ramachandran¹¹, A.A.C. Sander¹¹, J.S. Vink¹², and the XshootU collaboration

¹ LUPM, Université de Montpellier, CNRS, Place Eugène Bataillon, F-34095 Montpellier, France

² Aix-Marseille Univ, CNRS, CNES, LAM, Marseille, France

³ Department of Physics and Astronomy & Pittsburgh Particle Physics, Astrophysics and Cosmology Center (PITT PACC), University of Pittsburgh, 3941 O'Hara Street, Pittsburgh, PA 15260, USA

⁴ Astronomical Institute Anton Pannekoek, University of Amsterdam, Science Park 904, 1098 XH, Amsterdam, The Netherlands

⁵ Dept of Physics & Astronomy, University of Sheffield, Hounsfield Road, Sheffield S3 7RH, UK

⁶ Instituto de Astrofísica de Canarias, C. Vía Láctea, s/n, 38205 La Laguna, Tenerife, Spain

⁷ Departamento de Astrofísica, Universidad de La Laguna, Avenida Astrofísico Francisco Sánchez, s/n, 38205 La Laguna, Tenerife, Spain

⁸ Departamento de Astrofísica, Centro de Astrobiología (CSIC-INTA), Ctra. Torrejón a Ajalvir km 4, 28850, Torrejón de Ardoz, Spain

⁹ Institut für Physik und Astronomie, Universität Potsdam, Karl-Liebknecht-Str. 24/25, 14476 Potsdam, Germany

¹⁰ LMU München, Universitäts-Sternwarte, Scheinerstr. 1, 81679 München, Germany

¹¹ Zentrum für Astronomie der Universität Heidelberg, Astronomisches Rechen-Institut, Mönchhofstr. 12-14, 69120 Heidelberg, Germany

¹² Armagh Observatory and Planetarium, College Hill, BT61 9DG Armagh, UK

Received / Accepted

ABSTRACT

Context. Massive stars rotate faster, on average, than lower mass stars. Stellar rotation triggers hydrodynamical instabilities which transport angular momentum and chemical species from the core to the surface. Models of high-mass stars that include these processes predict that chemical mixing is stronger at lower metallicity.

Aims. We aim to test this prediction by comparing the surface abundances of massive stars at different metallicities.

Methods. We performed a spectroscopic analysis of single O stars in the Magellanic Clouds (MCs) based on the ULLYSES and XshootU surveys. We determined the fundamental parameters and helium, carbon, nitrogen, and oxygen surface abundances of 17 LMC and 17 SMC non-supergiant O6-9.5 stars. We complemented these determinations by literature results for additional MCs and also Galactic stars to increase the sample size and metallicity coverage. We investigated the differences in the surface chemical enrichment at different metallicities and compared them with predictions of three sets of evolutionary models.

Results. Surface abundances are consistent with CNO-cycle nucleosynthesis. The maximum surface nitrogen enrichment is stronger in MC stars than in Galactic stars. Nitrogen enrichment is also observed in stars with higher surface gravities in the SMC than in the Galaxy. This trend is predicted by models that incorporate chemical transport caused by stellar rotation. The distributions of projected rotational velocities in our samples are likely biased towards slow rotators.

Conclusions. A metallicity dependence of surface abundances is demonstrated. The analysis of larger samples with an unbiased distribution of projected rotational velocities is required to better constrain the treatment of chemical mixing and angular momentum transport in massive single and binary stars.

Key words. Stars: massive – Stars: fundamental parameters – Stars: abundances – Stars: evolution

1. Introduction

Stars more massive than $8 M_{\odot}$ evolve beyond the core carbon-burning phase and produce most metals heavier than oxygen and up to the iron group (Chiosi & Maeder 1986; Langer 2012). They are hot and consequently produce photons that can ionise hydrogen and heavier elements. They drive strong stellar winds (Puls et al. 2008; Vink 2022). Massive stars are thus important sources of feedback in terms of chemistry, energetics, and ionising flux. Their explosions as core-collapse supernovae leave

compact objects that may merge to produce gravitational wave events (Abbott et al. 2021). Understanding their properties and evolution is relevant for many astrophysical fields (Massey 2013; Eldridge & Stanway 2022).

Spectroscopic analysis of massive stars provides their present-day fundamental parameters. It requires sophisticated atmosphere models that include a non-LTE treatment of radiative transfer, spherical extension caused by stellar winds, and line-blanketing to account for the effects of metals on the atmospheric structure and emergent spectrum (Hillier & Miller 1998; Puls et al. 2005; Sander et al. 2015).

Variations in surface abundances while stars evolve probe the efficiency of mixing processes in stellar interior. The products

Send offprint requests to: Fabrice Martins
e-mail: fabrice.martins@umontpellier.fr

of nucleosynthesis in the core are transported to the surface by these mechanisms. During the main-sequence it is mainly helium, carbon, nitrogen, and oxygen that are affected since nucleosynthesis takes place through the CNO-cycle. Among other processes stellar rotation triggers instabilities that transport of both angular momentum and chemical species. The implementation of these mixing processes in stellar evolution codes has led to the prediction of three main trends with physical parameters (e.g. Meynet & Maeder 2000; Brott et al. 2011a): first, stars rotating faster transport more efficiently chemical species from their core to their surface; second, mixing is more efficient in more massive stars; third, stars with a lower metal content are more chemically processed at their surface.

Hunter et al. (2008a) and Hunter et al. (2009) investigate the relation between surface nitrogen enrichment and rotational velocity in B-type stars of the SMC, LMC, and Galaxy. They report a general trend of higher nitrogen content for higher projected rotational velocity, but also stress that a number of objects are chemically enriched while rotating slowly. Simulations of stellar populations based on the evolutionary tracks of Brott et al. (2011a) indicate a difficulty for these tracks to account for these slowly rotating N-rich B stars. Qualitatively similar results are found for additional objects: the LMC O stars studied by Rivero González et al. (2012) and Grin et al. (2017), the LMC B dwarfs and giants analysed by Dufton et al. (2018), and the SMC B stars studied by Dufton et al. (2020) all show a fraction of chemically enriched slow rotators that the models of Brott et al. (2011a) can not explain. Alternatively Martins et al. (2015) and Martins et al. (2017) find that the tracks computed by Ekström et al. (2012) can reproduce most of the Galactic stars they studied, although some outliers exist. These analyses are not based on population synthesis though, so a quantitative assessment of the ability of these models to explain the chemical and rotational properties of Galactic O stars remains to be performed. Using a similar approach, Bouret et al. (2013) and Bouret et al. (2021) reach the same qualitative conclusion for SMC O stars: models from Georgy et al. (2013) can account for the abundances and rotational velocities of most of the O stars. There are two main things that would advance these analyses. First, a systematic investigation of the differences in the predictions of various evolutionary models needs to be performed. Second, proper population synthesis simulations for all types of evolutionary models (i.e. models that include rotational mixing with different prescriptions, as well as binary models) are required before the relation between surface chemical enrichment and rotational velocity can be quantitatively probed.

Regarding the effect of stellar mass on chemical enrichment, Martins et al. (2017) report an average increase by ~ 0.7 dex in surface nitrogen enrichment between Galactic B and O stars, based on their spectroscopic analysis of late O giants and the results of Hunter et al. (2009) and Nieva & Przybilla (2012). In the SMC Bouret et al. (2021) confirm that more massive O stars have a higher N/C ratio than less massive ones.

Bouret et al. (2021) also performed a principal component analysis based on the abundances of C, N, and O in stars of the SMC and the Milky Way. They report a trend of more efficient mixing at lower metallicity, as predicted. However the significance of the results is limited mostly by the limited size of the SMC sample which is not commensurate to the reference Galactic sample.

The physical understanding of this metallicity effect is the following. Early simulations of the evolution of low metallicity stars showed that the zero-age main-sequence (ZAMS) is displaced to the blue part of the Hertzsprung-Russell (HR) di-

agram compared to solar metallicity stars (El Eid et al. 1983; Bertelli et al. 1984; Schaller et al. 1992). The reduction of the metal content, especially the CNO abundances, leads to a reduced energy release by the CNO cycle and thus to a reduced pressure support. As a consequence, stars contract until the associated temperature increase boosts the efficiency of the CNO cycle providing the extra energy release necessary to recover hydrostatic equilibrium. Therefore stars are more compact at low metallicity (e.g. Fig. 1 of Ekström et al. 2008).

Chemical transport is affected by the change in the structure of the star at low metallicity. It is dominated by horizontal shear turbulence and treated as a diffusive process, parameterised by a coefficient D_{shear} , in evolutionary calculations. D_{shear} is proportional to the gradient of the angular velocity (see Eq. 16 of Meynet & Maeder 2000). At lower metallicity this gradient is stronger, since the star is more compact, and consequently chemical transport is more efficient (Maeder & Meynet 2001; Meynet & Maeder 2002; Brott et al. 2011a; Georgy et al. 2013). In particular chemical enrichment or depletion, depending on the species, is stronger at the surface of low metallicity stars.

In this study we further investigate the metallicity dependence of chemical transport caused by stellar rotation. We leverage on the availability of homogeneous data – in terms of spectral coverage and instruments used – from the ULLYSES¹ (Roman-Duval et al., in prep.) and XshootU² (Vink et al. 2023) surveys that provide UV and optical spectroscopy of about 200 massive stars in the Magellanic Clouds (MCs). We determine the surface abundance of He, C, N, and O for a sample of O stars in the MCs. We complement these abundances by those of published studies in the MCs and the Galaxy. We very much emphasise that our goal is not to interpret the surface properties of large samples of stars that could probe all types of mixing and transport processes taking place in all possible sorts of massive stars (single and binary). We merely want to test if stars at different metallicities have different surface chemical composition, as predicted by models that include mixing caused by stellar rotation.

2. Samples and method

2.1. Samples

The primary goal of this study is to investigate the metallicity dependence of chemical mixing. For that we relied on samples of stars in the SMC, the LMC, and the Galaxy. The SMC and LMC samples were partly built from the XshootU and ULLYSES surveys. Complementary stars were selected to increase the sample sizes (see below). To avoid the effect of mass on surface abundances to be present in our analysis, we selected stars in a relatively narrow mass range.

2.1.1. XshootU sample

We selected O6 to O9.5 objects from the XshootU sample, i.e. stars with an X-shooter spectrum. We excluded stars for which the presence of a companion was clear from the spectra (presence of double sets of lines). The sample is made of 17 stars in both the LMC and the SMC. We avoided luminous supergiants because no large enough Galactic sample of such objects was available for comparisons of surface abundances at the time of the present study. Only a few class I stars were included because

¹ <https://ullyses.stsci.edu/>

² X-shooting ULLYSES - <https://massivestars.org/xshootu/>

their stellar parameters are similar to giants and bright giants (luminosity classes III and II) of the sample (see Sect. 3.1). In the following we will refer to these MC samples as the XshootU samples. The members of the samples are listed in Tables 1 and 2. The observational data for this sample is described at length in Vink et al. (2023). The optical spectra were retrieved from the XshootU database presented by Sana et al. (2024). They have a spectral resolution of about 7000 and a signal-to-noise ratio (SNR) of about 200. The UV spectra were downloaded from the MAST archive³. Their spectral resolution is ~ 15000 and the SNR of the order 100. Spectra were manually normalised by choosing spectral regions free of lines and applying a spline cubic function to define the continuum.

We stress that the spectral types and luminosity classes listed in Tables 1 and 2 have been collected from literature. Some are based on poor quality data and are likely uncertain. A complete revision of spectral classification of the entire ULLYSES samples will be provided in a subsequent publication of the series (Maíz Apellániz et al., in prep.). Spectral types can be used to infer coarse stellar parameters, but stars with similar parameters can have different spectral types and luminosity classes (Simón-Díaz et al. 2014; Martins & Palacios 2017). In addition spectral classification depends on metallicity since some of the classification criteria depend on wind sensitive lines (and thus on the metal content) and on metallic lines (Sota et al. 2011; Martins 2018; Martins & Palacios 2021). For the present study the accuracy of spectral classification is not an issue since we aim at obtaining homogeneous samples in terms of evolutionary state. We demonstrate in the following that this goal is achieved.

2.1.2. Literature samples

To increase the number of stars for which surface abundances are determined, we complemented our results with those of Bouret et al. (2013), Bouret et al. (2021), and Grin et al. (2017). The former two studies include SMC stars while the latter study focuses on LMC targets. All stars are presumably single. We included only stars that cover the same region of the $\log g - T_{\text{eff}}$ diagram as the XshootU samples. By doing so we ensured that we kept a relatively narrow mass range for the entire sample, thus minimising the effect of mass on surface abundances as explained above (see also Sect. 3.1).

In addition to literature results in the MCs we also considered stars in the Galaxy to extend the metallicity range over which abundances can be compared. We selected stars from the studies of Martins et al. (2015), Martins et al. (2017), Cazorla et al. (2017), and Markova et al. (2018). As for the complementary stars in the MCs, the Galactic stars were chosen to cover the same mass range as the XshootU samples. The position of the sample stars in evolutionary diagrams will be discussed in Sect. 3.1. These various samples defined from the literature will be referred as the complementary samples in the remainder of the manuscript. The members of these additional samples are given in Table A.1. We stress that we did not re-determine the fundamental stellar parameters and surface abundances for these stars, but took the values published in the studies listed in Table A.1. The methods adopted by Bouret et al. (2013), Martins et al. (2015), Martins et al. (2017), and Bouret et al. (2021) are very similar to the one used in the present study. In particular they rely on the code CMFGEN. Grin et al. (2017) and Markova et al. (2018) use atmosphere models and synthetic

spectra computed with the code FASTWIND (Puls et al. 2005; Rivero González et al. 2011) and rely on optical spectra only.

2.2. Stellar parameters

For the present study we determined the surface parameters of the stars in the XshootU samples. We performed a spectroscopic analysis with the atmosphere code CMFGEN (Hillier & Miller 1998). Non-LTE radiative transfer is performed in a spherical geometry. Stellar winds are included by connecting a pseudo-hydrostatic velocity structure to a β velocity law⁴. Line-blanketing is taken into account. Once the atmosphere model has converged, a formal solution of the radiative transfer is performed and leads to the emergent spectrum that can be compared to observational data to infer stellar parameters. We proceeded as follows in the present analysis.

We relied on two grids of models designed to cover the main sequence and early-post main-sequence in the LMC and SMC, respectively. The grids will be presented in Marcolino et al. (in prep.) and we refer the reader to this publication for details. Models in the grids all assume a microturbulent velocity (v_{turb}) of 10 km s^{-1} in the photosphere and a fixed chemical composition⁵, that is scaled solar abundances from Asplund et al. (2009) assuming a metallicity of $1/2$ and $1/5 Z_{\odot}$ for the LMC and SMC respectively. The steps in T_{eff} and $\log g$ are 1000 K and 0.1 dex . Mass loss rates are from Vink et al. (2001) and no clumping is taken into account.

The first step of the analysis was the determination of the projected rotational velocity ($V \sin i$) and of the macroturbulent velocity (v_{mac}). For this we used the Fourier transform method (Gray 1976; Simón-Díaz & Herrero 2007) to isolate $V \sin i$. We relied on He I 4713⁶, and when present on Si III 4553. Once obtained, we estimated the effective temperature and surface gravity of the star from its spectral type using the calibration of Martins et al. (2005). We then selected the model from the grid with the closest parameters to these values. We convolved it by a rotational profile parameterised by $V \sin i$. Convolution by a Gaussian profile was also performed to account for instrumental resolution. Finally we also included a convolution by a radial-tangential profile to take macroturbulence into account (Simón-Díaz & Herrero 2014). We then compared the resulting line profile of He I 4713 or Si III 4553 to the observed profile and select v_{mac} that best reproduced the line shape, especially the far wings. The typical uncertainties on the measurements of $V \sin i$ and v_{mac} are 10 and 20 km s^{-1} respectively.

Once obtained the values of $V \sin i$ and v_{mac} were adopted to convolve the entire grids of synthetic spectra. This yielded theoretical spectra that can be quantitatively compared to the observed ones to estimate the stellar parameters. For that purpose we selected various sets of lines that are sensitive to T_{eff} and $\log g$. For the chosen set of lines a χ^2 analysis was performed allowing us to determine the best fit value and the uncertainties. The lines we used are the following:

- Effective temperature: we relied entirely on helium lines. For the spectral types we considered, both He I and He II

⁴ $v = v_{\infty} \times (1 - R/r)^{\beta}$, v being the velocity, R the stellar radius, and r the radial coordinate

⁵ This implies that He/H is kept constant in the determination of the effective temperature.

⁶ This line is broadened by the Stark effect, but in most cases it is the only clean line available for the determination of $V \sin i$. Alternative lines usually considered for the determination of $V \sin i$ are Si III lines that are at best weak in the spectrum of the stars we consider here

³ <https://archive.stsci.edu/hlsp/ullyses>

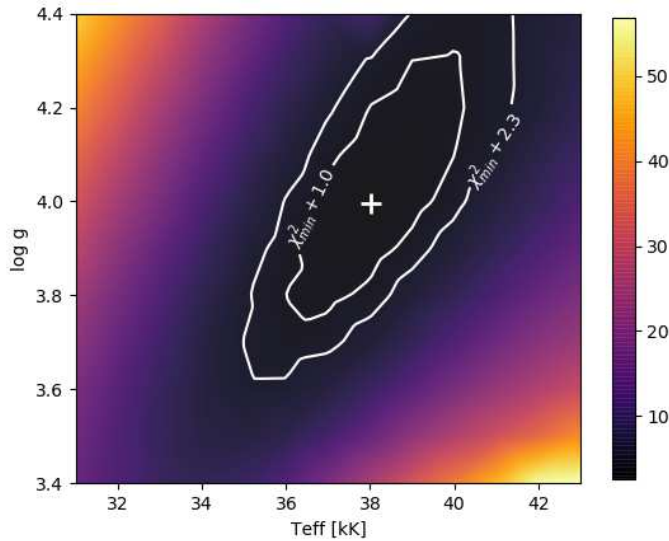


Fig. 1. Example of determination of T_{eff} and $\log g$ for star AV207 in the SMC. The colour scale indicates the value of the χ^2 function. The 1 and 2.3 σ contours are shown by the white lines. The white cross marks the minimum of the χ^2 function.

features are present in the spectra so the ionisation balance method can be robustly used. The full set of lines that can be potentially used is: He I 4026, He I 4143, He II 4200, He I 4388, He I 4471, He II 4542, He I 4713, He I 4920, He II 5412, He I 5876, He I 6678, He I 7065. Given the predominance of He I lines in this list, we gave more weight to the He II in order to avoid that the results are systematically biased towards low T_{eff} . The weight can be adjusted and we found that the results depend little on its value. A value of 2 was adopted for the present analysis.

- Surface gravity: the wings of Balmer lines were the main indicators as is customary for OB-type stars. We relied on H δ , H ϵ , H δ , H γ , H β .

The set of helium and hydrogen lines we used depended on the target. Data quality was sometimes insufficient to clearly isolate the line profile of a particular line. Nebular contamination may affect some lines. In addition depending on the position in the parameter space, some lines were too weak to be used. Fig. 1 shows an example of the determination of T_{eff} and $\log g$. We see that the two parameters are highly correlated and so are their error bars. This is expected since our method relies on the measurement of the ionisation balance at the atmospheric depth where lines are formed, and ionisation depends on both temperature and density, hence gravity. For these reasons we do not quote formal errors on T_{eff} and $\log g$ but refer to Fig. 1 for representative values. In the following we adopt the $\chi^2_{\text{min}} + 1.0$ contour as representative of our error measurements.

The luminosity was subsequently adjusted for the fixed set of T_{eff} and $\log g$. We computed the bolometric corrections associated to the effective temperature (Martins & Plez 2006), the extinction from the colour excess $E(B-V)$ and determined the luminosity from the assumed distance and the photometry of each star, taken from Table B.1 of Vink et al. (2023). We did not determine wind properties (mass loss rates, wind terminal velocity, and clumping) that will be investigated in other publications of the XshootU series. We simply assumed the classical mass loss rates of Vink et al. (2001). At the metallicity of the LMC and SMC the winds remain weak enough not to affect most photospheric lines used in the present study.

The results of the present analysis are summarised in the first columns of Tables 1 and 2. In those Tables we also provide the surface gravity corrected for the effect of centrifugal acceleration, $g_c = g + \frac{V \sin^2 i}{R}$. When $V \sin i$ is large the difference between $\log g$ and $\log g_c$ can reach almost 0.2 dex as in the case of AzV 251. The best fits are given in appendix D.

2.3. Surface abundances

Once the fundamental stellar parameters were determined we moved on to the investigation of the surface abundances. We considered helium, carbon, nitrogen, and oxygen. Abundances were determined from the fit of selected lines. Line strength depends on many parameters which control the level populations of the upper and lower levels of the transitions, as well as the intensity of the radiation field at the transition's wavelength. Ionisation and excitation processes, whether collisional or radiative, are partly fixed when the temperature and gravity are determined. Radiation field is affected by opacities that depend on elemental abundances. All of this sets the level populations. The line intensity further depends on broadening mechanisms, in particular the turbulent ones. Macroturbulence was constrained in the early phase of the analysis (see above) but microturbulence was not. We constrained it in parallel to surface abundances, in the same spirit as that of the curve of growth method (e.g. Simón-Díaz 2020).

We proceeded as follows. Adopting the stellar parameters previously determined, we ran new CMFGEN models varying the abundances and v_{turb} . For the latter, we used values of 5, 10, 15, and 20 km s⁻¹. We computed the synthetic spectrum for each of these values, and for various abundances. Typically five sets of abundances with a ratio of 50 to 100 between the smallest and largest values were selected. Both new atmosphere models and synthetic spectra were computed with additional sets of abundances, while microturbulence was changed only in the formal solution of the radiative transfer leading to the synthetic spectrum. For each of these new models we quantified the goodness of fit of individual lines of a given element by means of a χ^2 analysis. For each line and for a given microturbulent velocity we determined the abundance leading to the best fit. The resulting abundance measurements had a dispersion (among various lines) that depended on the adopted microturbulence. We then adopted the final v_{turb} that lead to the smallest dispersion and for that value, we fixed the final abundance by taking the average of the individual line determinations. The uncertainty was set to the dispersion of the measurements. When two values of v_{turb} gave similar results the final choice was made by visually inspecting the fits and selecting by eye the most relevant value. An example of this process is given in Fig. 2. In that case both $v_{\text{turb}} = 10$ and 15 km s⁻¹ (the sets of red and blue points) lead to similar dispersion. The first value was adopted from the final fit (see bottom panel of Fig. D.3). We stress that uncertainties in the fundamental parameters are not propagated into error on the abundance measurement, because of our method. This should not significantly affect our estimate of uncertainties on surface abundances, as was discussed by Martins et al. (2012) and Martins et al. (2015).

The set of lines used for the abundance determination depended on the star, the data quality and the robustness of the normalisation. Here is the list of lines that were considered:

- helium: He I 4026, He II 4200, He I 4388, He I 4471, He II 4542, He I 4713, He I 4920, He II 5412, He I 5876, He I 6678, He I 7065

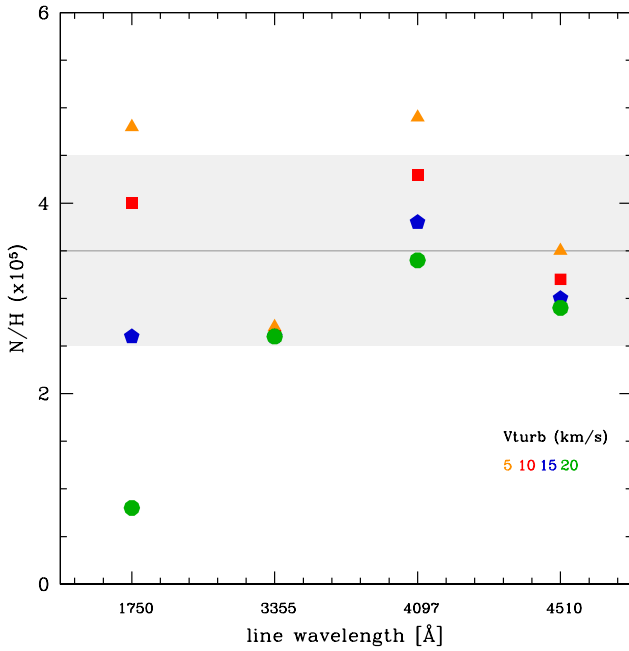


Fig. 2. Example of determination of the nitrogen abundance and v_{turb} for star AV47. The horizontal axis shows the wavelengths of the different nitrogen lines used, labelled by their wavelength. The vertical axis gives the best fitting abundance (N/H by number) for each line. Different symbols and colours correspond to different microturbulent velocities. All points for line N III 3355 overlap. The grey line and area highlight the final abundance value and its uncertainty. See text for discussion.

- carbon: C IV 1169, C III 1176, C III 4068-70
- nitrogen: N III 1183-85, N III 1748-52, N IV 3478-83, N III 3355, N III 4097, N III 4510-20
- oxygen: O IV 1339, O IV 1343, O III 3261, O III 3265, O III 3760, O III 3963, O III 5593

We excluded N III 4634-40-42, C III 4647-50-51, and C III 5696 from the analysis because these lines have been shown to depend critically on atomic data, line-blanketing, and stellar winds (Rivero González et al. 2011; Martins & Hillier 2012). We also excluded strong resonance lines (N V 1240 and C IV 1550) that depend on X-ray emission and mainly on wind parameters (Pauldrach et al. 1994). In addition they are often saturated (at least for LMC stars) and thus not sensitive to abundance variations.

The results of the abundance analysis are gathered in Table 1 and 2. The bottom panels of the figures shown in appendix D highlight the fits to lines from carbon, nitrogen, and oxygen.

2.4. Comparison to previous studies

Table B.1 gathers the results from previous studies for some stars of our XshootU sample. Effective temperatures agree very well for all stars. The dispersion is usually about 1000 K or even less. Surface gravities can differ significantly but in that case it is mainly due to the adoption of $\log g$ in some studies. For instance, Bouret et al. (2013) fixed $\log g$ when no optical spectra was available. This is the case for AzV446: Bouret et al. adopted $\log g = 4.0$ as a classical value for dwarfs, while the use of Balmer lines to measure $\log g$ leads to higher values for the present study and for Massey et al. (2005). AzV47 is an exception since optical spectra are available in all studies that included

that star. We found that the UVES spectrum used by Bouret et al. (2021) is quite different from the X-shooter spectrum we used in the present analysis. In particular the Balmer lines are narrower in the former study, explaining the lower surface gravity (3.75 vs 4.3). The reason for this difference is not clear. One can only speculate that normalisation issues and low SNR cause most of it.

Luminosities are consistent between various studies, with differences of the order 0.1 dex, at most 0.2 dex. Some differences are seen in the determination of projected rotational velocities. Large discrepancies are explained by macroturbulence: studies that do take it into account provide lower $V \sin i$ than studies that assume rotation incorporates all the macro-broadening mechanisms.

Helium surface abundance determinations are usually consistent in the sense that when a star is He-rich, all studies agree on enrichment, and when it is not, all studies also agree that it is not. Two exceptions are AzV95 and AzV243 for which Mokiem et al. (2006) find an enrichment in He while both Bouret et al. (2013) and the present study do not find evidence for enrichment.

Carbon, nitrogen, and oxygen abundances have been mostly determined by Bouret et al. (2013, 2021), in addition to the present study. Only a few other determinations exist for some of the XshootU sample stars. In general abundances are consistent within the error bars between the results of Bouret et al. and the present ones. However, some differences may exist. For instance, the carbon content of AzV15 differs by almost 0.5 dex between both studies. Similarly the surface nitrogen abundance of AzV47 is ~ 0.4 dex higher in the present analysis than in Bouret et al. This stresses that using the same atmosphere models, the same fitting strategy (χ^2 analysis) but slightly different observational sets and spectral lines can affect the final values. This highlights that when discussing surface abundances, general trends are more robust than individual measurements.

3. Surface abundances and metallicity

In this section we present our results and discuss how they compare to predictions of stellar evolution for single stars with rotation. We focus on the variation of surface chemistry with metallicity. We discuss the results using three sets of evolutionary models: the Geneva models (Ekström et al. 2012; Georgy et al. 2013; Eggenberger et al. 2021), the Bonn models (Brott et al. 2011a - see also Szécsi et al. 2022 for interpolated tracks), and the Stromlo models (Grasha et al. 2021). Other models calculated with alternative stellar evolution codes exist in the literature. Those of Limongi & Chieffi (2018) do not cover the SMC and LMC metallicity, and are not considered here. The three sets of models include stellar rotation using different formalisms, and we refer the reader to the original publications listed above for the details. In short the main differences are a purely diffusive approach for the treatment of angular momentum transport in the Bonn and Stromlo models, while an advecto-diffusive scheme is implemented in the Geneva models. In addition, the Bonn models include the effect of magnetic field on angular momentum transport (but not on chemical mixing). Finally different models assume different degree of core-overshooting that affect the shape of evolutionary tracks, as well as different initial values of carbon, nitrogen, and oxygen abundances.

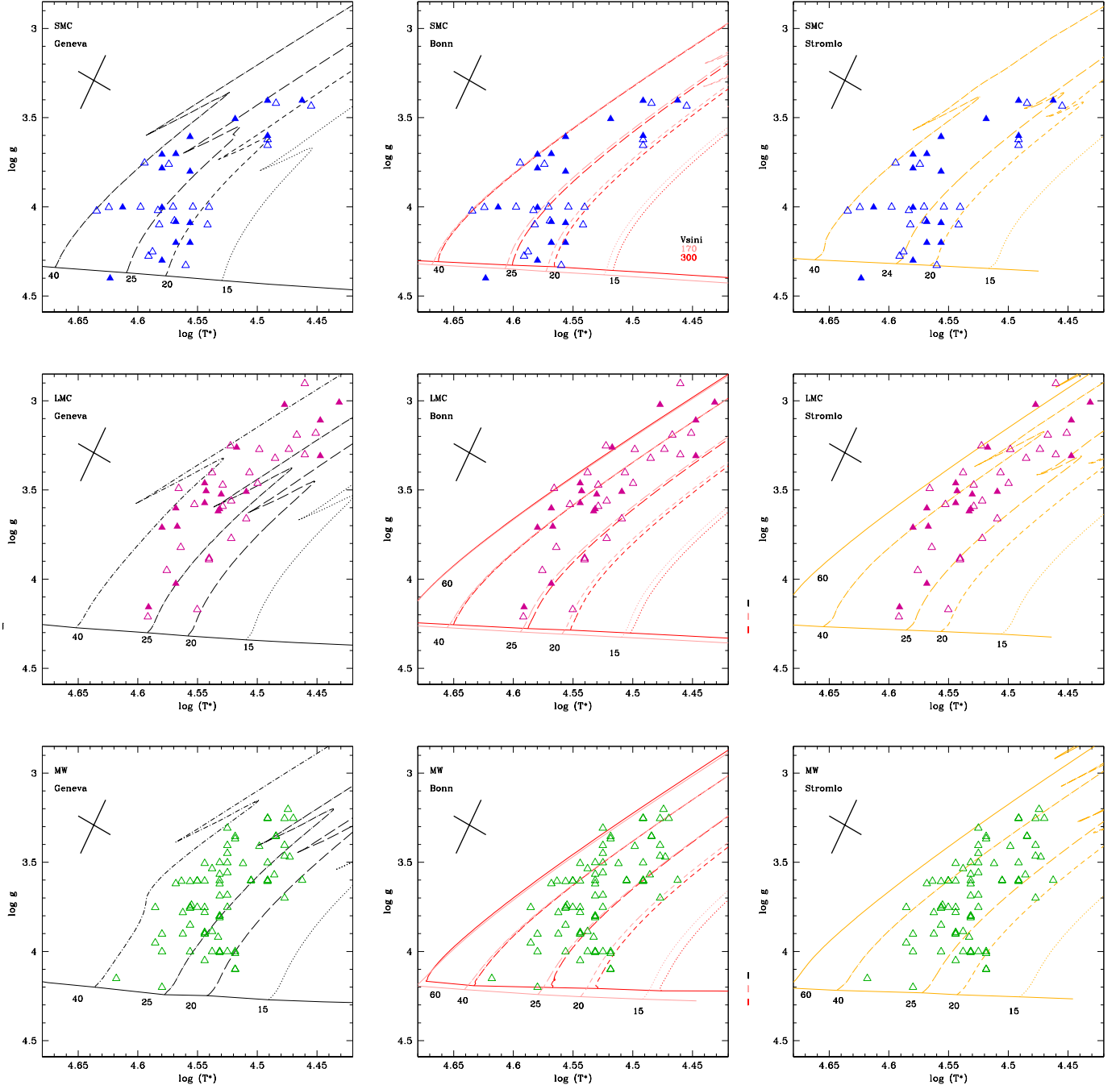


Fig. 3. $\log T_{\text{eff}} - \log g$ diagram for SMC (LMC, Galactic) sample stars in the top (middle, bottom) panels. Filled (open) symbols are for the XshootU (complementary) sample. Left panels are for Geneva tracks (Eggenberger et al. (2021) for the LMC, Georgy et al. 2013 for the SMC, and Ekström et al. (2012) for the Galaxy), middle panels for tracks from Brott et al. (2011a), and right panels for tracks from Grasha et al. (2021). We show tracks for initial rotational velocities of about 300 km s^{-1} and, in the case of those of Brott et al., also 170 km s^{-1} (in pink). Surface gravity has been corrected for the effect of rotation in the sample stars. The cross in each panel indicates typical error bars that are taken from Fig. 1.

3.1. Evolutionary diagrams

Figure 3 shows the $\log T_{\text{eff}} - \log g$ diagram for the XshootU and complementary sample stars. We overplot evolutionary tracks to provide a qualitative estimate of the mass and evolutionary state of the stars. In the three galaxies the sources are located on a relatively narrow band from the ZAMS to the end of the main-sequence. The SMC stars have initial masses between 20 and $40 M_{\odot}$ independently of the choice of the tracks used for com-

parison. In the LMC and the Galaxy, the Geneva tracks indicate a similar initial mass range while the Bonn and Stromlo tracks favour a wider mass range, from 20 to $60 M_{\odot}$.

The inferred evolutionary status of the stars depends much more on the choice of the tracks. If we simply separate stars into two categories whether they are on the main sequence (MS) or beyond it, we find that in the Milky Way all stars fall in the first category. In the LMC, the morphology of the Geneva and Stromlo tracks imply that a fraction of the stars are post-MS ob-

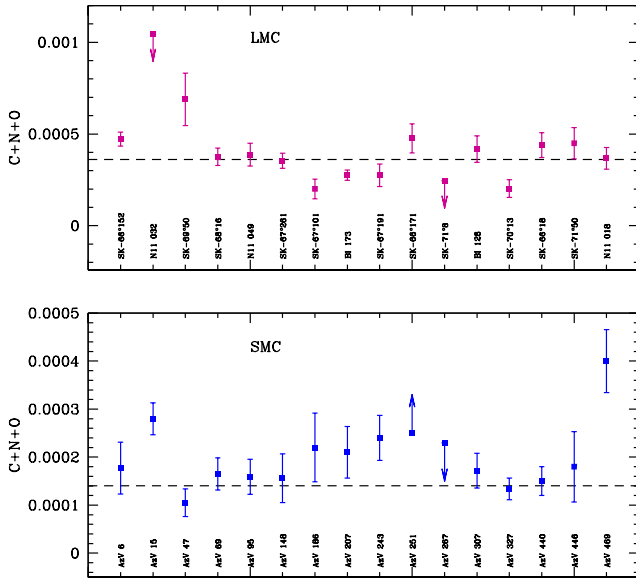


Fig. 4. Sum of the number fraction of carbon, nitrogen, and oxygen for the LMC (top panel) and SMC (bottom panel) stars. The horizontal dashed lines mark the C+N+O value in the LMC and SMC according to Vink et al. (2023). Stars for which the abundance determination of one of the three elements could not be performed are excluded from the figure.

jects, while the Bonn tracks favour a MS status. In the SMC, most stars are MS objects, with the exception of a couple of objects that may be post-MS objects depending on the tracks.

3.2. Nucleosynthesis

Figure 4 shows the sum of the carbon, nitrogen, and oxygen abundances for stars for which a determination of the abundances of the three elements could be performed. Nucleosynthesis through the CNO cycle predicts that the total amount of these three elements should remain constant since they act as catalysts. In the LMC and SMC stars this is what is observed, most values of the C+N+O content being close to the baseline abundance of each galaxy (see Table 3). Small (i.e. less than 2σ deviations occur in a few cases but are not unexpected because of 1) potential remaining bias in the abundance determination and 2) a spread in the baseline abundance depending on the star's locations in the galaxy. Two stars appear as outliers in the SMC. AzV469 in the SMC has a C+N+O content about three times larger than the baseline abundance. Fig. D.17 shows a good fit to most lines. In particular the nitrogen and oxygen lines are strong and imply a large C+N+O content. AzV469 may thus have experienced a peculiar chemical evolution. The other outlier (more than 2σ deviation from baseline C+N+O) is star AzV15. In that case we attribute the potential discrepancy to the abundance determination since C, N, and O lines are weak and relatively noisy (see Fig. D.2). We also refer to Sect. 3.3 for a discussion on a potential spread in chemical abundances in the SMC.

In the LMC SK-70°13 and SK-67°101 have marginally small values of the C+N+O abundance. Figs. D.27 and D.33 indicate that the C, N, and O lines are not perfectly fitted which mainly explains the relatively small deviation compared to the baseline

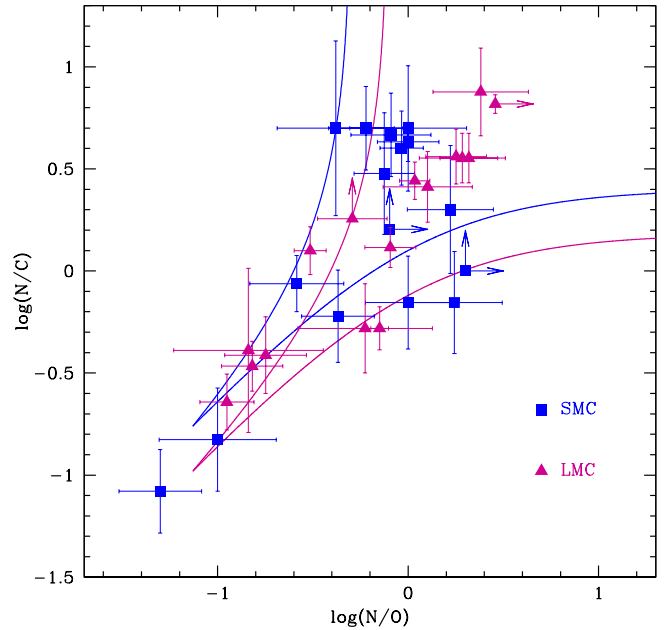


Fig. 5. Logarithm of N/C versus logarithm of N/O (all number ratios) for the XshootingU SMC (LMC) stars in blue (purple). Solid lines are the theoretical values for CNO (top) and CN (bottom) equilibrium.

abundances. SK-69°50 lies above the baseline value but the error bars are the largest of the LMC sample, making this object only a weak outlier.

For consistency we show the C+N+O sum for Galactic stars of the complementary sample in Fig. A.1. We see that 21 out of the 36 objects in this figure have values consistent with the solar case. Thirteen stars lie in between the solar and LMC reference values.

Figure 5 shows the ratios of N/H over C/H versus N/H over O/H for the XshootingU LMC and SMC sample stars. The results for the complementary samples have been presented in the publications from which the results were retrieved. The baseline values of the ratios, from which the solid lines expand, are taken from Vink et al. (2023). All stars nicely follow the trend of increasing N/C for higher N/O, in full agreement with the expectation that these elements are processed by the CNO-cycle in the interior of the stars. Within the error bars the vast majority of stars are also located in between the two theoretical curves, strengthening this conclusion. One exception in the SMC is star AzV69, which has a very low N/H ratio (blue square at the bottom left of the figure). This object has been discussed by Hillier et al. (2003). It is an OC star, a class of O stars with unprocessed abundances (Walborn 1971; Martins et al. 2016). The other SMC outlier is star AzV47 which lies slightly below the expected limit. In the LMC SK-67°261 has N/C marginally above the expected value for its N/O ratio. We stress that the exact position and shape of the curves shown in Fig. 5 depend on the initial N/C and N/O ratios. Bouret et al. (2021) show that variations in these quantities lead to shifts in the positions of these curves. Consequently stars that are outliers for a given set of initial abundances may be accommodated by a slightly different initial composition.

The nitrogen surface abundance is shown as a function of the surface He/H number ratio in Fig. 6. Stars with no significant helium enrichment can show a large range of surface ni-

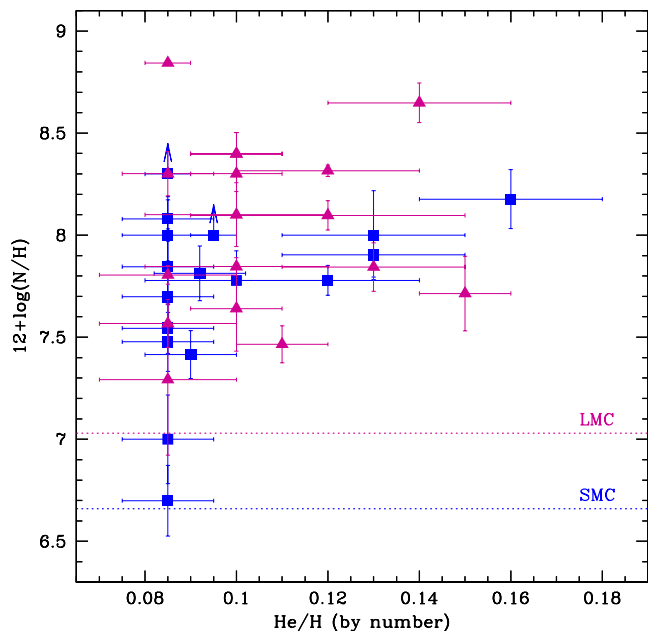


Fig. 6. Nitrogen abundance (in units of $12 + \log(N/H)$) versus He/H number ratio for XshooU SMC (LMC) stars in blue (purple). Horizontal dotted lines mark the baseline nitrogen abundances in the SMC and LMC.

trogen abundance. Contrarily, stars that show helium enrichment are also nitrogen rich. This is consistent with CNO-burning and chemical mixing (see also Rivero González et al. 2012). Nitrogen can be quickly brought to the surface even if the increase of the surface helium content has not yet happened. Indeed the fractional change relative to the baseline values is much larger for nitrogen than for helium. When a sufficient fraction of helium produced in the core has been brought to the surface so the He/H ratio is affected, the other products of CNO-burning are also seen, in particular a large nitrogen enrichment.

3.3. Metallicity effect on chemical enrichment

In this section we investigate the effect of metallicity on the surface abundances. We consider not only the stars analysed in the present study, and part of the XshooU project, but also all complementary samples described in Sect. 2.1.

Figure 7 shows the difference between the present-day and baseline N/H ratio, as a function of surface gravity. We used the baseline abundances in the LMC, SMC, and Milky Way reported in Table 3. In Figure 7 we detect a trend of surface enrichment with lower $\log g$. This is expected of mixing processes that transport the products of CNO-burning to the surface while stars evolve and reach lower surface gravity. The trend is clearly observed in the Galaxy. In the MCs significant enrichment is already seen at relatively early stages, i.e. high surface gravities. The second major conclusion is that surface nitrogen enrichment reaches a higher maximum value in the SMC than in the Galaxy, and this happens at higher surface gravity. In the Milky Way $\Delta \log(N/H)$ ranges from about 0 to ~ 1.0 . In the SMC the enrichment is about twice as large, reaching $\Delta \log(N/H) = 1.5$. In the LMC even larger values of $\Delta \log(N/H)$ are observed, up to 1.8. But the scatter is large compared to that of the SMC and MW. These results are qualitatively in line with the predictions

of all models that are presented in Fig. C.1: a stronger nitrogen enrichment is predicted at lower metallicity, and enrichment is observed at higher gravity for lower metallicity models. However the level and path to the highest enrichment is different from model to model.

Turning to the C/H ratio shown in Fig. 8, Galactic stars are significantly carbon depleted at lower surface gravity. This is expected from CNO-cycle nucleosynthesis and chemical transport to the surface, as seen in all models of Fig. C.1. However we note that depletion reaches levels lower than any model of Fig. C.1 predicts. This may be partly explained by the possible sub-solar metallicity of the Galactic stars, as indicated by the C+N+O values (Fig. A.1). But even in that case depletion is stronger than model predictions at low metallicity. Both incorrect model predictions and abundance determinations could explain this trend, but at present no clear answer can be given. In the LMC, carbon is on average depleted. The maximum depletion seems not as strong as in the Galaxy. The identification of a metallicity trend is difficult. Compared to N/H the variation of C/H is much lower (about a factor of 3) but since the error bars remain of the same order of magnitude, trends are somewhat hidden. The SMC stars show a peculiar behaviour: the dispersion is very large; some stars are carbon-depleted, but at least half of the objects are actually carbon-enhanced compared to the baseline abundance. This is opposite to all theoretical predictions which all show a slow decrease of the carbon surface abundance as a star evolves (see middle panels of Fig. C.1). This surprising behaviour in the SMC may be due to 1) systematic offsets in the carbon abundance determination or 2) improper baseline carbon abundance. If explanation 1 was correct one would expect the same trend at all metallicities, which is not observed. We visually checked that lower C/H values for the problematic objects translated into too weak C III 1176 and C III 4070 lines compared to the observed spectra. One may wonder whether the lower metallicity of the SMC produces weaker lines that are more difficult to analyse. This trend exists but as seen in Figs D.1 to D.17 the carbon lines remain relatively well detected and are useful indicators of the carbon content. For explanation 2 listed above, an offset by ~ 0.3 dex would be needed (i.e. the baseline carbon abundance in the SMC would need to be two times larger than currently estimated). In that case the most C-rich objects should also be the least nitrogen-enhanced, which is not observed: stars with high C/H show a wide range of nitrogen enrichment. Hence a systematic offset in the initial carbon content is not likely. Ramachandran et al. (2021) report a significant spread in the surface chemical composition of three binary stars in the bridge region of the SMC. One has LMC-like abundances. If such a degree of inhomogeneity was widespread in the SMC this could explain part of the issue regarding C/H in the present sample. But as we will see below this is not corroborated by surface oxygen abundances. From this we tentatively conclude that surface carbon abundances are presently not reliable to test the effect of metallicity on chemical mixing. We also see in the middle panels of Fig. C.1 that stronger depletion at lower Z is predicted by the Geneva models, and to a lesser extent by the Stromlo models. However the Bonn models do not predict any clear trend.

Finally the variation of the oxygen abundance as a function of metallicity is shown in Fig. 9. On average oxygen is depleted in most stars, in the three galaxies. This is again expected of nucleosynthesis. However given the uncertainties and the magnitude of the variations ($\Delta \log(O/H) \sim 0.2-0.3$) no conclusion can be drawn regarding any metallicity trend. The Stromlo models show such a trend but with a magnitude of the order 0.3 dex. The

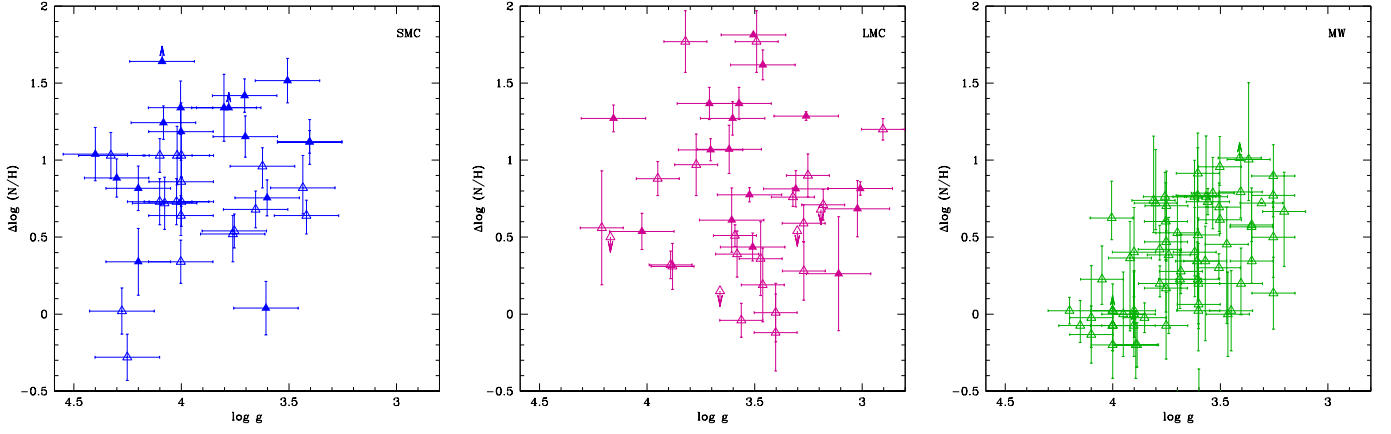


Fig. 7. logarithm of N/H minus the baseline value as a function of surface gravity for the SMC (left panel), the LMC (middle panel), the MW (right panel). Surface gravity has been corrected for the effect of rotation. XshootU sample stars are shown by filled symbols, complementary sample stars are shown by open symbols.

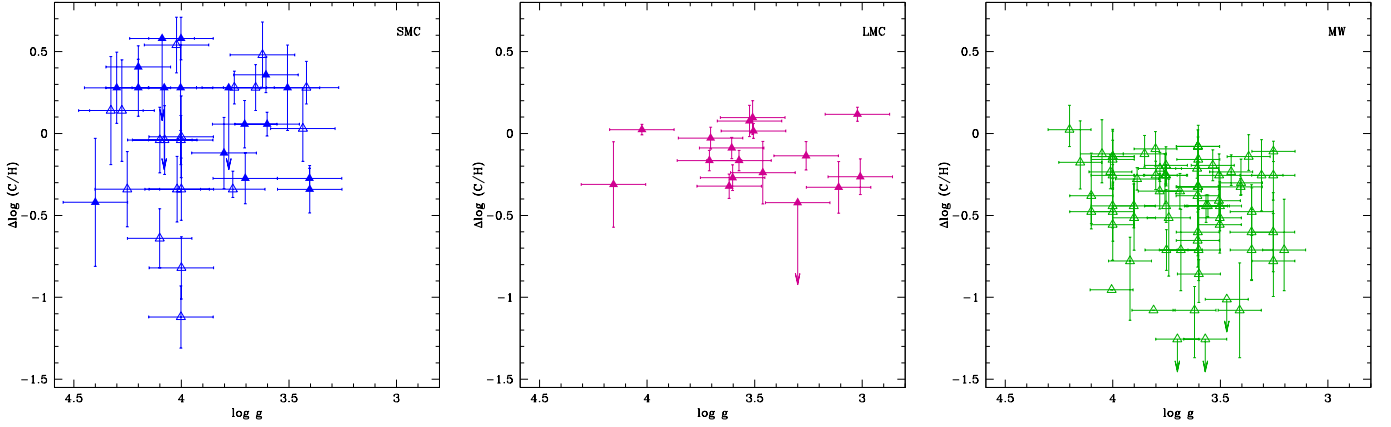


Fig. 8. Same as Fig. 7 but for the difference between C/H and the baseline carbon abundance.

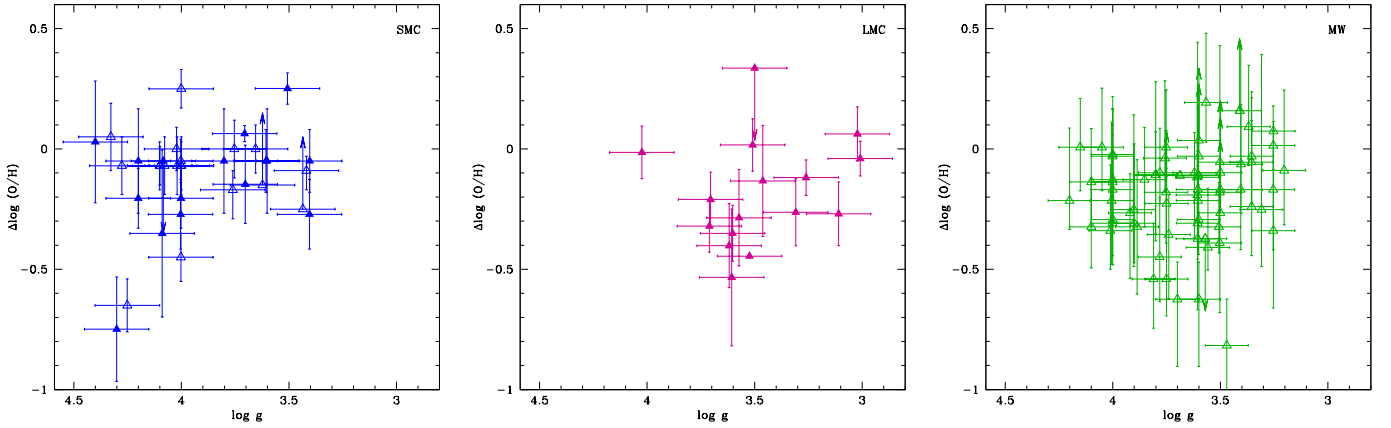


Fig. 9. Same as Fig. 7 but for the difference between O/H and the baseline oxygen abundance.

Geneva and Bonn models do not show a clear trend. Thus oxygen cannot be used to investigate the metallicity dependence of chemical mixing. We also note the same issue as C/H for Galactic stars: oxygen depletion reaches levels lower than model predictions. However the problem is less severe for oxygen since

only a handful of stars show oxygen depletion clearly stronger than model predictions.

From this analysis we conclude that surface nitrogen enrichment is the best indicator of any metallicity trend. The nitrogen enrichment is stronger in the SMC than in the Galaxy, in qualitative agreement with model predictions. For the intermediate case

of the LMC, no conclusion can be drawn at present because of the large dispersion of the measurements. The metallicity difference between the LMC and the Galaxy on one side, and the LMC and the SMC on the other side, is probably too small to lead to effects that can be distinguished with the accuracy of the measurements we can achieve with the method used for abundance determinations.

3.4. Projected rotational velocities

A classical diagram to test the predictions of evolutionary models that includes chemical and angular momentum transport caused by rotation is the N/H versus $V \sin i$ diagram. Several studies have used this diagram over the last fifteen years (Hunter et al. 2008a, 2009; Brott et al. 2011b; Rivero González et al. 2012; Bouret et al. 2013; Grin et al. 2017; Dufton et al. 2018, 2020; Markova et al. 2018; Bouret et al. 2021). As recalled in Section 1 and stressed by Maeder et al. (2014) surface chemical enrichment does not depend only on $V \sin i$, and thus comparing evolutionary models and observational properties requires population synthesis models (Brott et al. 2011b). Various sets of models treating differently transport and mixing processes have to be considered. It is also equally important to ensure that the samples to which these models are compared to are not biased and are representative of the global properties of massive stars.

In this Section we discuss the distribution of projected rotational velocities of our sample to investigate any potential bias. We show in Fig. 10 the number of stars as a function of projected rotational velocity. In the LMC and MW we use a reference sample that contains a larger number of stars and no bias in the selection except the availability of high resolution optical spectra (i.e. the samples are magnitude limited). The reference samples are further refined to include only O6-9.5 stars with luminosity classes V to II. As such, we have the same distributions of spectral types and luminosity classes as in the samples we studied in the previous sections. We have also excluded all known binaries from the reference samples.

In the Galaxy we use the sample of Holgado et al. (2022) as a reference. It is the largest sample of Galactic O stars for which projected rotational velocities were determined in a homogeneous way, using the Fourier transform method. We see in the right panel of Fig. 10 that the distribution of $V \sin i$ in this reference sample is different from that of the sample used in the present study (i.e. the XshootU + complementary sample, that for which surface abundance determinations exist). The latter contains 80% of stars with projected rotational velocities below 80 km s^{-1} , while in the reference sample only 60% have such low $V \sin i$. In other words the sample with available abundance determinations contains relatively more slow rotators than the reference sample.

The same conclusion applies even more strongly to the LMC stars for which surface nitrogen abundances have been determined. In the middle panel of Fig. 10 we use the sample of Ramírez-Agudelo et al. (2013) as a reference. It includes most O stars of 30 Dor. As for the MW we see that the distributions of $V \sin i$ in the sample for which N/H is available (purple lines) is biased towards low $V \sin i$ compared to the reference sample.

In the SMC no large reference sample exist. In the left panel of Fig. 10 we show how our XshootU plus complementary sample compares to that of Mokiem et al. (2006). The latter sample contains less stars than the former but shows a flatter distribution. However the statistical significance of the difference is low given the small number of objects considered. Penny & Gies (2009)

also determine projected rotational velocities for O stars in the SMC. But when considering only the relevant spectral types and luminosity classes, the remaining sample is even smaller than that of Mokiem et al. (2006). Consequently we cannot safely answer the question of whether our XshootU plus complementary sample is biased towards slow rotators or not in the SMC.

From these investigations we conclude that the samples of stars for which surface abundances and projected rotational velocities are both available in the literature (including the present study) appear to be biased towards slow rotators. The velocity distributions of the reference samples of Ramírez-Agudelo et al. (2013) and Holgado et al. (2022) show a high velocity component, above $\sim 150\text{--}200 \text{ km s}^{-1}$. de Mink et al. (2013) predicted that such high velocities can be caused by interactions in binary systems. Britavskiy et al. (2023) report that stars with $V \sin i > 200 \text{ km s}^{-1}$ in the sample of Holgado et al. (2022) host less spectroscopic binaries than the slow velocity sub-sample. At the same time the high velocity sub-sample contains a fraction of runaway stars about twice as large as that of the slow velocity sub-sample. They argue that this feature can be explained by the scenario of de Mink et al. (2013) in which the high runaway velocity is acquired because of the supernova explosion of the companion in binary systems, with subsequent disruption of the system (Blaauw 1961). However this is in contradiction with the theoretical work of Renzo et al. (2019) who predict that less than 2.6% of binaries should produce single runaway stars. In that case the majority of runaway stars should be the result of dynamical interaction (Poveda et al. 1967). The origin of the high velocity tail of the $V \sin i$ distribution is thus not firmly established.

It thus appears that comparing the predictions of stellar evolution models with observed trends to constrain their ability to reproduce surface abundances and projected rotational velocities is a complex task. It requires large samples including stars with high $V \sin i$, which are lacking in the current samples for which both surface abundances and $V \sin i$ have been determined. Additionally it requires populations synthesis models that include both single and binary evolutionary channels with fair accounts of their (somehow uncertain) relative contributions. Different models that account differently for the transport of angular momentum and chemical species should be tested too, since they behave rather differently. This general task is beyond the scope of the present analysis that merely focuses on investigating the effect of metallicity on surface chemical enrichment.

4. Conclusion

We have performed a spectroscopic analysis of 17 LMC and 17 SMC O-type stars using data from the ULLYSES and XshootU surveys. All stars are presumably single. We have determined the fundamental parameters (T_{eff} , $\log g$, $\log \frac{L}{L_{\odot}}$) and the He, C, N, and O surface abundances. We have complemented these results by published values for additional stars in the MCs and the Galaxy. Our goal was to investigate the effect of metallicity on chemical transport triggered by stellar rotation. We show that the surface abundances of the stars analysed in this study are consistent with the products of nucleosynthesis through the CNO cycle. A clear increase of the surface nitrogen content, sometimes accompanied by an increase in the helium content, is detected as stars evolve to lower surface gravities, that is away from the ZAMS. The evolution of surface carbon and oxygen abundances is more difficult to constrain because of the small variations rel-

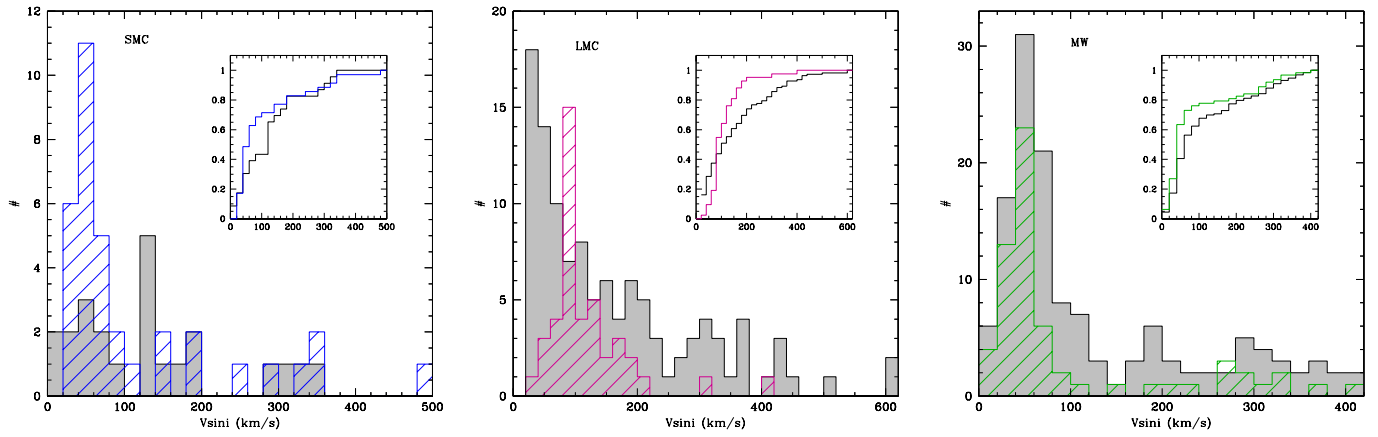


Fig. 10. Projected rotational velocity distribution in the SMC (left), LMC (middle), and the Galaxy (right). The blue, purple, and green histograms corresponds to the XshootU plus complementary samples. The grey histograms show the O6-9.5 V-II stars of Mokiem et al. (2006) in the SMC, Ramírez-Agudelo et al. (2013) in the LMC, and of Holgado et al. (2022) in the Galaxy. The inserts in each panel show the cumulative distribution functions.

ative to the error bars on abundance measurements. The maximum increase of surface N/H relative to the baseline value is larger at lower metallicity. Nitrogen enrichment is observed at higher $\log g$ in the SMC than in the Galaxy, in agreement with the predictions of evolutionary models including rotational mixing. No conclusion can be drawn for LMC objects due to the large dispersion in N/H measurements. Our sample of stars for which both surface abundances and projected rotational velocities have been determined appear to be biased towards slow rotators, at least in the LMC and the Galaxy. Future studies aiming at testing model predictions should rely on: 1) large samples with unbiased rotational velocity distributions; 2) large grids of evolutionary and population synthesis models that take into account various implementations of the physics of chemical mixing and angular momentum transport, as well as a mix of single and binary stars.

Acknowledgments

We thank an anonymous referee for a positive report. We thank Rolf Kuiper, Laurent Mahy, Andrea Mehner, Grace Telford, Matheus Bernini for text corrections and suggestions of clarifications. Based on observations obtained with the NASA/ESA Hubble Space Telescope, retrieved from the Mikulski Archive for Space Telescopes (MAST) at the Space Telescope Science Institute (STScI). STScI is operated by the Association of Universities for Research in Astronomy, Inc. under NASA contract NAS 5-26555. DP acknowledges financial support by the Deutsches Zentrum für Luft und Raumfahrt (DLR) grant FKZ 50 OR 005. AACS and VR acknowledge support by the Deutsche Forschungsgemeinschaft (DFG, German Research Foundation) in the form of an Emmy Noether Research Group – Project-ID 445674056 (SA4064/1-1, PI Sander). AACS and VR further acknowledge support from the Federal Ministry of Education and Research (BMBF) and the Baden-Württemberg Ministry of Science as part of the Excellence Strategy of the German Federal and State Governments. F.N. acknowledges grants PID2019-105552RB-C41 and PID2022-137779OB-C41 funded by the Spanish MCIN/AEI/ 10.13039/501100011033.

References

Abbott, R., Abbott, T. D., Abraham, S., et al. 2021, *ApJ*, 915, L5

- Asplund, M., Grevesse, N., Sauval, A. J., & Scott, P. 2009, *ARA&A*, 47, 481
 Bertelli, G., Bressan, A. G., & Chiosi, C. 1984, *A&A*, 130, 279
 Blaauw, A. 1961, *Bull. Astron. Inst. Netherlands*, 15, 265
 Bouret, J. C., Lanz, T., Martins, F., et al. 2013, *A&A*, 555, A1
 Bouret, J. C., Martins, F., Hillier, D. J., et al. 2021, *A&A*, 647, A134
 Britavskiy, N., Simón-Díaz, S., Holgado, G., et al. 2023, *A&A*, 672, A22
 Brott, I., de Mink, S. E., Cantiello, M., et al. 2011a, *A&A*, 530, A115
 Brott, I., Evans, C. J., Hunter, I., et al. 2011b, *A&A*, 530, A116
 Cazorla, C., Morel, T., Nazé, Y., et al. 2017, *A&A*, 603, A56
 Chiosi, C. & Maeder, A. 1986, *ARA&A*, 24, 329
 de Mink, S. E., Langer, N., Izzard, R. G., Sana, H., & de Koter, A. 2013, *ApJ*, 764, 166
 Dufton, P. L., Evans, C. J., Lennon, D. J., & Hunter, I. 2020, *A&A*, 634, A6
 Dufton, P. L., Thompson, A., Crowther, P. A., et al. 2018, *A&A*, 615, A101
 Eggenberger, P., Ekström, S., Georgy, C., et al. 2021, *A&A*, 652, A137
 Ekström, S., Georgy, C., Eggenberger, P., et al. 2012, *A&A*, 537, A146
 Ekström, S., Meynet, G., Maeder, A., & Barblan, F. 2008, *A&A*, 478, 467
 El Eid, M. F., Fricke, K. J., & Ober, W. W. 1983, *A&A*, 119, 54
 Eldridge, J. J. & Stanway, E. R. 2022, *ARA&A*, 60, 455
 Evans, C. J., Crowther, P. A., Fullerton, A. W., & Hillier, D. J. 2004, *ApJ*, 610, 1021
 Georgy, C., Ekström, S., Eggenberger, P., et al. 2013, *A&A*, 558, A103
 Grasha, K., Roy, A., Sutherland, R. S., & Kewley, L. J. 2021, *ApJ*, 908, 241
 Gray, D. F. 1976, *The observation and analysis of stellar photospheres*
 Grin, N. J., Ramírez-Agudelo, O. H., de Koter, A., et al. 2017, *A&A*, 600, A82
 Heap, S. R., Lanz, T., & Hubeny, I. 2006, *ApJ*, 638, 409
 Hillier, D. J., Lanz, T., Heap, S. R., et al. 2003, *ApJ*, 588, 1039
 Hillier, D. J. & Miller, D. L. 1998, *ApJ*, 496, 407
 Holgado, G., Simón-Díaz, S., Herrero, A., & Barbá, R. H. 2022, *A&A*, 665, A150
 Hunter, I., Brott, I., Langer, N., et al. 2009, *A&A*, 496, 841
 Hunter, I., Brott, I., Lennon, D. J., et al. 2008a, *ApJ*, 676, L29
 Hunter, I., Lennon, D. J., Dufton, P. L., et al. 2008b, *A&A*, 479, 541
 Langer, N. 2012, *ARA&A*, 50, 107
 Limongi, M. & Chieffi, A. 2018, *ApJS*, 237, 13
 Maeder, A. & Meynet, G. 2001, *A&A*, 373, 555
 Maeder, A., Przybilla, N., Nieva, M.-F., et al. 2014, *A&A*, 565, A39
 Markova, N., Puls, J., & Langer, N. 2018, *A&A*, 613, A12
 Martins, F. 2018, *A&A*, 616, A135
 Martins, F., Escolano, C., Wade, G. A., et al. 2012, *A&A*, 538, A29
 Martins, F., Foschino, S., Bouret, J. C., Barbá, R., & Howarth, I. 2016, *A&A*, 588, A64
 Martins, F., Hervé, A., Bouret, J. C., et al. 2015, *A&A*, 575, A34
 Martins, F. & Hillier, D. J. 2012, *A&A*, 545, A95
 Martins, F. & Palacios, A. 2017, *A&A*, 598, A56
 Martins, F. & Palacios, A. 2021, *A&A*, 645, A67
 Martins, F. & Plez, B. 2006, *A&A*, 457, 637
 Martins, F., Schaerer, D., & Hillier, D. J. 2005, *A&A*, 436, 1049
 Martins, F., Simón-Díaz, S., Barbá, R. H., Gamen, R. C., & Ekström, S. 2017, *A&A*, 599, A30
 Massey, P. 2013, *New A Rev.*, 57, 14
 Massey, P., Puls, J., Pauldrach, A. W. A., et al. 2005, *ApJ*, 627, 477
 Massey, P., Zangari, A. M., Morrell, N. I., et al. 2009, *ApJ*, 692, 618

- Meynet, G. & Maeder, A. 2000, A&A, 361, 101
- Meynet, G. & Maeder, A. 2002, A&A, 390, 561
- Mokiem, M. R., de Koter, A., Evans, C. J., et al. 2007, A&A, 465, 1003
- Mokiem, M. R., de Koter, A., Evans, C. J., et al. 2006, A&A, 456, 1131
- Nieva, M. F. & Przybilla, N. 2012, A&A, 539, A143
- Pauldrach, A. W. A., Kudritzki, R. P., Puls, J., Butler, K., & Hunsinger, J. 1994, A&A, 283, 525
- Penny, L. R. & Gies, D. R. 2009, ApJ, 700, 844
- Poveda, A., Ruiz, J., & Allen, C. 1967, Boletín de los Observatorios Tonantzintla y Tacubaya, 4, 86
- Puls, J., Urbaneja, M. A., Venero, R., et al. 2005, A&A, 435, 669
- Puls, J., Vink, J. S., & Najarro, F. 2008, A&A Rev., 16, 209
- Ramachandran, V., Oskinova, L. M., & Hamann, W. R. 2021, A&A, 646, A16
- Ramírez-Agudelo, O. H., Simón-Díaz, S., Sana, H., et al. 2013, A&A, 560, A29
- Renzo, M., Zapartas, E., de Mink, S. E., et al. 2019, A&A, 624, A66
- Rivero González, J. G., Puls, J., & Najarro, F. 2011, A&A, 536, A58
- Rivero González, J. G., Puls, J., Najarro, F., & Brott, I. 2012, A&A, 537, A79
- Sana, H., Trammer, F., Abdul-Masih, M., et al. 2024, arXiv e-prints, arXiv:2402.16987
- Sander, A., Shenar, T., Hainich, R., et al. 2015, A&A, 577, A13
- Schaller, G., Schaerer, D., Meynet, G., & Maeder, A. 1992, A&AS, 96, 269
- Serebriakova, N., Tkachenko, A., Gebruers, S., et al. 2023, A&A, 676, A85
- Simón-Díaz, S. 2020, in Reviews in Frontiers of Modern Astrophysics; From Space Debris to Cosmology, 155–187
- Simón-Díaz, S. & Herrero, A. 2007, A&A, 468, 1063
- Simón-Díaz, S. & Herrero, A. 2014, A&A, 562, A135
- Simón-Díaz, S., Herrero, A., Sábín-Sanjulián, C., et al. 2014, A&A, 570, L6
- Sota, A., Maíz Apellániz, J., Walborn, N. R., et al. 2011, ApJS, 193, 24
- Szécsi, D., Agrawal, P., Wünsch, R., & Langer, N. 2022, A&A, 658, A125
- Vink, J. S. 2022, ARA&A, 60, 203
- Vink, J. S., de Koter, A., & Lamers, H. J. G. L. M. 2001, A&A, 369, 574
- Vink, J. S., Mehner, A., Crowther, P. A., et al. 2023, A&A, 675, A154
- Walborn, N. R. 1971, ApJ, 164, L67

Table 1. Stellar parameters for LMC stars

Star	ST	T_{eff} [kK]	$\log g$	$\log g_c$	$\log \frac{L}{L_{\odot}}$ [km s ⁻¹]	$V \sin i$ [km s ⁻¹]	v_{mac} [km s ⁻¹]	v_{turb}	He/H [10 ⁻⁵]	C/H [10 ⁻⁵]	N/H [10 ⁻⁵]	O/H
Sk-66° 18	O6 V	38.0	3.70	3.71	5.42	100	0	15	0.10±0.010	7.0±1.0	25.0±6.0	12.0±3.0
Sk-71° 19	O6 III	39.0	4.10	4.16	5.12	311	0	15	0.10±0.010	5.0±3.0	20.0±4.0	–
N11 018	O6 II(f+)	37.0	3.60	3.60	5.67	50	70	15	0.085±0.010	5.5±1.0	20.0±5.0	11.2±3.0
Sk-71° 50	O6.5 III	35.0	3.50	3.57	5.21	210	0	20	0.10±0.010	7.0±1.0	25.0±6.0	13.0±6.0
Sk-66° 152	O7 Ib(f)	32.9	3.20	3.26	5.60	180	45	15	0.12±0.02	7.48±1.49	20.7±1.34	19.1±3.25
N11 032	O7 II(f)	34.9	3.50	3.51	5.34	60	70	10	0.085±0.035	10.6±1.1	69.7±0.7	<24.3
Sk-69° 50	O7(n)(f)p	35.0	3.40	3.46	5.45	197	80	15	0.14±0.02	5.9±2.6	44.5±10.0	18.5±9.84
Sk-68° 16	O7 III	36.9	3.70	3.71	5.74	83	40	10	0.12±0.03	9.59±1.48	12.5±2.1	15.5±4.0
N11 049	O7.5 V	37.0	4.00	4.02	5.11	187	21	10	0.085±0.015	10.8±0.8	3.69±1.0	24.3±0.6
Sk-67° 101	O8 II((f))	34.0	3.60	3.61	5.56	85	78	10	0.10±0.010	8.35±1.25	4.37±2.1	7.35±4.81
BI 173	O8 III	33.9	3.50	3.52	5.53	146	92	15	0.085±0.015	12.2±2.67	6.38±0.67	9.00±0.17
Sk-67° 261	O8.5 III	27.0	3.00	3.01	5.48	60	50	10	0.10±0.02	5.57±1.4	7.01±0.7	22.9±3.8
Sk-67° 191	O8 V	34.1	3.60	3.62	5.27	123	74	15	0.10±0.02	4.88±0.84	12.6±4.55	9.95±4.00
Sk-66° 171	O9 Ia	30.0	3.00	3.02	5.71	98	20	15	0.15±0.010	13.4±1.32	5.18±2.18	29.0±7.5
Sk-71° 8	O9 II	28.0	3.30	3.31	5.20	69	31	15	0.13±0.020	<3.87	6.98±1.90	13.7±4.40
BI 128	O9 V	32.3	3.50	3.51	5.08	72	0	15	0.11±0.010	12.8±3.02	2.92±0.61	26.1±6.54
Sk-70° 13	O9 V	29.0	3.20	3.21	5.64	75	70	10	0.085±0.015	4.80±1.74	1.96±1.67	13.5±4.12

Notes. Columns are star’s ID, spectral type from Vink et al. (2023), effective temperature, surface gravity, surface gravity corrected for centrifugal acceleration, luminosity, projected rotational velocity, macroturbulent velocity, microturbulent velocity, abundance of He, C, N, and O by number. Typical uncertainties on $V \sin i$ and v_{mac} are of the order 10-20 km s⁻¹. For v_{turb} 5 km s⁻¹ is a reasonable error as explained in Sect. 2.3. Uncertainties on T_{eff} and $\log g$ are correlated and typical values are shown in Fig. 1. An error of about 0.15 dex on luminosity is a typical value.

Table 2. Stellar parameters for SMC stars

Star	ST	T_{eff} [kK]	$\log g$	$\log g_c$	$\log \frac{L}{L_{\odot}}$	$V \sin i$ [km s ⁻¹]	v_{mac} [km s ⁻¹]	v_{turb} [km s ⁻¹]	He/H	C/H [10 ⁻⁵]	N/H [10 ⁻⁵]	O/H [10 ⁻⁵]
AzV6	O9 III	36.0	4.20	4.20	5.84	60	50	10	0.085±0.010	6.7±2.0	1.0±0.5	10.0±5.0
AzV15	O6.5 II(f)	38.0	3.70	3.71	5.72	90	90	10	0.085±0.010	3.0±1.0	12.0±3.0	13.0±1.0
AzV47	O8 III((f))	38.0	4.30	4.30	5.60	65	50	10	0.085±0.010	5.0±2.5	3.5±1.0	2.0±1.0
AzV69	OC7.5 III((f))	36.0	3.60	3.61	5.60	85	70	15	0.085±0.010	6.0±1.5	0.5±0.2	10.0±3.0
AzV80	O7 III	38.0	3.70	3.78	5.71	350	0	10	0.085±0.010	<5.0	>20.0	–
AzV95	O7 III((f))	37.0	3.70	3.71	5.43	55	50	15	0.092±0.010	1.4±0.5	6.5±2.0	8.0±3.0
AzV148	O8.5 V	31.0	3.60	3.60	5.16	35	0	10	0.090±0.010	3.0±0.5	2.6±0.7	10.0±5.0
AzV186	O8.5 III((f))	36.0	3.80	3.80	5.63	55	10	10	0.130±0.02	2.0±1.0	10.0±5.0	10.0±5.0
AzV207	O7 III((f))	38.0	4.00	4.00	5.21	75	70	15	0.085±0.010	5.0±3.0	10.0±4.0	6.0±2.0
AzV243	O6 V	41.0	4.00	4.00	5.50	60	40	10	0.085±0.010	10.0±3.0	7.0±3.0	7.0±2.0
AzV251	O7 V	36.0	3.90	4.09	5.01	500	0	15	0.095±0.010	<10.0	>10.0	5.0±4.0
AzV267	O8 V	37.0	4.00	4.08	4.93	325	0	15	0.13±0.02	<5.0	8.0±2.0	<10.0
AzV307	O9 III	29.0	3.40	3.40	5.12	45	30	15	0.10±0.02	1.2±0.4	6.0±2.0	10.0±3.0
AzV327	O9.5 II-Ibw	31.0	3.40	3.40	5.55	60	40	10	0.12±0.02	1.4±0.2	6.0±1.0	6.0±2.0
AzV440	O7.5 III	37.0	4.20	4.20	5.03	35	30	5	0.085±0.010	5.0±2.0	3.0±1.0	7.0±2.0
AzV446	O6.5 V	42.0	4.40	4.40	5.22	35	0	5	0.085±0.010	1.0±0.9	5.0±2.0	12.0±7.0
AzV469	O8.5 II((f))	33.0	3.50	3.50	5.58	80	30	20	0.16±0.02	5.0±3.0	15.0±5.0	20.0±3.0

Notes. Columns are star's ID, spectral type from Vink et al. (2023), effective temperature, surface gravity, surface gravity corrected for centrifugal acceleration, luminosity, projected rotational velocity, macroturbulent velocity, microturbulent velocity, abundance of He, C, N, and O by number. Uncertainties are described in Table. 1.

Table 3. Baseline abundances adopted in this study.

Galaxy	C	N	O
MW	8.43	7.83	8.69
LMC	8.01	7.03	8.40
SMC	7.42	6.66	8.05

Notes. Units are $12+\log(X/H)$. References are Asplund et al. (2009) for the MW and Vink et al. (2023) for the MCs. For the MCs the values are an average from various literature studies.

Appendix A: Complementary samples

Table A.1 lists the members of the complementary samples described in Sect. 2.1 and the references they were taken from. Figure A.1 shows the sum of the carbon, nitrogen, and oxygen number fractions for the Galactic stars of the complementary samples.

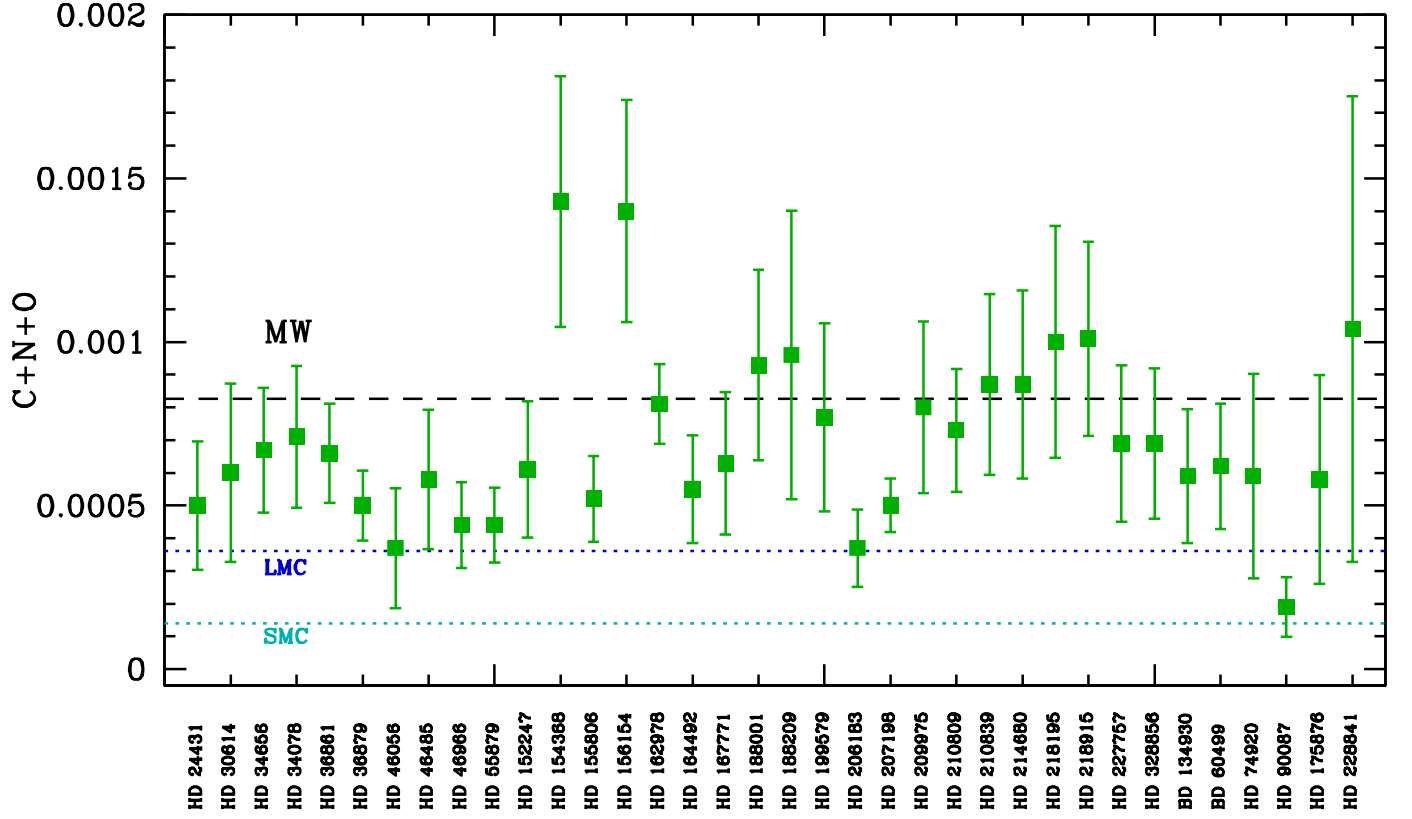


Fig. A.1. Same as Fig. 4 but for the complementary Galactic sample stars. Stars with an upper or lower limit on at least one of the abundance measurements are excluded from this figure. The horizontal broken lines show the Galactic, LMC, and SMC values.

Table A.1. Complementary samples.

Star	ST	reference	Star	ST	reference
SMC			LMC		
AzV77	O7 III	1	VFTS046	O9.7 II((n))	3
AzV439	O9.5 III	1	VFTS076	O9.2 III	3
AzV170	O9.7 III	1	VFTS087	O9.7 Ib-II	3
AzV43	B0.5 III	1	VFTS103	O8.5 III((f))	3
AzV388	O4 V	2	VFTS151	O6.5 II(f)p	3
MPG324	O4 V	2	VFTS153	O9 III((n))	3
MPG368	O6 V	2	VFTS160	O9.5 III((n))	3
MPG113	OC6 Vz	2	VFTS172	O9 III((f))	3
MPG356	O6.5 V	2	VFTS178	O9.7 Iab	3
AzV429	O7 V	2	VFTS185	O7.5 III((f))	3
MPG523	O7 Vz	2	VFTS259	O6 Iaf	3
NGC346 046	O7 Vn	2	VFTS306	O8.5 II((f))	3
NGC346 031	O8 Vz	2	VFTS466	O9 III	3
AzV461	O8 V	2	VFTS502	O9.7 II	3
MPG299	O8 Vn	2	VFTS503	O9 III	3
MPG487	O8 V	2	VFTS513	O6-7 II(f)	3
AzV468	O8.5 V	2	VFTS546	O8-9 III:((n))	3
MPG682	O9 V	2	VFTS664	O7 II(f)	3
MPG012	B0 IV	2	VFTS669	O8 Ib(f)	3
			VFTS764	O9.7 Ia	3
			VFTS777	O9.2 II	3
			VFTS782	O8.5 III	3
			VFTS807	O9.5 III	3
			VFTS819	O8 III((f))	3
MW			MW		
BD+60 261	O7.5 III(n)(f)	4	HD167263	O9.5 III	5
HD24912	O7.5 III(n)(f)	4	HD167771	O7.5 III(f)	5
HD34656	O7.5 II(f)	4	HD188001	O7.5 Iabf	5
HD35633	O7.5 II(n)(f)	4	HD188209	O9.5 Iab	5
HD36861	O8 III(f)	4	HD189957	O9.7 III	5
HD94963	O7 II(f)	4	HD192639	O7.5 Iabf	5
HD97434	O7.5 III(n)(f)	4	HD193443	O9 III	5
HD151515	O7 II(f)	4	HD199579	O6.5 V((f))z	5
HD162978	O8 II(f)	4	HD201345	ON9.2 IV	5
HD163800	O7.5 III(f)	4	HD203064	O7.5 IIIIn((f))	5
HD167659	O7 II-III(f)	4	HD206183	O9.5 IV-V	5
HD171589	O7 II(f)	4	HD207198	O8.5 II	5
HD175754	O8 II(n)((f))p	4	HD209975	O9 Ib	5
HD186980	O7.5 III(f)	4	HD210809	O9 Iab	5
HD203064	O7.5 IIIIn((f))	4	HD210839	O6 I(n)fp	5
HD14633	ON8.5 V	5	HD214680	O9 V	5
HD24431	O9 III	5	HD218195	O8.5 IIIInstr	5
HD30614	O9 Ia	5	HD218915	O9.2 Iab	5
HD34656	O7.5 II(f)	5	HD227757	O9.5 V	5
HD34078	O9.5 V	5	HD258691	O9 V	5
HD35619	O7.5 V((f))	5	HD328856	O9.7 II	5
HD36861	O8 III((f))	5	BD-13 4930	O9.5 V	5
HD36879	O7V(n)((f))z	5	BD+60 499	O9.5 V	5
HD38666	O9.5 V	5	HD63005	O6.5 IV(f)	6
HD42088	O6 V	5	HD92504	O8.5 V(n)	6
HD46056	O8 Vn	5	CPD-58 2620	O7 Vz	6
HD46485	O7 V((f))nz	5	HD93222	O7 V((f))z	6
HD46966	O8.5 IV	5	CD-44 4865	O9.7 III	6
HD55879	O9.7 III	5	CD-43 4690	O6.5 III	6
HD66788	O8 V	5	HD97848	O8 V	6
HD152247	O9.2 III	5	HD302505	O8.5 III	6
HD152249	OC9 Iab	5	HD15642	O9.5 III-IIIIn	7
HD153426	O8.5 III	5	HD74920	O7.5 IVn((f))	7
HD154368	O9 Iab	5	HD90087	O9.2 III(n)	7
HD154643	O9.7 III	5	HD117490	ON9.5 IIIInn	7
HD155806	O7.5 V((f))z	5	HD150574	ON9 III(n)	7
HD156154	O7.5 Ib(f)	5	HD175876	O6.5 III(n)(f)	7
HD162978	O8 II(f)	5	HD191423	ON9 II-IIIInn	7
HD164492	O7.5 Vz	5	HD228841	O6.5 Vn((f))	7

Notes. Columns are star's ID, spectral type and reference. References are 1- Bouret et al. (2021), 2- Bouret et al. (2021), 3- Grin et al. (2017), 4- Martins et al. (2017), 5- Martins et al. (2015), 6- Markova et al. (2018), 7- Cazorla et al. (2017).

Appendix B: Stellar parameters from present and literature studies

Table B.1 gathers the results of spectroscopic analysis for stars that have been previously studied in the literature. The present results are also included for clarity.

Table B.1. Parameters from literature studies

Star	T_{eff} [kK]	$\log g$	$\log \frac{L}{L_{\odot}}$	$V \sin i$ [km s ⁻¹]	He/H	$\epsilon(\text{C})$	$\epsilon(\text{N})$	$\epsilon(\text{O})$	reference
AzV15	38.0	3.7	5.72	90	0.085±0.005	7.48±0.15	8.08±0.11	8.11±0.33	this study
	39.0	3.61	5.83	120	0.10	7.00±0.11	7.78±0.13	7.90±0.13	1
	38.5	3.6	5.82	180	0.10	–	–	–	2
	37.0	3.5	–	100	–	7.42	7.92	–	3
	39.4	3.69	5.82	135	0.10±0.03	–	–	–	4
AzV47	38.0	4.3	5.60	65	0.085±0.005	7.70±0.22	7.54±0.12	8.30±0.22	this study
	35.0	3.75	5.44	60	0.10	7.69±0.09	7.08±0.15	7.98±0.08	1
	35.0	3.75	–	60	–	7.42	7.22	–	3
AzV69	36.0	3.6	5.60	85	0.085±0.005	7.78±0.11	6.70±0.17	8.00±0.13	this study
	33.9	3.5	5.61	70	0.10	7.56±0.15	6.34±0.17	8.23±0.12	1
	35.0	3.4	–	70	–	7.52	6.70	–	3
	33.9	3.5	5.61	–	0.10	7.56	6.34	8.23	5
AzV95	37.0	3.7	5.43	55	0.092±0.008	7.15±0.16	7.81±0.13	7.30±0.17	this study
	38.0	3.7	5.46	55	0.10	7.30±0.10	7.60±0.11	7.96±0.10	1
	35.0	3.4	–	80	–	7.42	7.62	–	3
	38.3	3.66	5.56	68	0.13±0.04	–	–	–	4
AzV148	31.0	3.6	5.16	35	0.090±0.005	7.48±0.07	7.41±0.12	8.00±0.22	this study
	32.3	4.0 ^a	4.84	60	0.09	7.69±0.12	7.26±0.23	7.99±0.11	1
AzV186	36.0	3.8	5.63	55	0.13±0.02	7.30±0.22	8.00±0.22	8.00±0.22	this study
	34.5	3.4	5.40	78	–	–	–	–	6
AzV207	38.0	4.0	5.21	75	0.085±0.005	7.70±0.26	8.00±0.17	7.78±0.14	this study
	37.0	3.72	5.32	120	0.1	–	–	–	7
AzV243	41.0	4.0	5.50	60	0.085±0.005	8.00±0.14	7.85±0.19	7.85±0.12	this study
	39.6	3.9	5.59	60	0.09	7.20±0.15	7.50±0.24	7.90±0.10	1
	42.6	3.94	5.68	59	0.12±0.02	–	–	–	4
AzV267	37.0	4.0	4.93	325	0.13±0.02	<7.70	7.90±0.11	<7.30	this study
	35.7	4.04	4.90	220	0.10	7.30±0.14	7.48±0.23	7.98±0.13	1
AzV307	29.0	3.4	5.12	45	0.10±0.02	7.08±0.14	7.78±0.14	8.00±0.14	this study
	30.0	3.5	5.15	60	0.12	7.38±0.17	7.56±0.18	7.95±0.10	1
AzV327	31.0	3.4	5.55	60	0.12±0.02	7.15±0.06	7.78±0.07	7.78±0.14	this study
	30.0	3.12	5.54	95	0.15	7.30±0.11	8.08±0.25	7.66±0.13	1
	30.0	3.25	–	60	–	7.12	7.22	–	3
AzV440	37.0	4.2	5.03	35	0.085±0.005	7.70±0.17	7.48±0.14	8.00±0.30	this study
	37.0	4.01	5.28	100	0.2	–	–	–	7
AzV446	42.0	4.4	5.22	35	0.085±0.005	7.00±0.39	7.70±0.17	8.08±0.25	this study
	39.7	4.0 ^a	5.25	30	0.09	7.20±0.13	7.48±0.20	7.98±0.11	1
	41.0	4.15	5.29	95	0.15	–	–	–	7
AzV469	33.0	3.5	5.58	80	0.16±0.02	7.69±0.26	8.17±0.14	8.30±0.29	this study
	34.0	3.41	5.70	81	0.17±0.03	–	–	–	4
	32.0	3.13	5.64	120	0.20	–	–	–	7
	33.0	3.4	5.5	80	0.20	7.1	8.2	–	8
N11 032	34.9	3.5	5.34	60	0.085±0.005	8.03±0.05	8.84±0.01	<8.39	this study
	36.0	3.5	5.15	60	0.09	–	7.87±0.15	–	9
	35.2	3.45	5.43	65	0.09±0.02	–	–	–	10
BI 173	33.9	3.5	5.53	146	0.085±0.015	8.09±0.10	7.80±0.05	7.95±0.01	this study
	34.5	3.4	5.60	200	0.10	–	–	–	2
Sk-66° 18	38.0	3.7	5.42	100	0.10±0.01	7.85±0.06	8.40±0.10	8.08±0.11	this study
	39.7	3.76	5.52	70	0.14	–	8.48±0.15	–	9
	40.2	3.76	5.55	82	0.14	–	–	–	10
Sk-70° 13	29.0	3.2	5.64	75	0.085±0.015	7.68±0.16	7.29±0.37	8.13±0.13	
	26.5	2.96	–	60	–	–	–	–	11

Notes. *a*: adopted value. References are 1- Bouret et al. (2013, 2021), 2- Massey et al. (2009), 3- Heap et al. (2006), 4- Mokiem et al. (2006), 5- Hillier et al. (2003), 6- Hunter et al. (2008b), 7- Massey et al. (2005), 8- Evans et al. (2004), 9- Rivero González et al. (2012), 10- Mokiem et al. (2007), 11- Serebriakova et al. (2023).

Appendix C: Surface abundances in various models

Figs. C.1 shows the predictions of the three sets of models regarding the evolution of surface abundances with surface gravity, taken as a proxy for time.

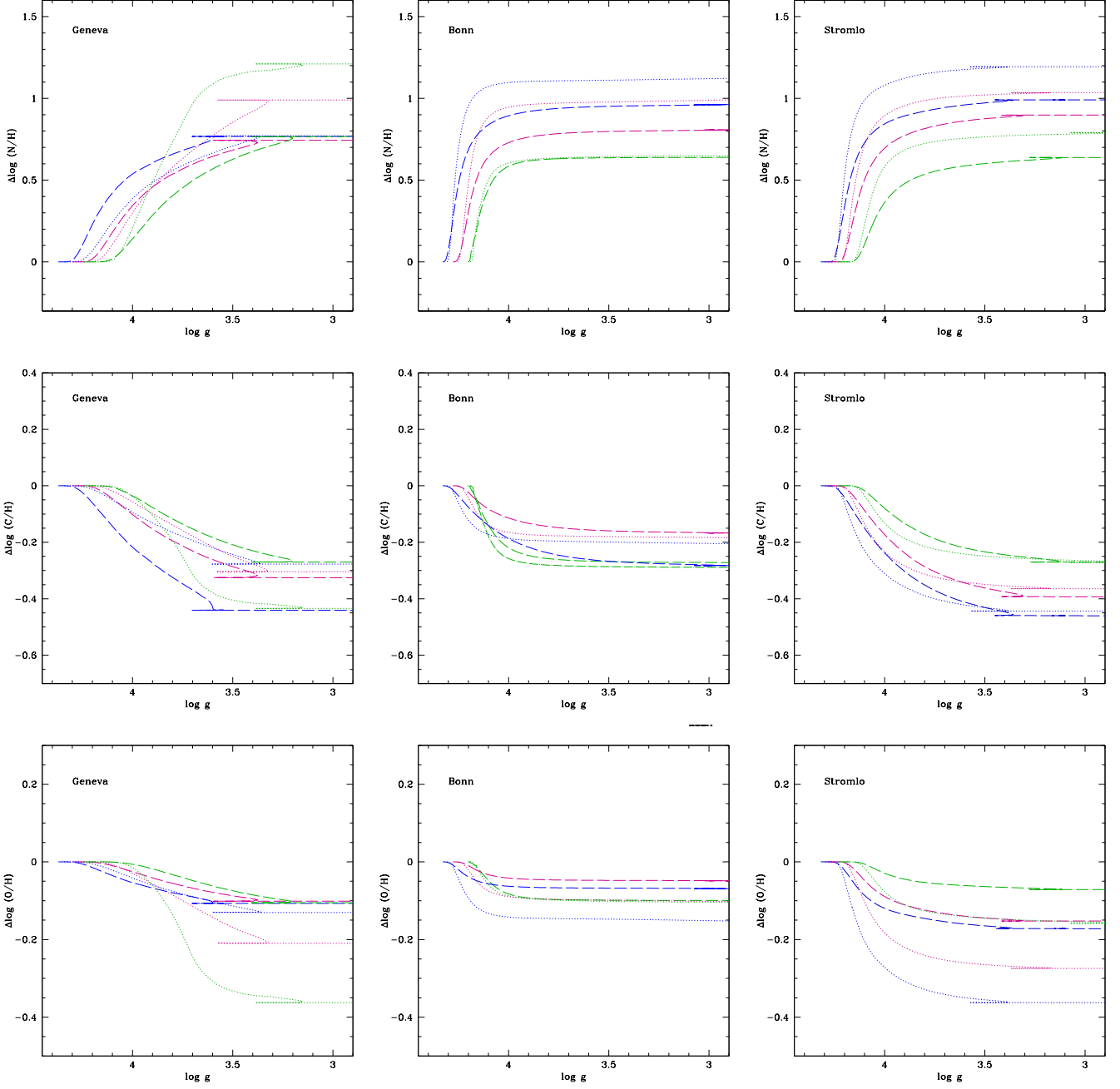


Fig. C.1. Difference between present and initial surface abundance as a function of surface gravity. Top, middle, and bottom rows show differences in nitrogen, carbon, and oxygen abundances respectively. The Geneva, Bonn, and Stromlo models are shown in the left, middle, and right column respectively. For each set of models the 25 and 40 M_{\odot} tracks are shown by the dashed and dotted lines respectively. Green, magenta, and blue lines correspond to Galactic, LMC, and SMC chemical composition.

Appendix D: Best fits

In this Section we gather the figures showing the best fit models (in red) compared to the observed UV and optical spectra of the XshooU sample stars.

We summarise the main issues as follows. For some stars (BI 173, SK-67° 101, SK-67° 191, N11 018, AzZV15, AzV95, AzV207) N IV 3478-83 is slightly under-predicted compared to other nitrogen lines. We found that increasing the effective temperature by 500 to 1000 K improves the fit at the cost of degrading the fit of the helium lines. Details of the line-blanketing such as microturbulence (not only in the spectrum computation, but also in the atmospheric calculations) affect the shape of the N IV lines.

In some cases we encountered an inconsistency in the amount of broadening inferred from the UV and optical spectra. For stars AzV148 and AzV307 fitting the UV spectra would require a stronger broadening, while for SK-70° 13 the model overestimates the broadening of the optical spectrum. We double-checked the determination of the projected rotational velocity and verified that the instrumental broadening was correctly taken into account in those cases. The reason for the discrepancy remains unclear.

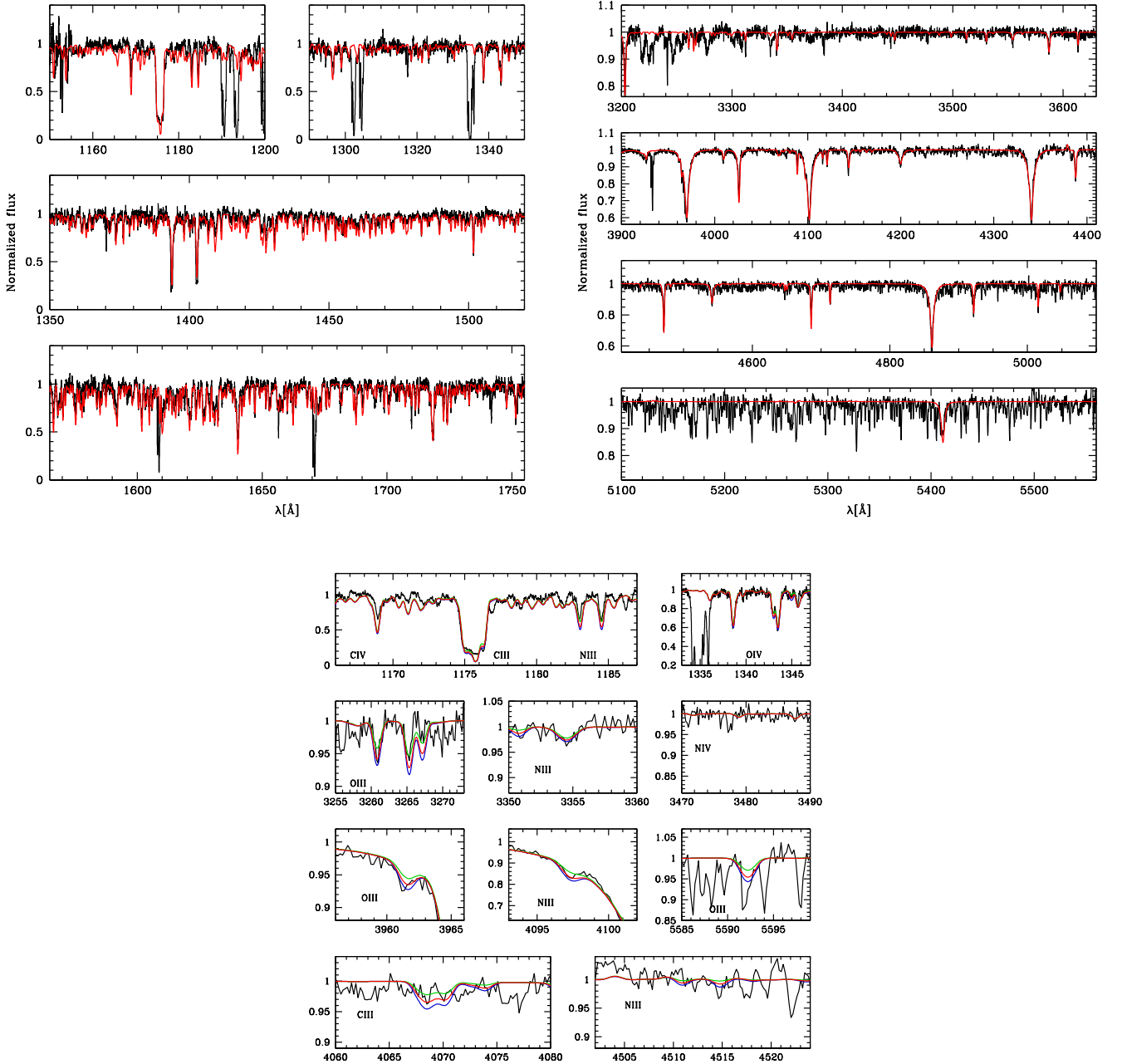


Fig. D.1. Best fit model (red) of the spectrum (black) of AzV6. The top left (top right) panel shows the UV (optical) range. The bottom panel shows a zoom on CNO lines. In that panel the blue (green) line show the effect of increasing (decreasing) the abundances by the uncertainties quoted in Table.2.

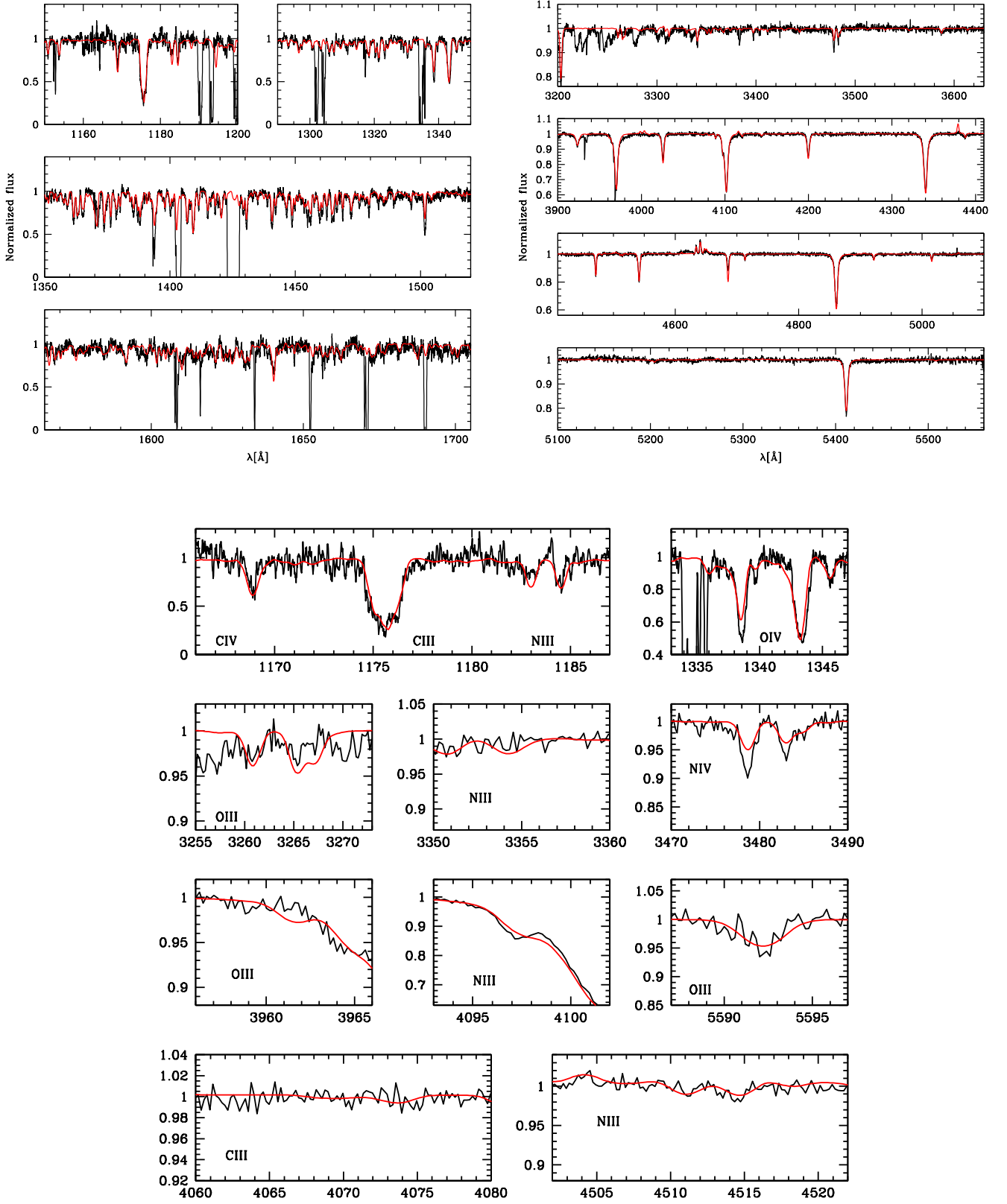


Fig. D.2. Best fit model (red) of the spectrum (black) of AzV15. The top left (top right) panel shows the UV (optical) range. The bottom panel shows a zoom on CNO lines.

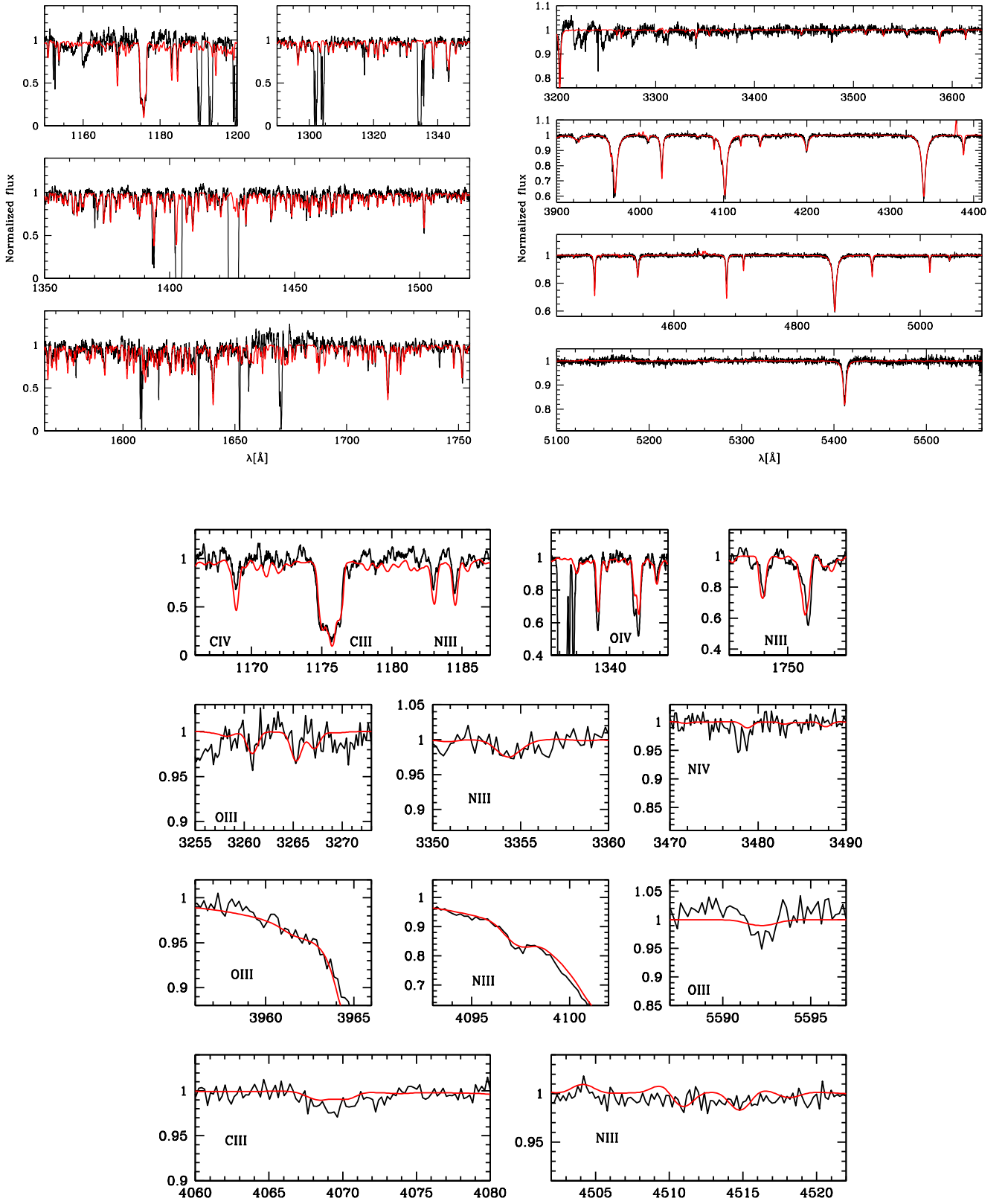


Fig. D.3. Same as Fig. D.2 but for AzV47.

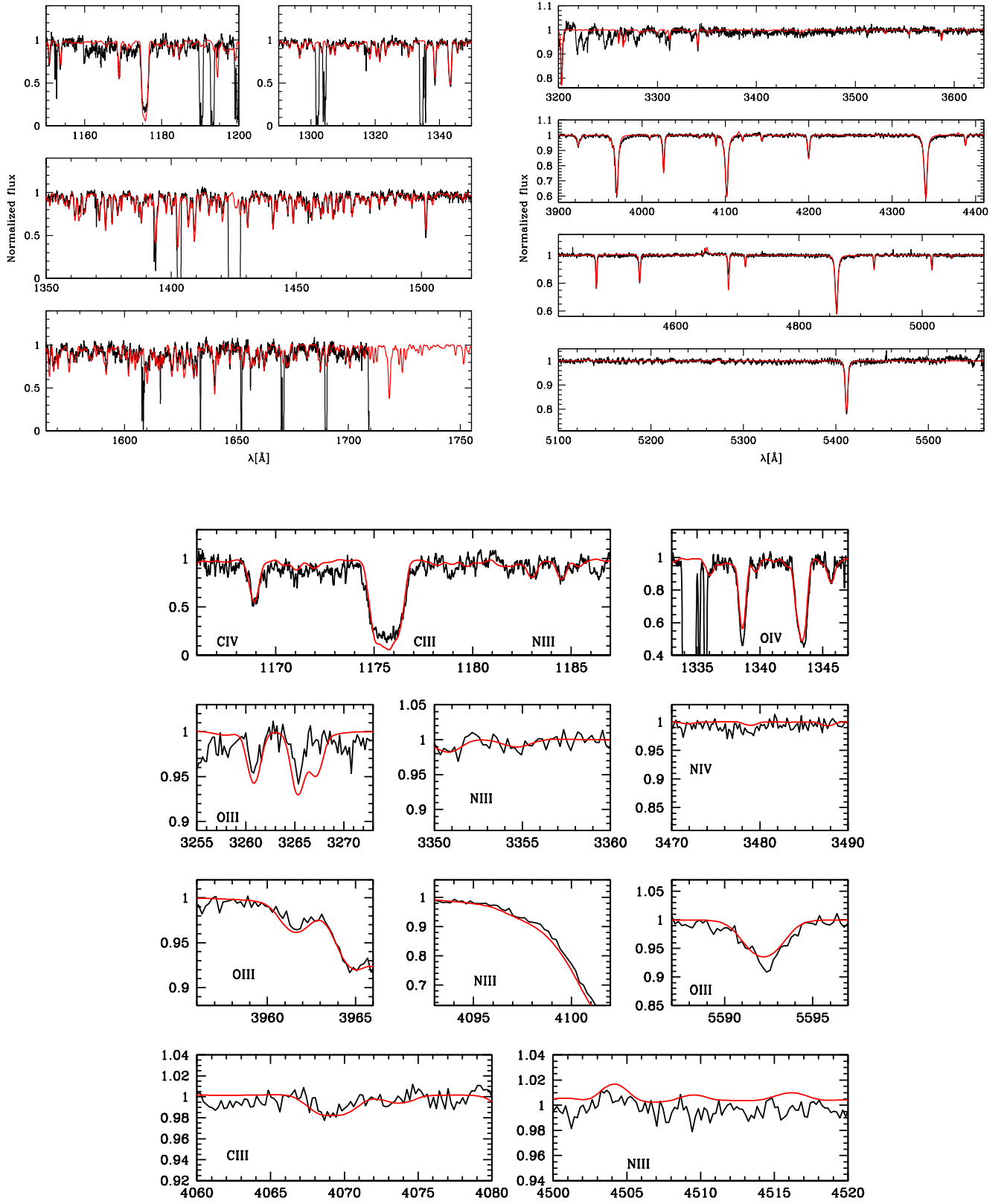


Fig. D.4. Same as Fig. D.2 but for AzV69.

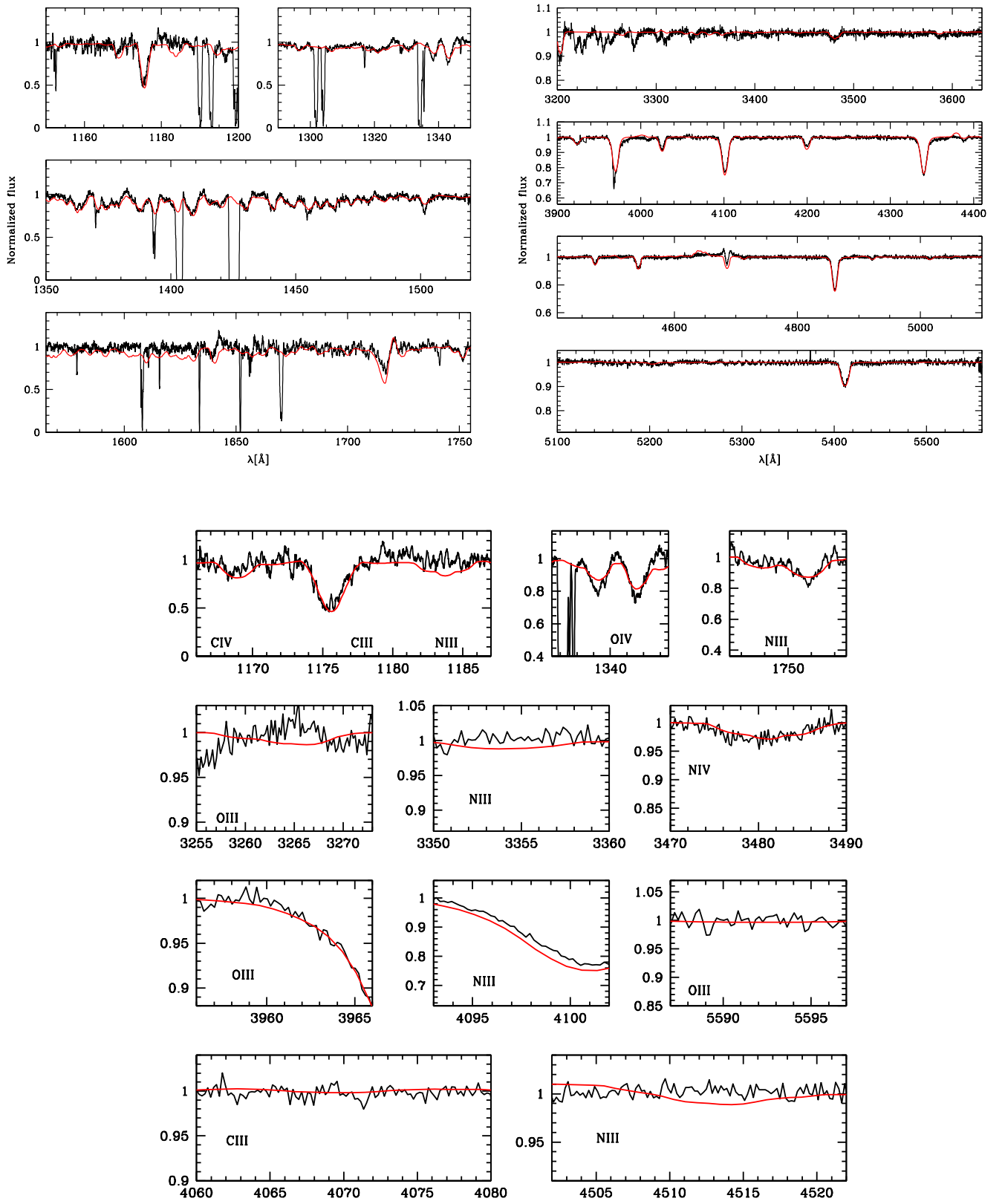


Fig. D.5. Same as Fig. D.2 but for AzV80.

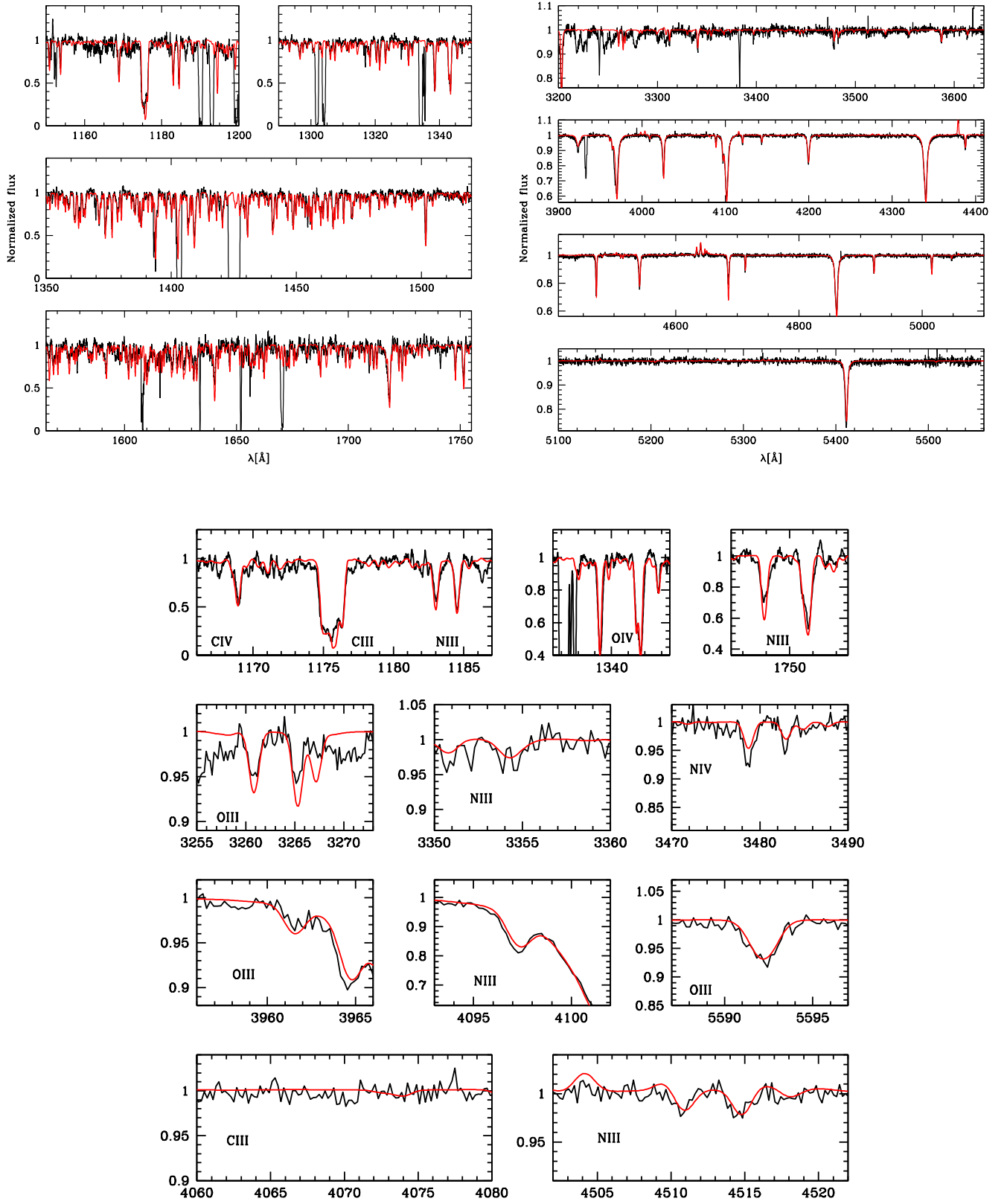


Fig. D.6. Same as Fig. D.2 but for AzV95.

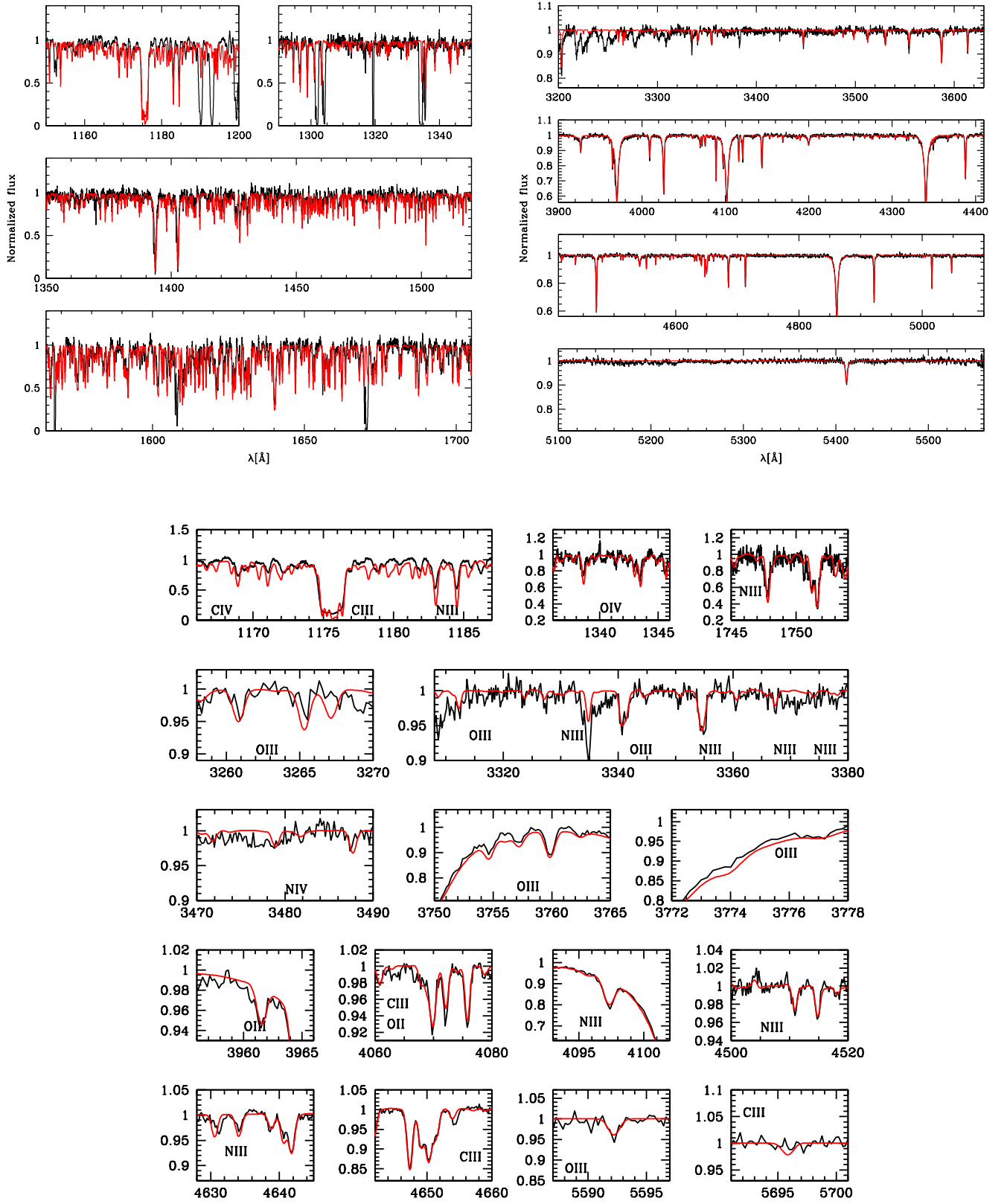


Fig. D.7. Same as Fig. D.2 but for AzV148.

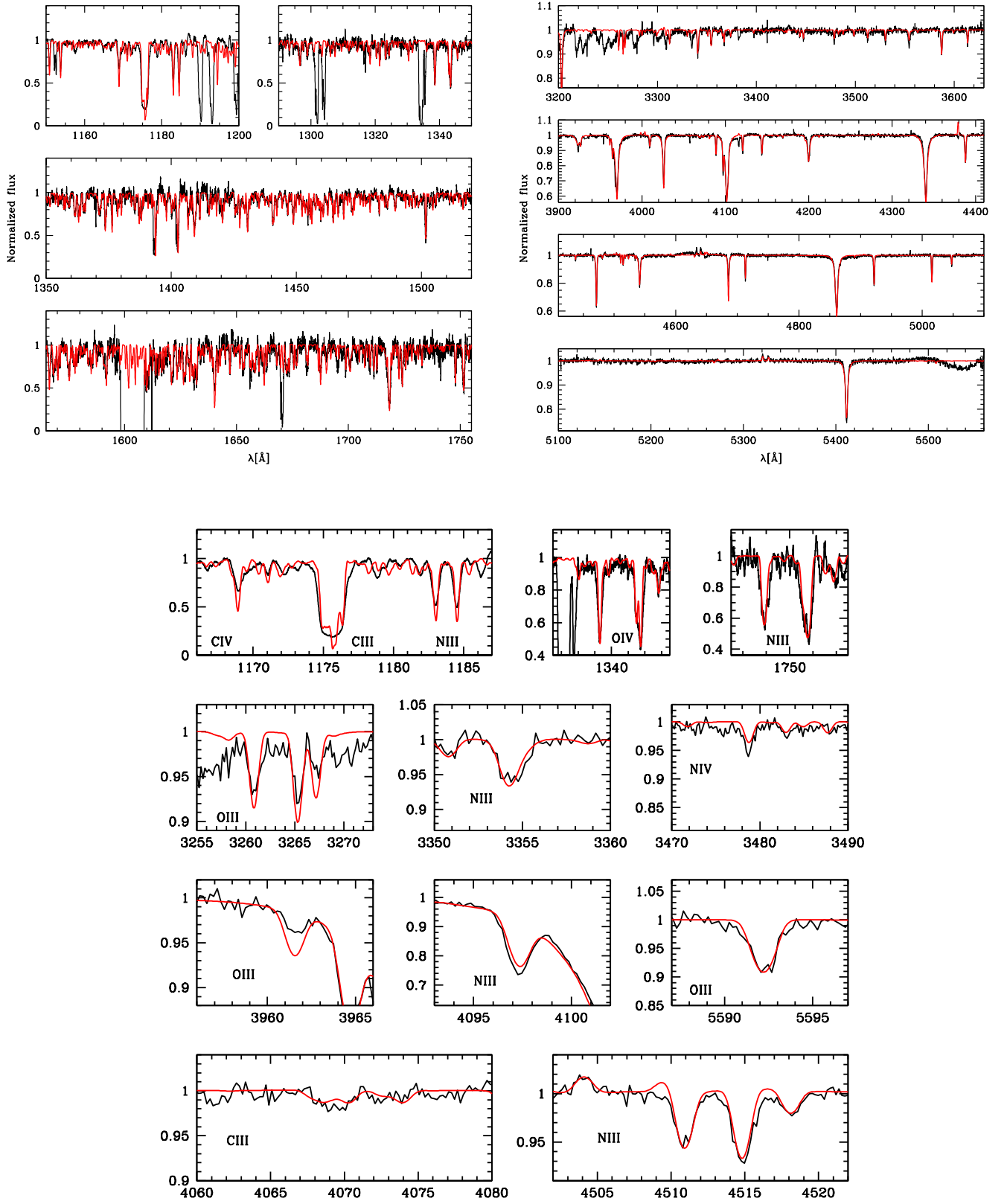


Fig. D.8. Same as Fig. D.2 but for AzV186.

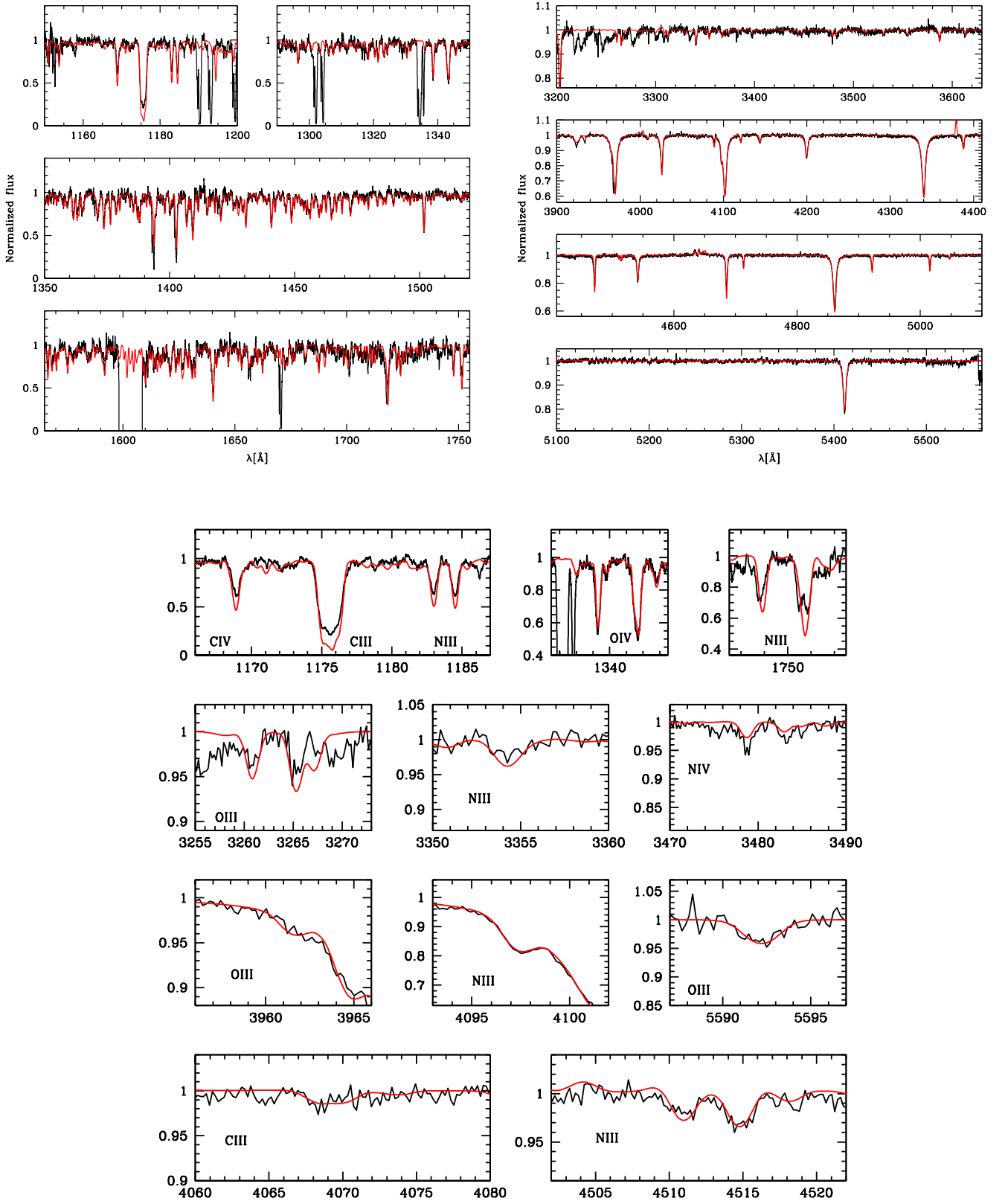


Fig. D.9. Same as Fig. D.2 but for AzV207.

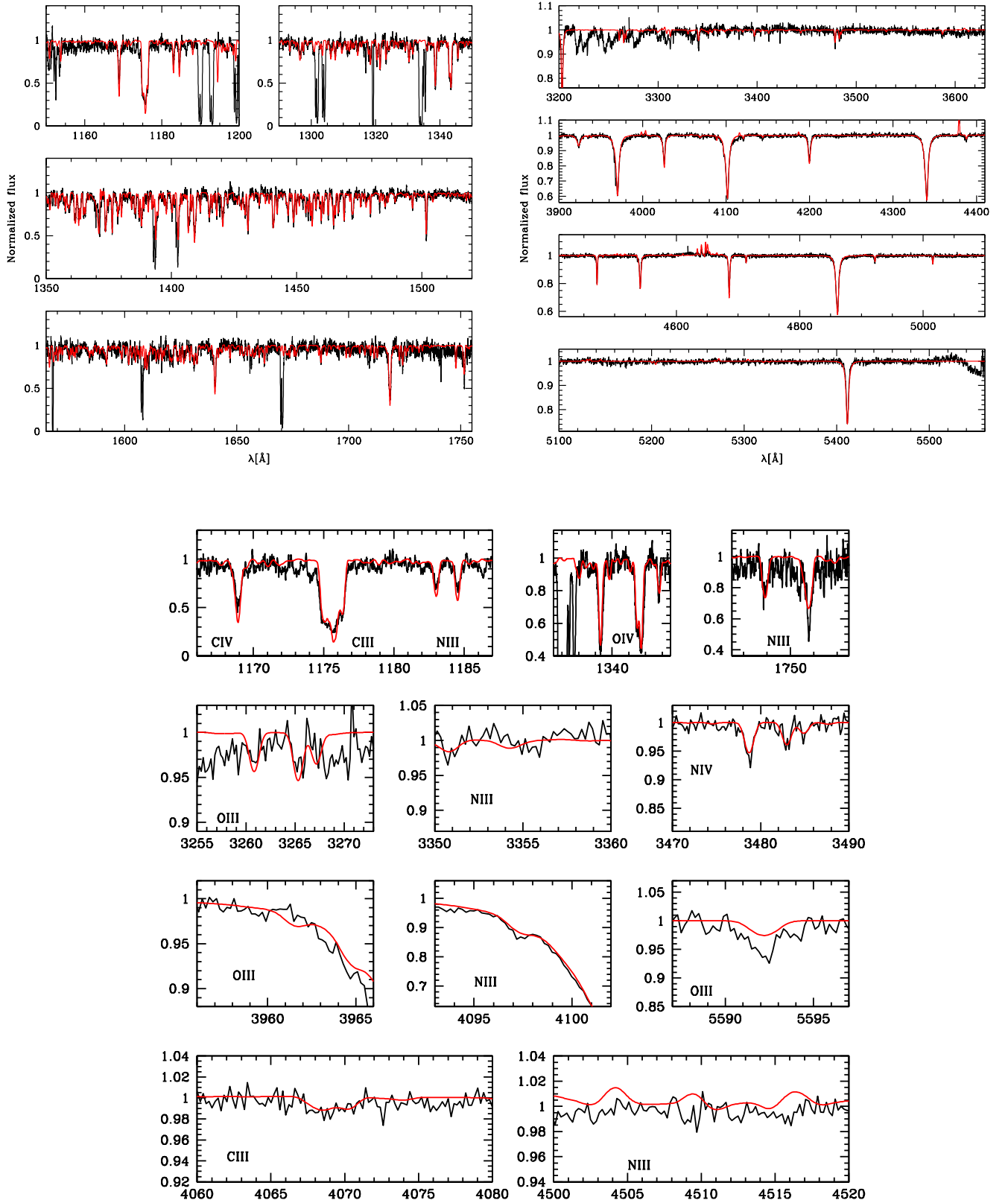


Fig. D.10. Same as Fig. D.2 but for AzV243.

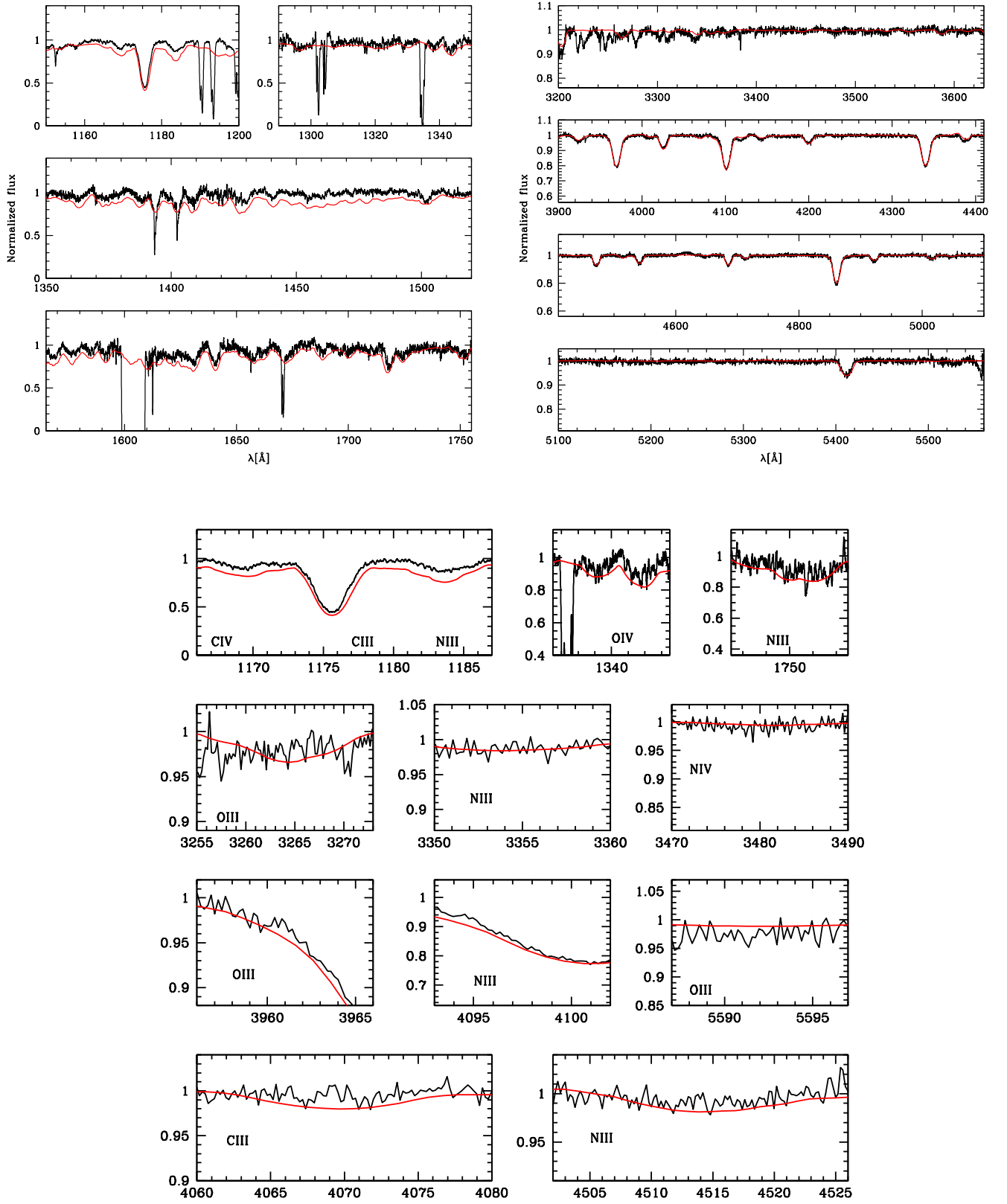


Fig. D.11. Same as Fig. D.2 but for AzV251.

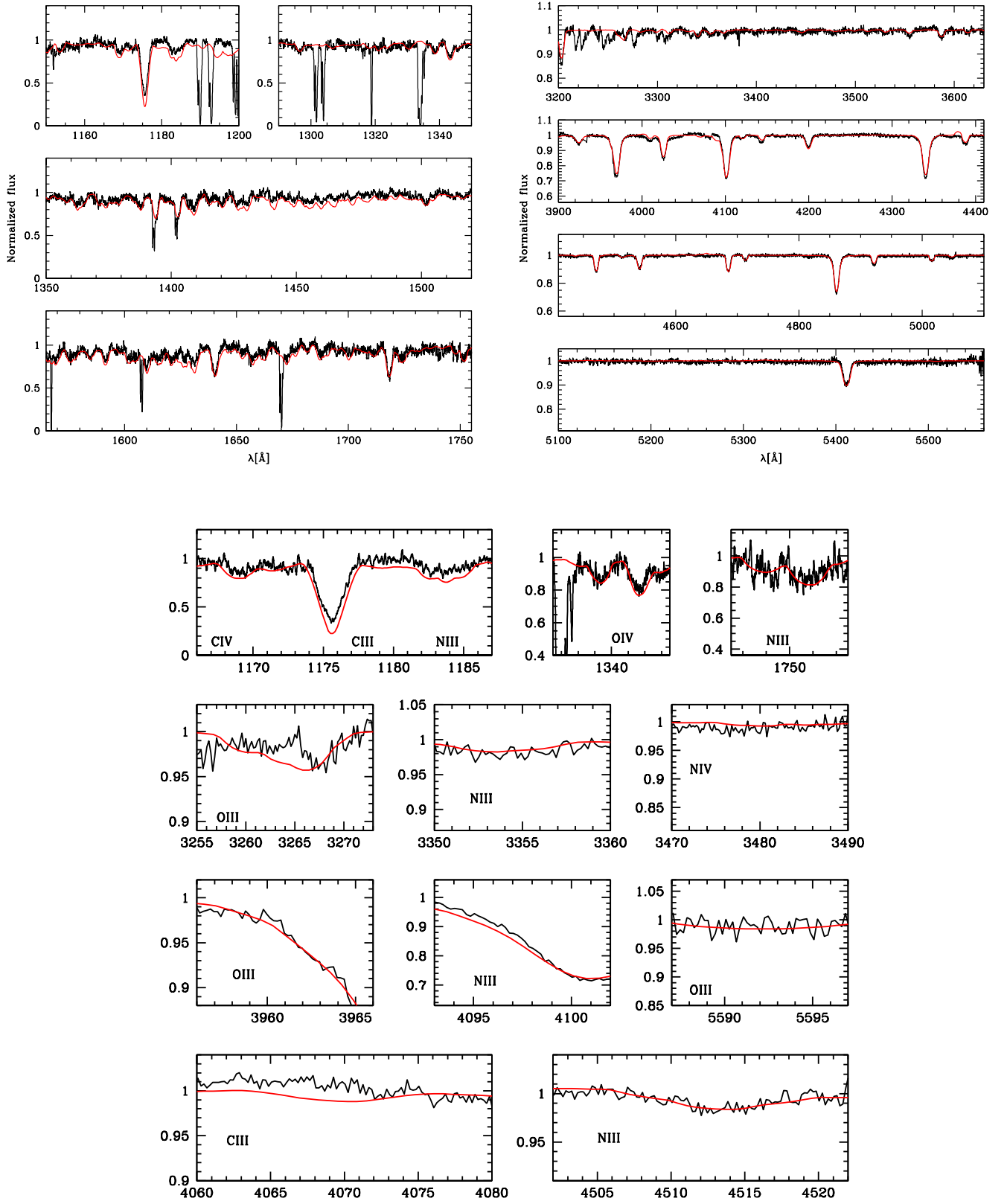


Fig. D.12. Same as Fig. D.2 but for AzV267.

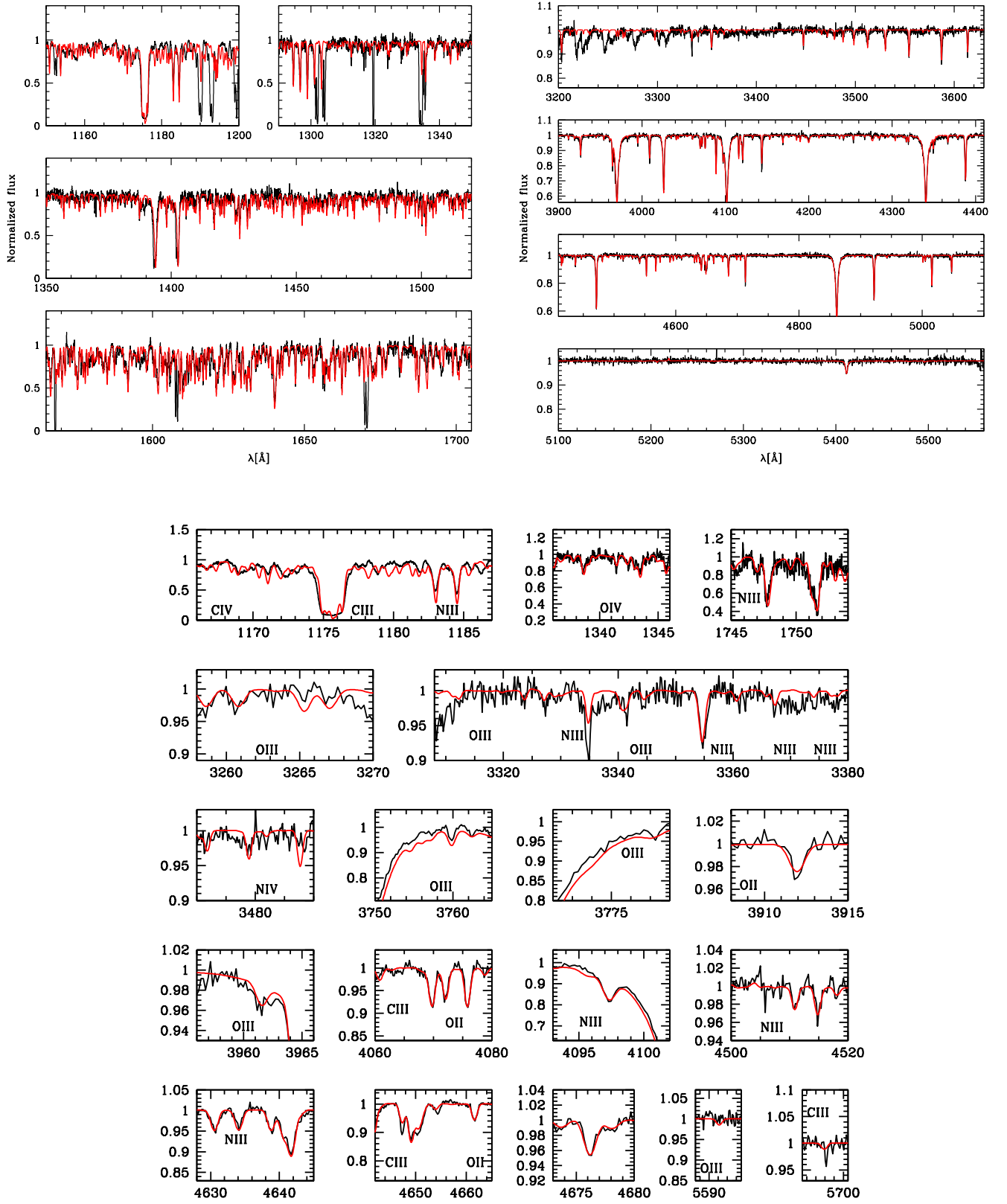


Fig. D.13. Same as Fig. D.2 but for AzV307.

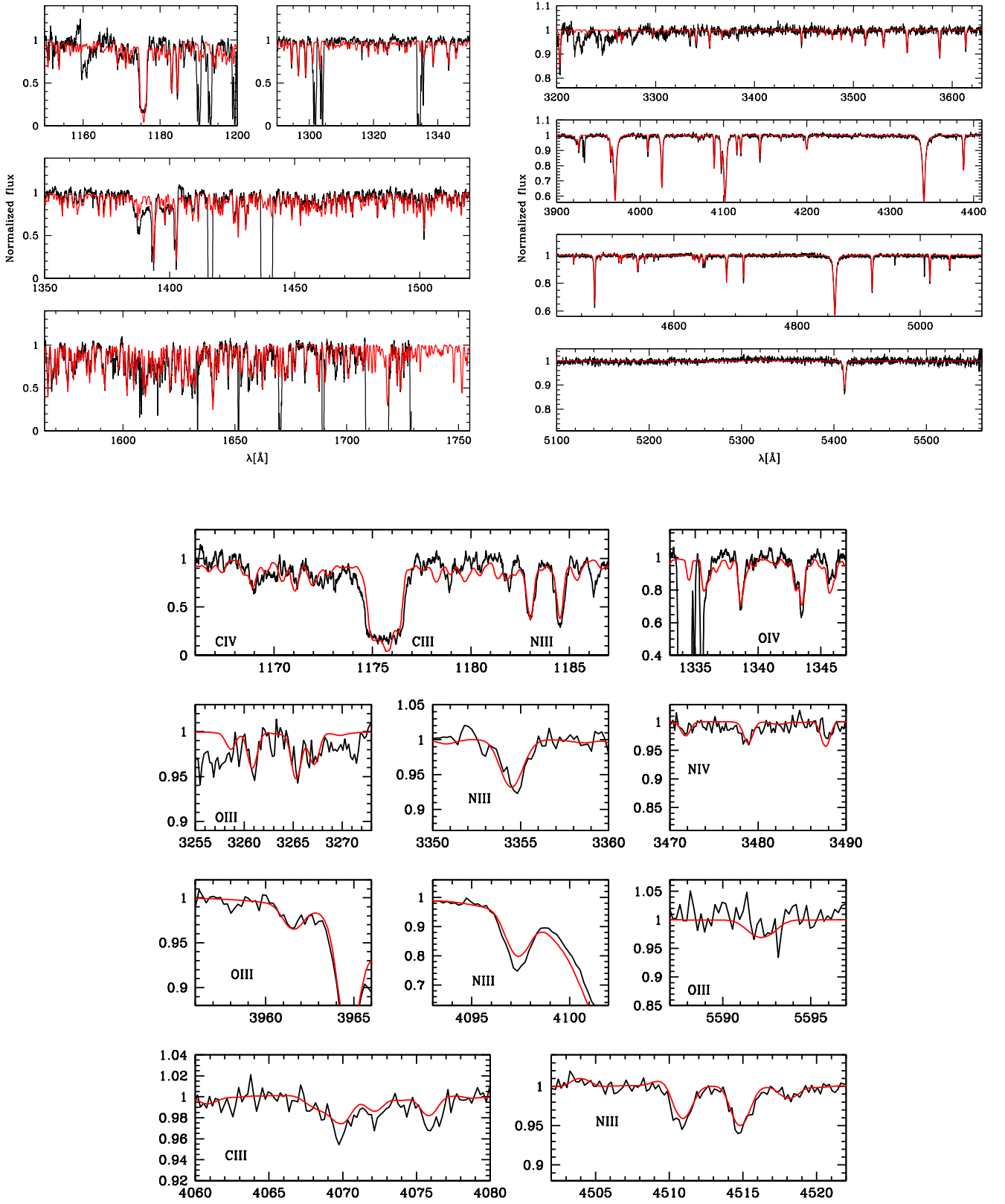


Fig. D.14. Same as Fig. D.2 but for AzV327.

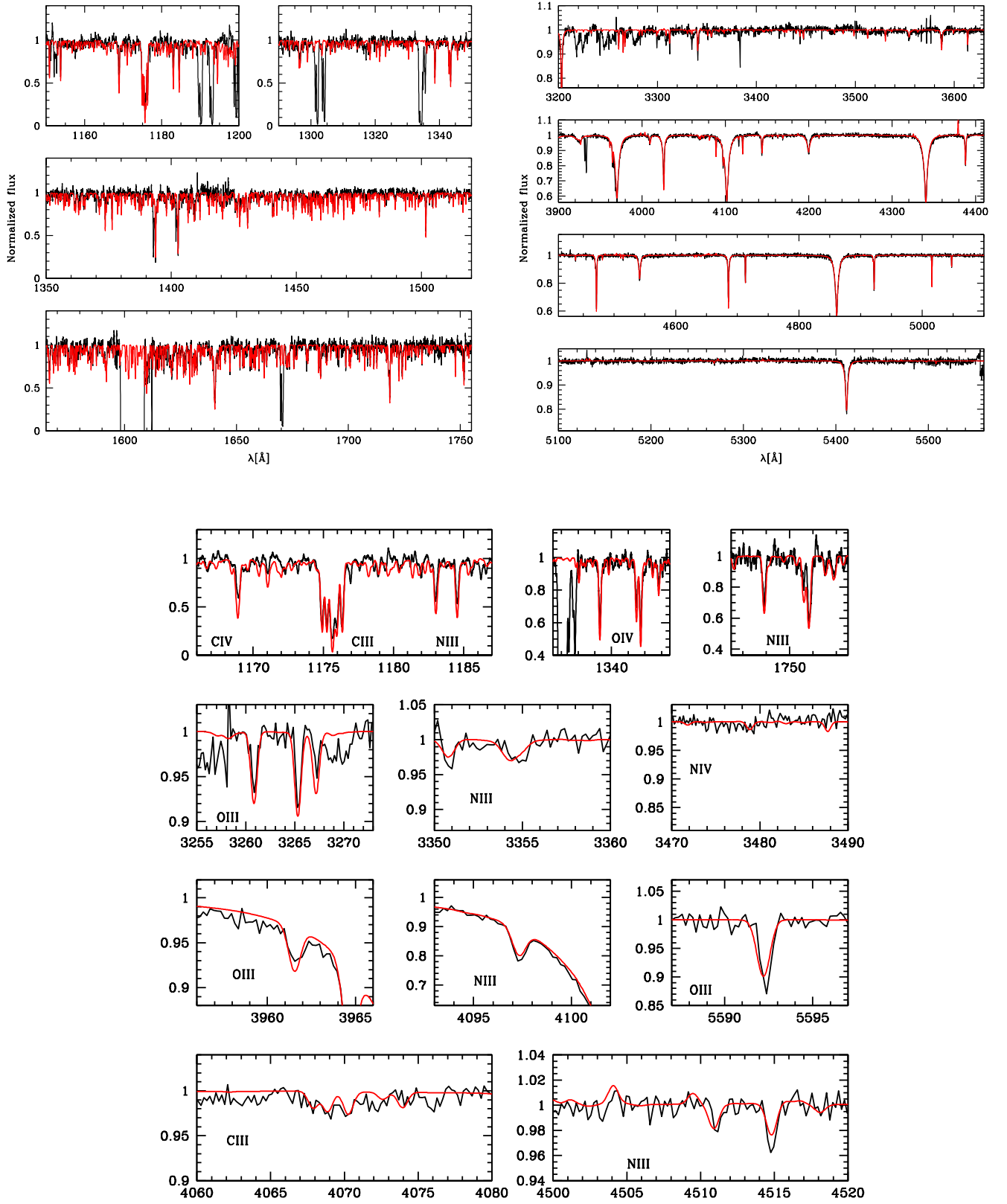


Fig. D.15. Same as Fig. D.2 but for AzV440.

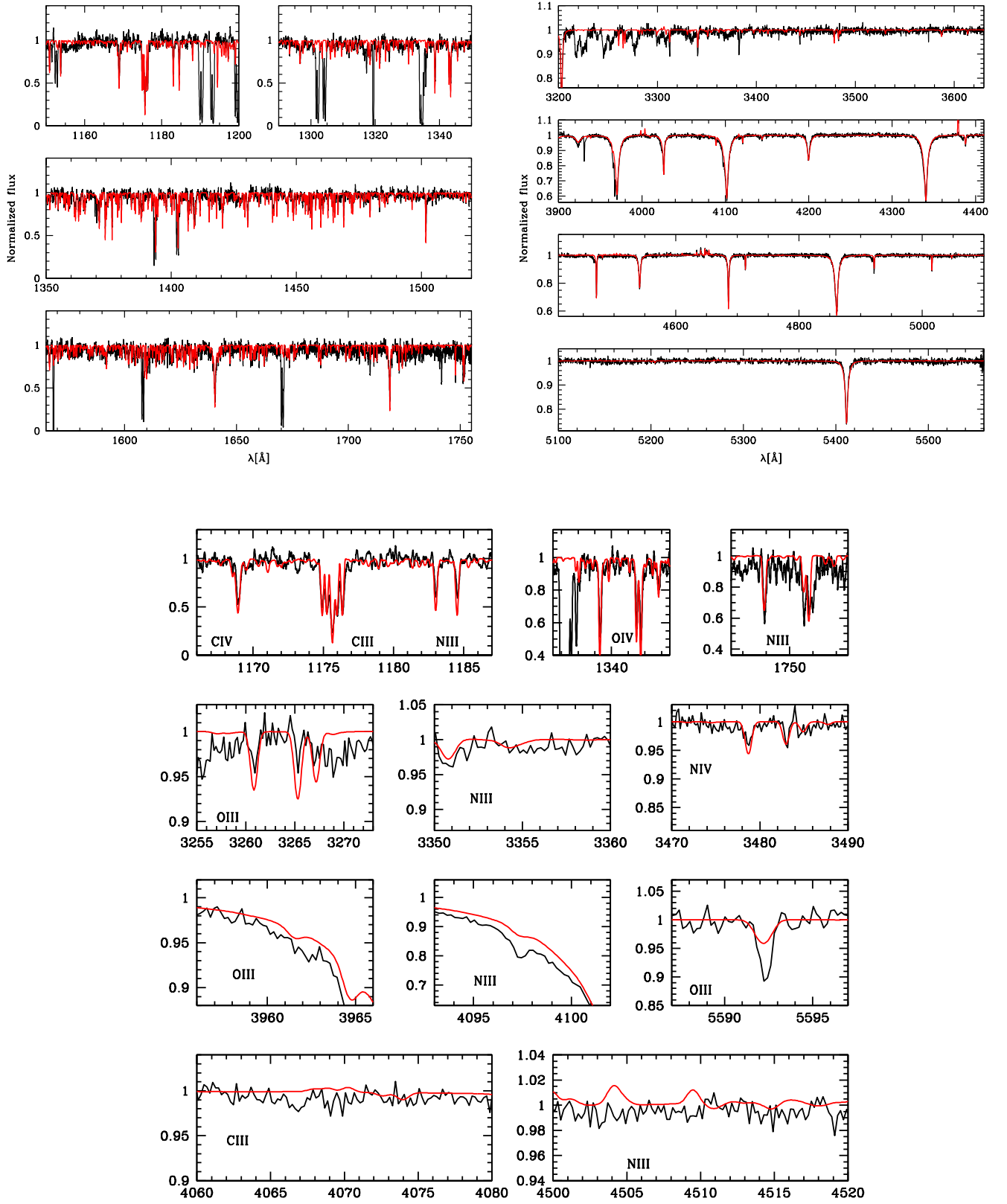


Fig. D.16. Same as Fig. D.2 but for AzV446.

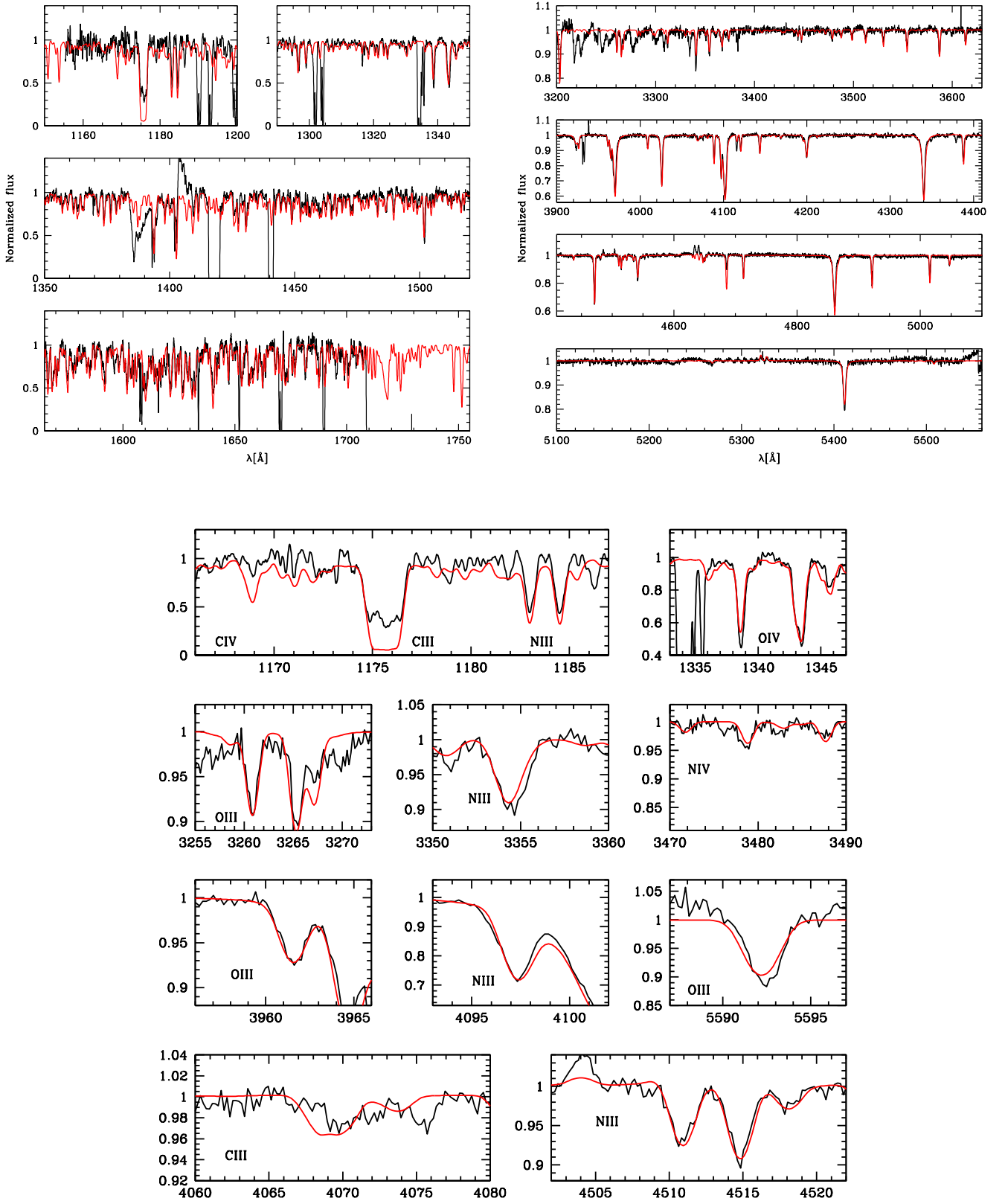


Fig. D.17. Same as Fig. D.2 but for AzV469.

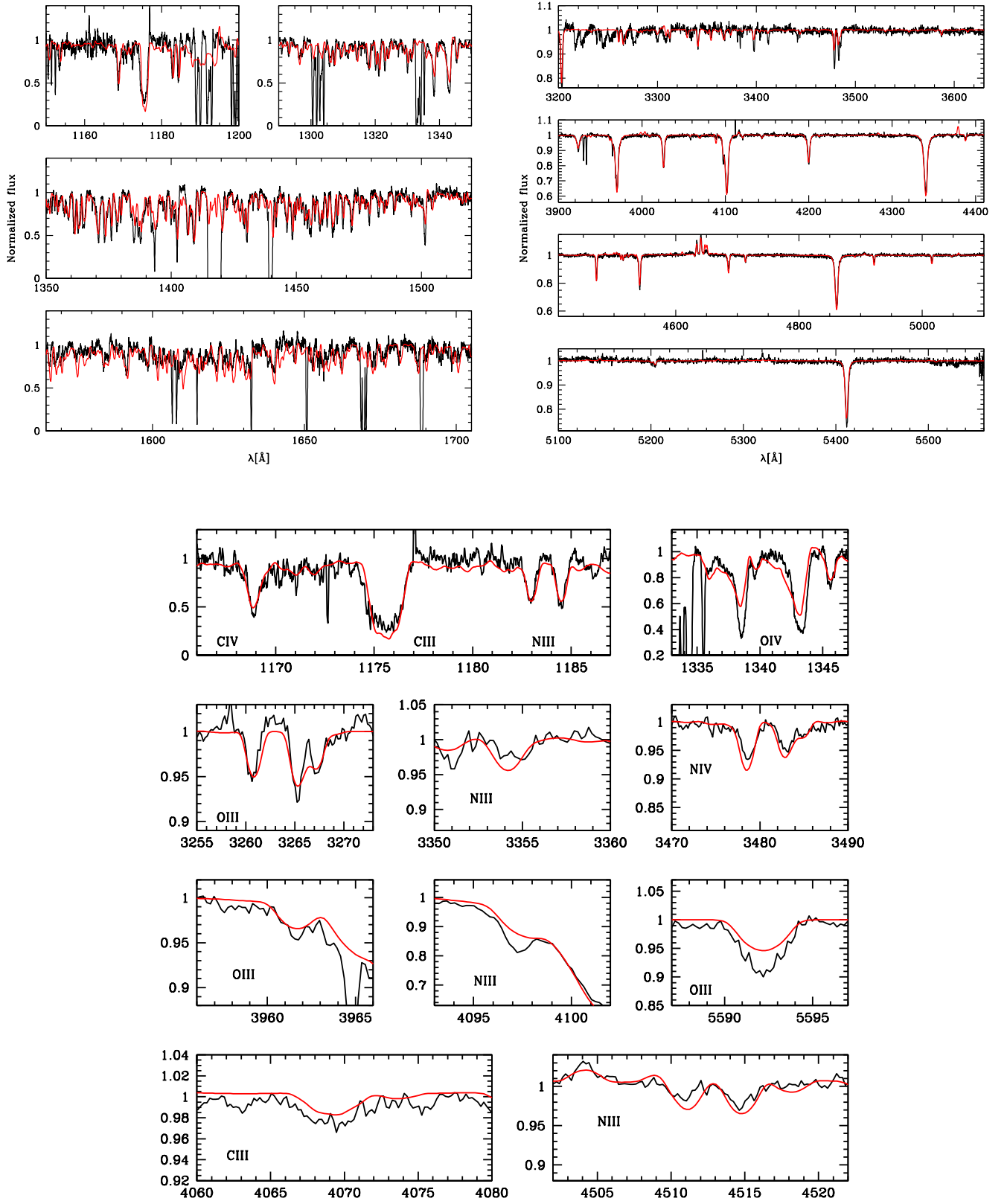


Fig. D.18. Same as Fig. D.2 but for SK -66° 18.

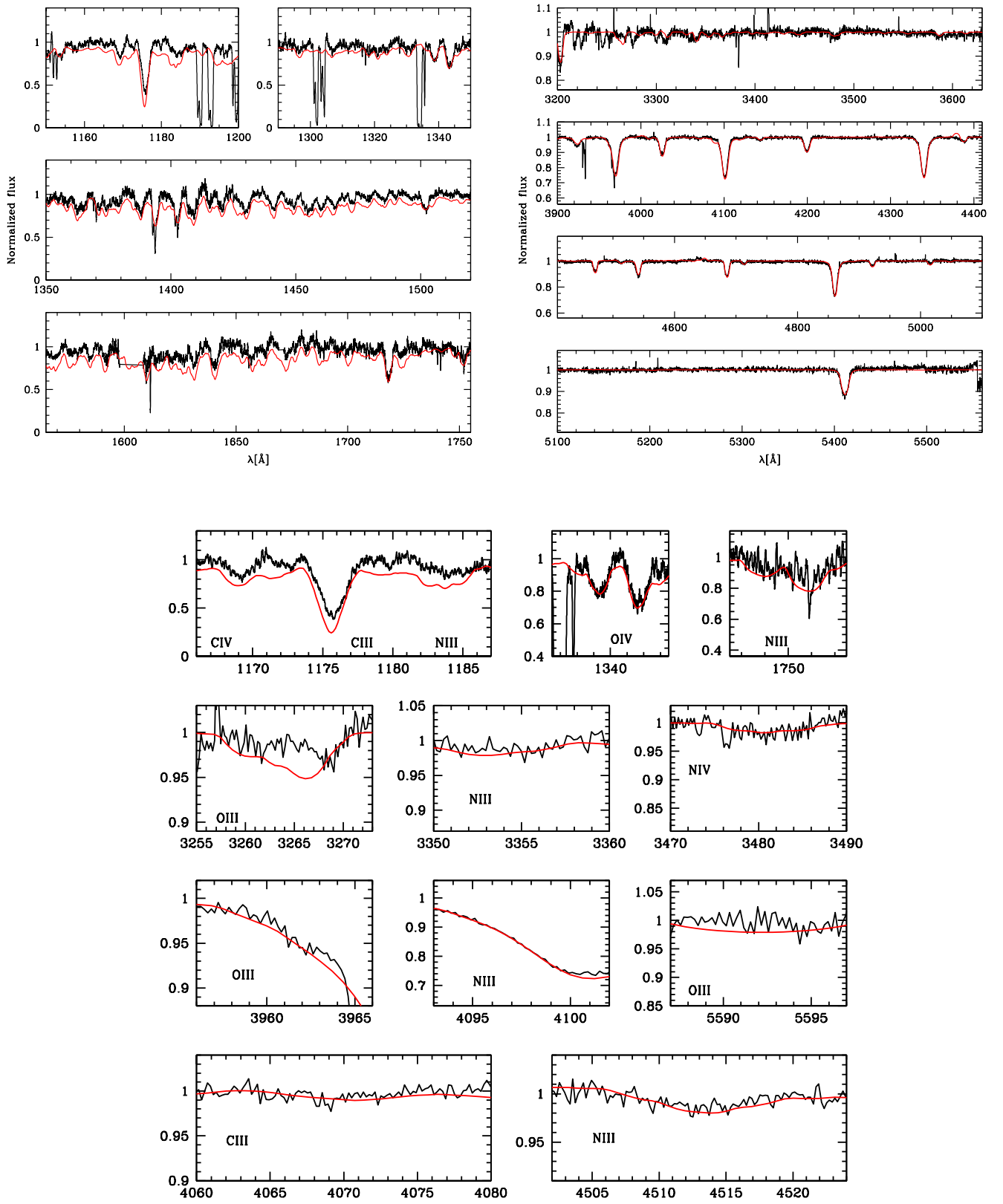


Fig. D.19. Same as Fig. D.2 but for SK -71° 19.

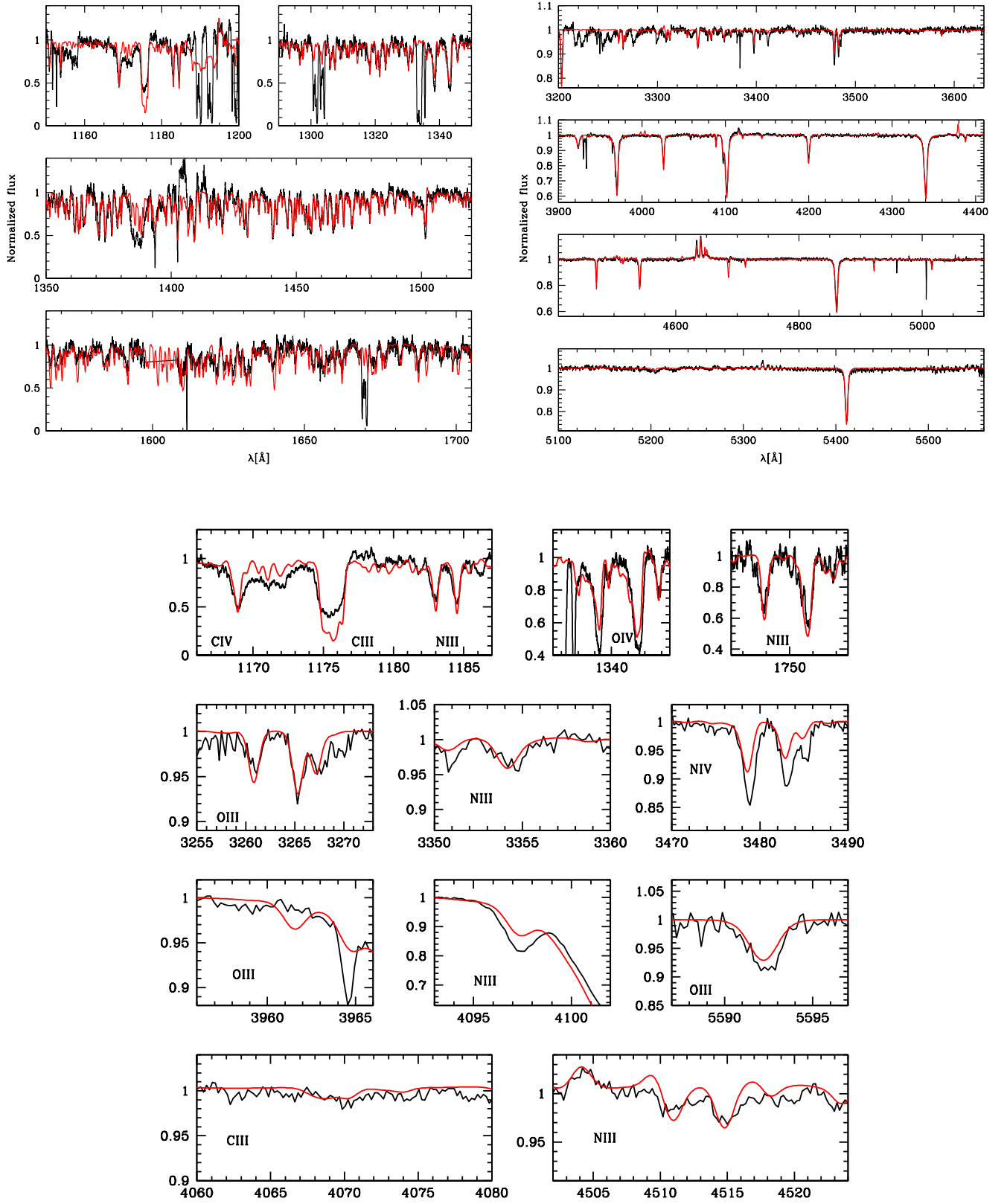


Fig. D.20. Same as Fig. D.2 but for N11 018.

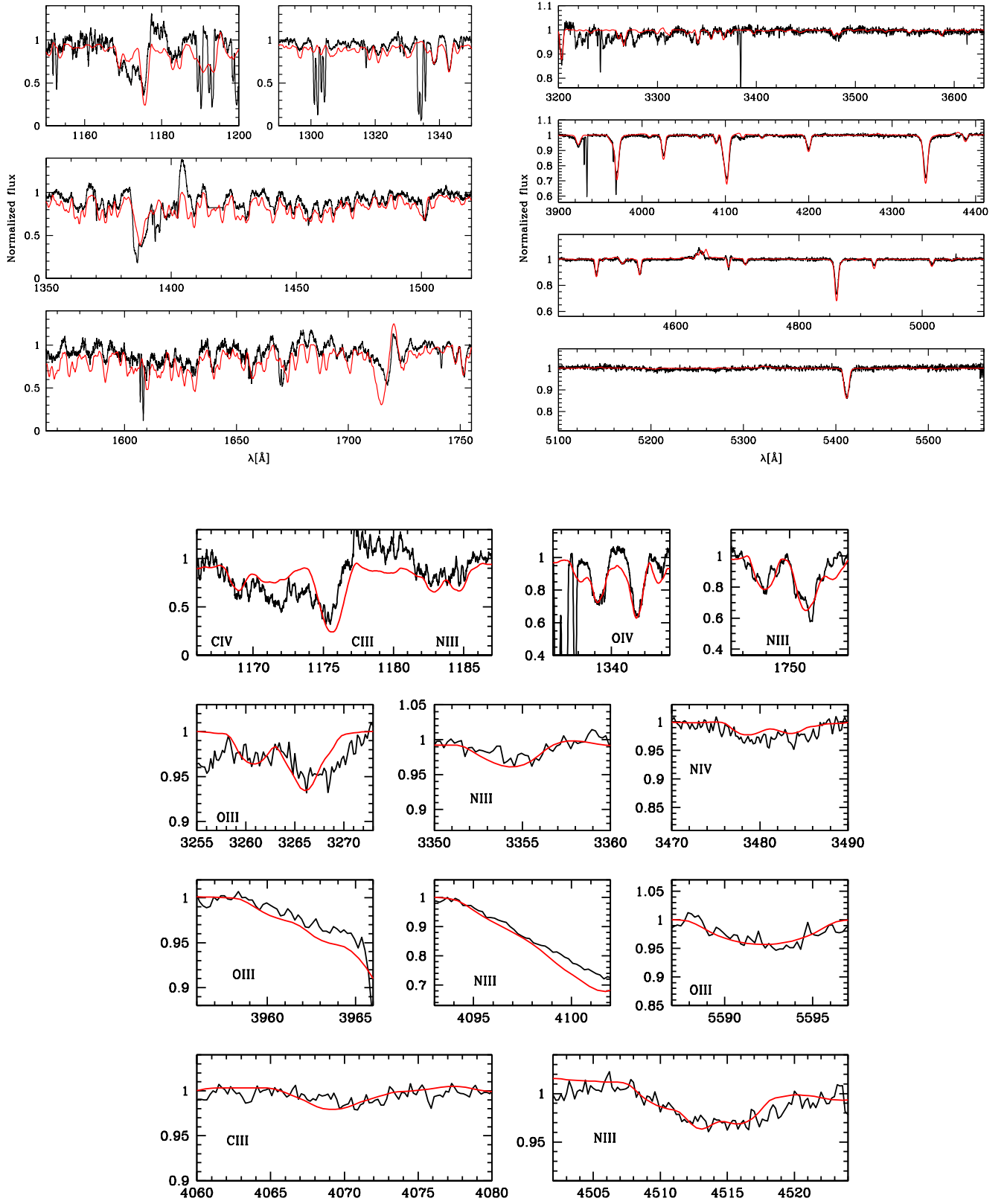


Fig. D.21. Same as Fig. D.2 but for SK $-71^\circ 50$.

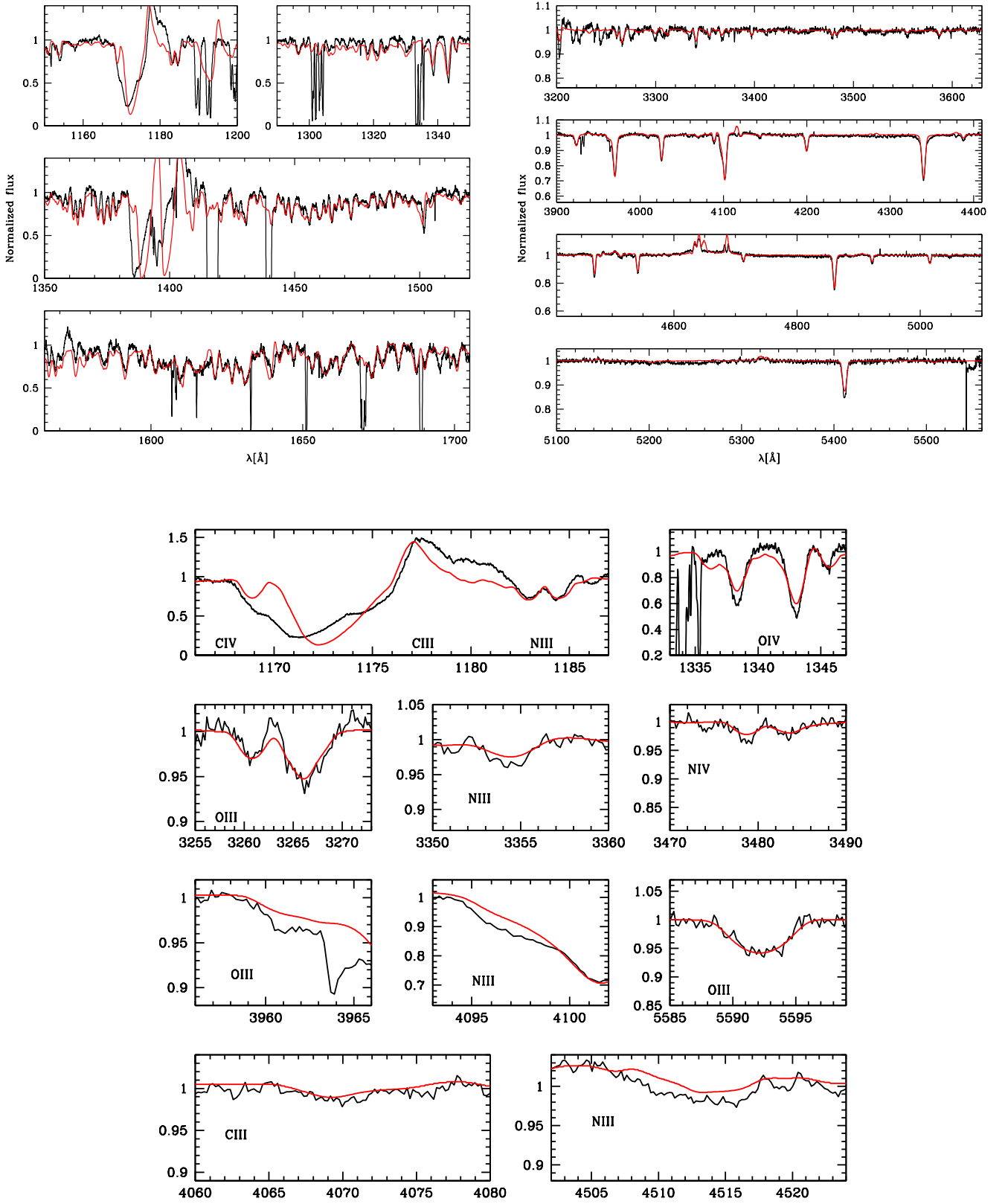


Fig. D.22. Same as Fig. D.2 but for SK -66° 152.

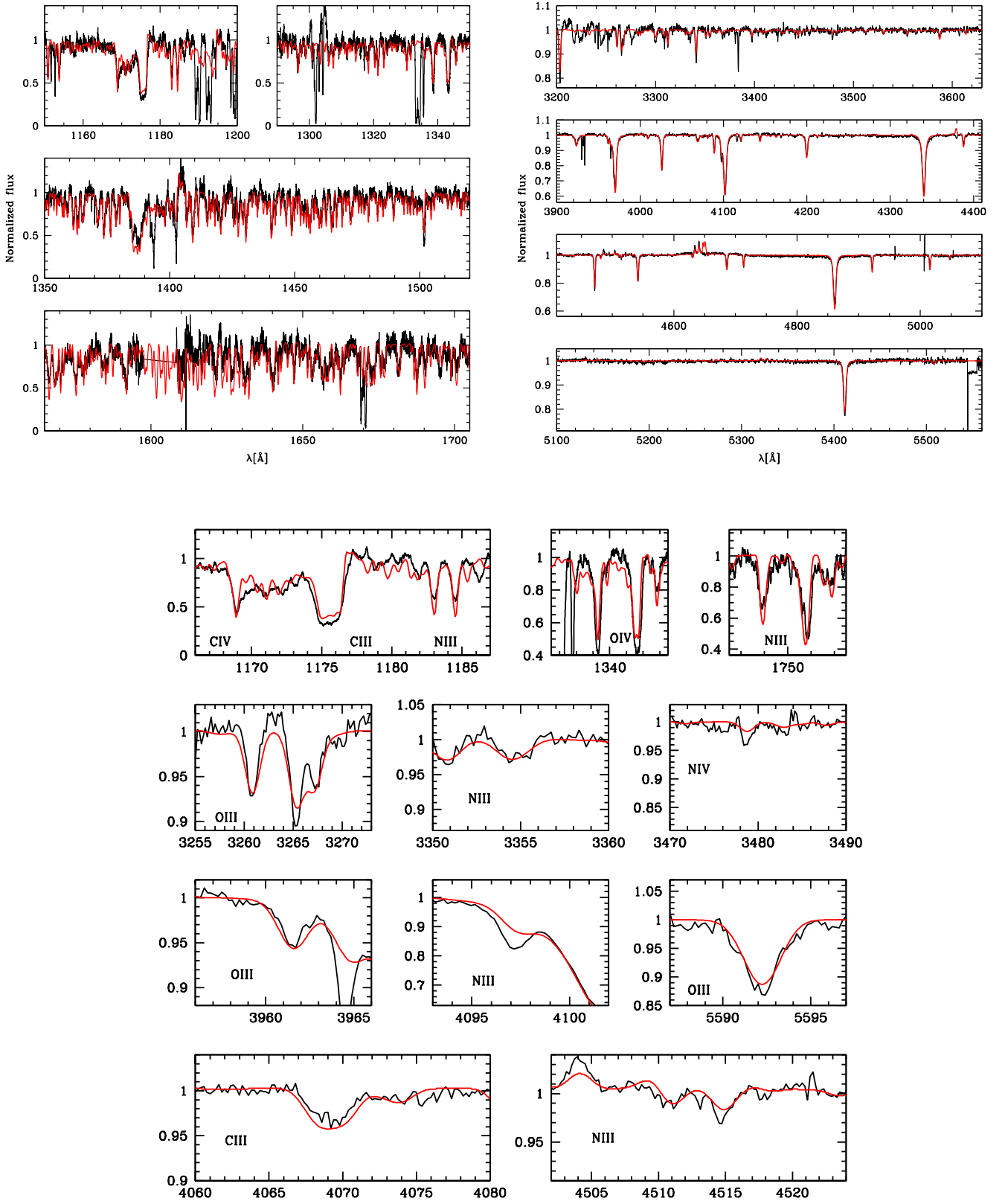


Fig. D.23. Same as Fig. D.2 but for N11 032.

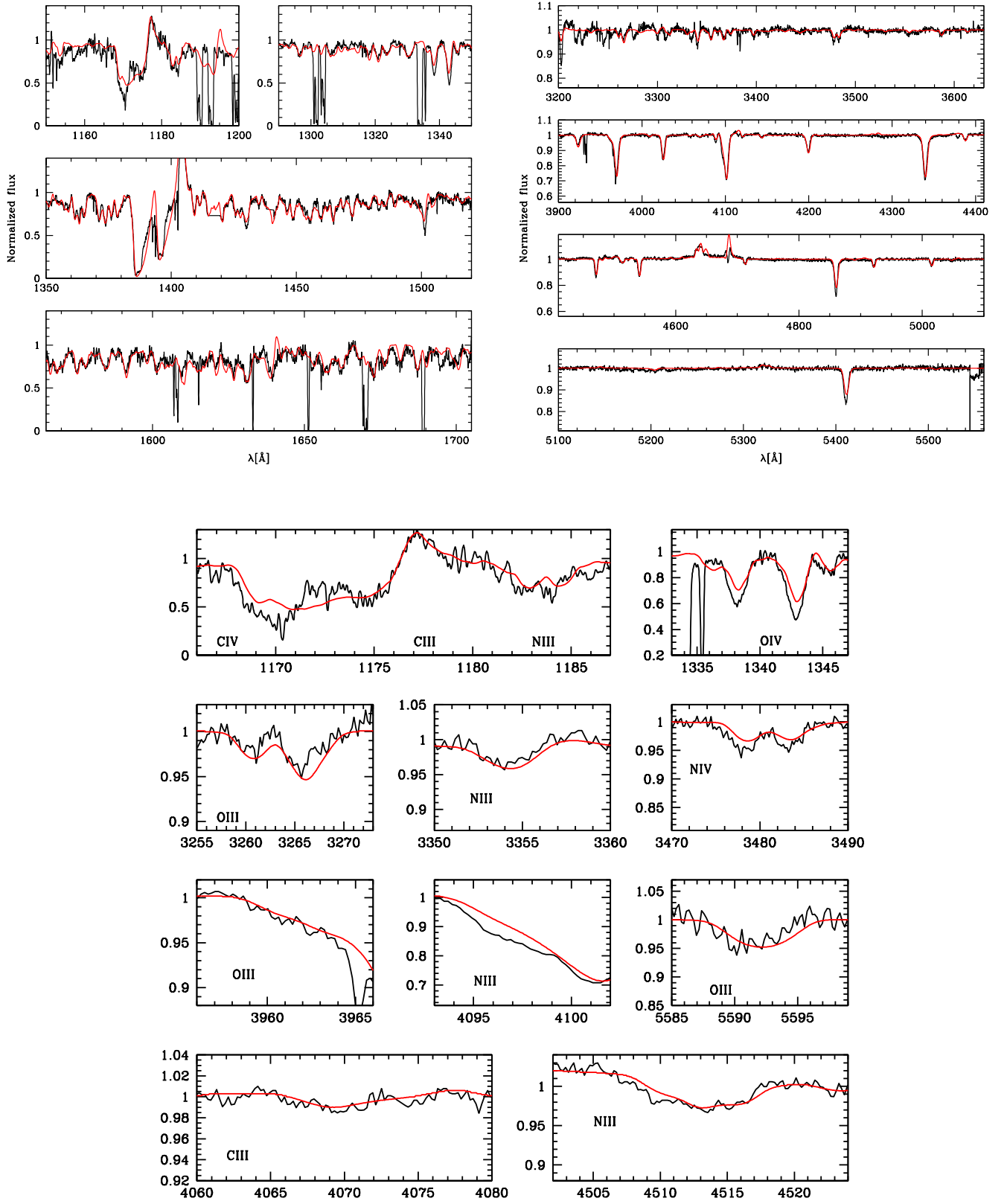


Fig. D.24. Same as Fig. D.2 but for SK -69° 50.

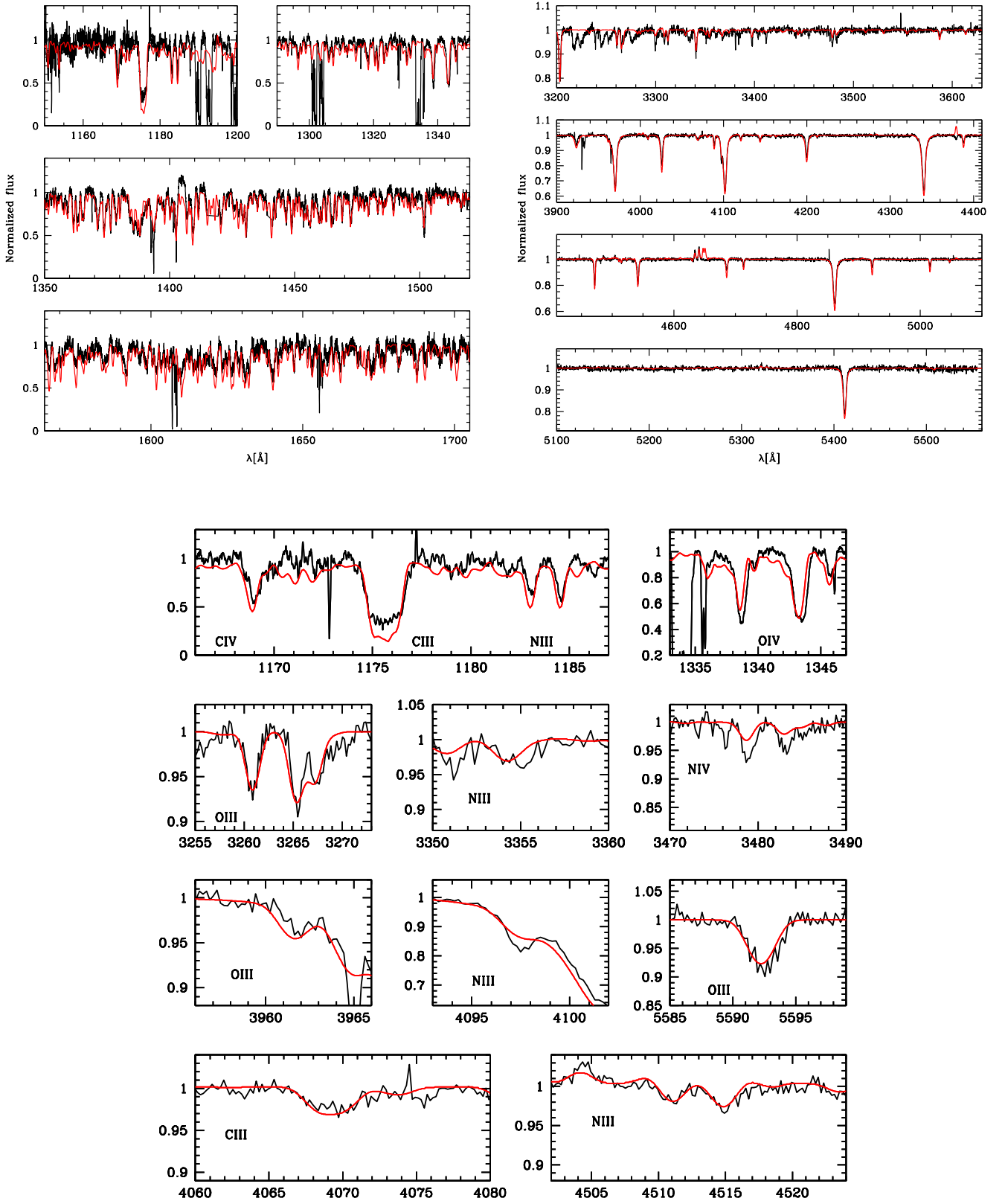


Fig. D.25. Same as Fig. D.2 but for SK -68° 16.

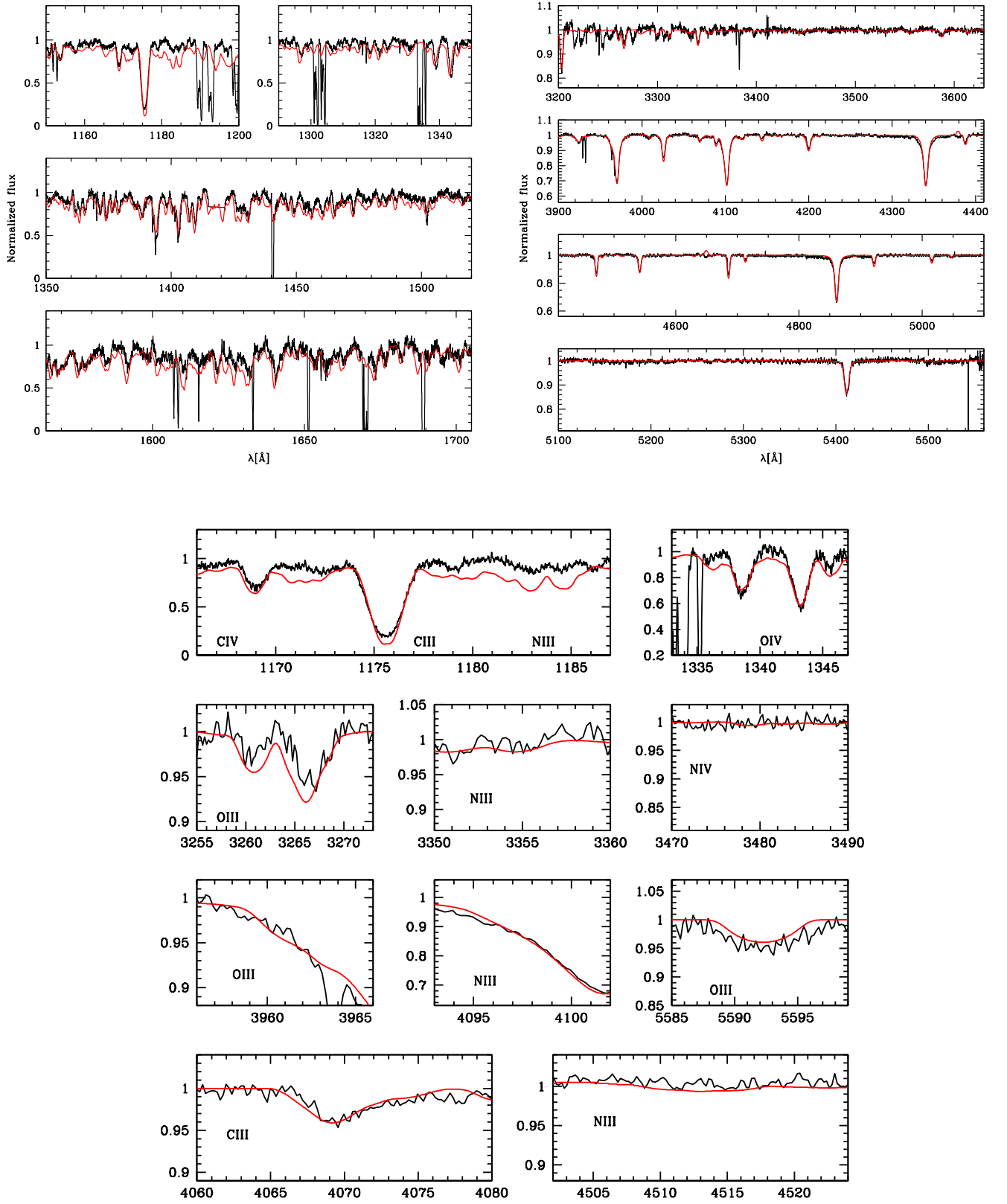


Fig. D.26. Same as Fig. D.2 but for N11 049.

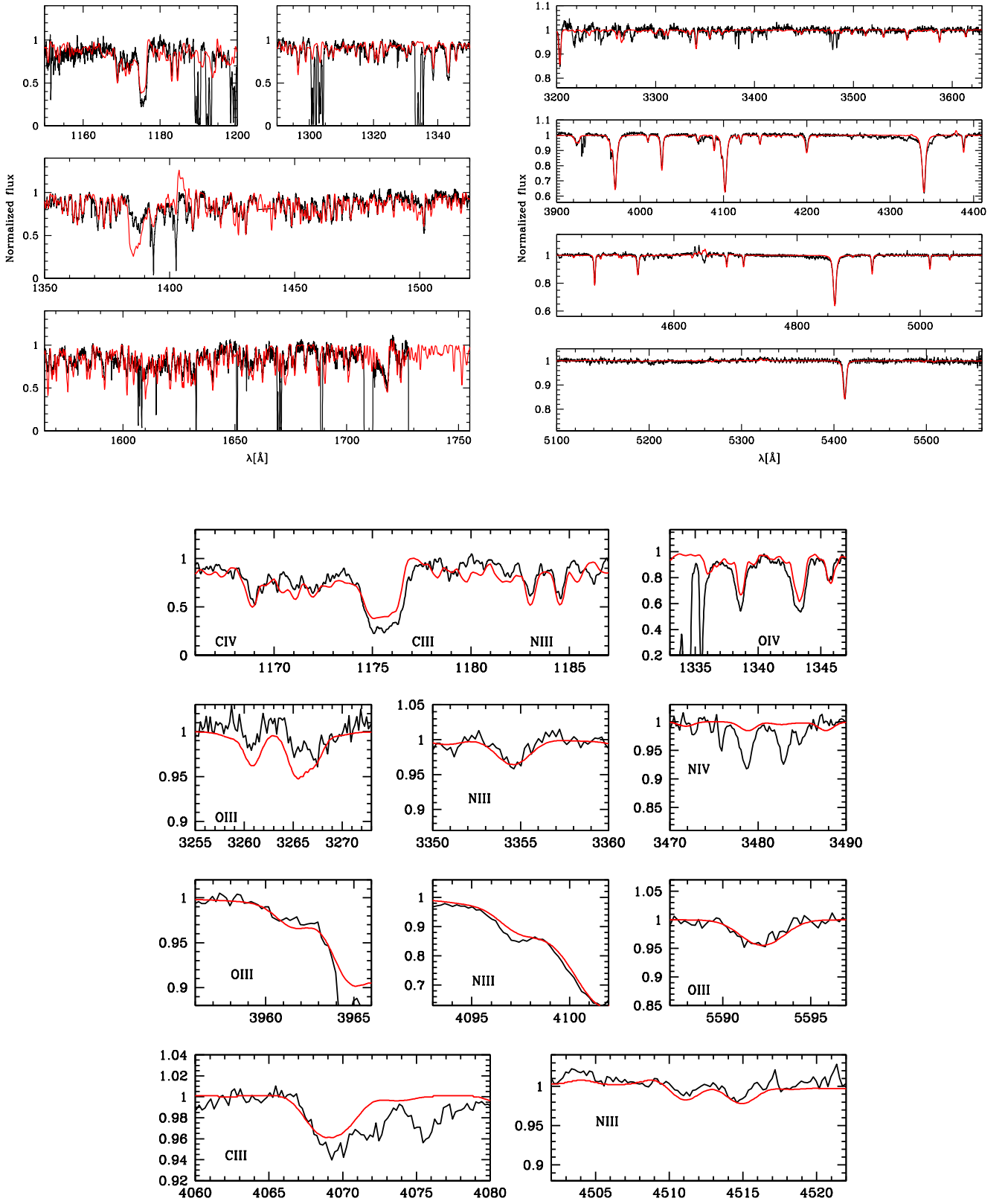


Fig. D.27. Same as Fig. D.2 but for SK -67° 101.

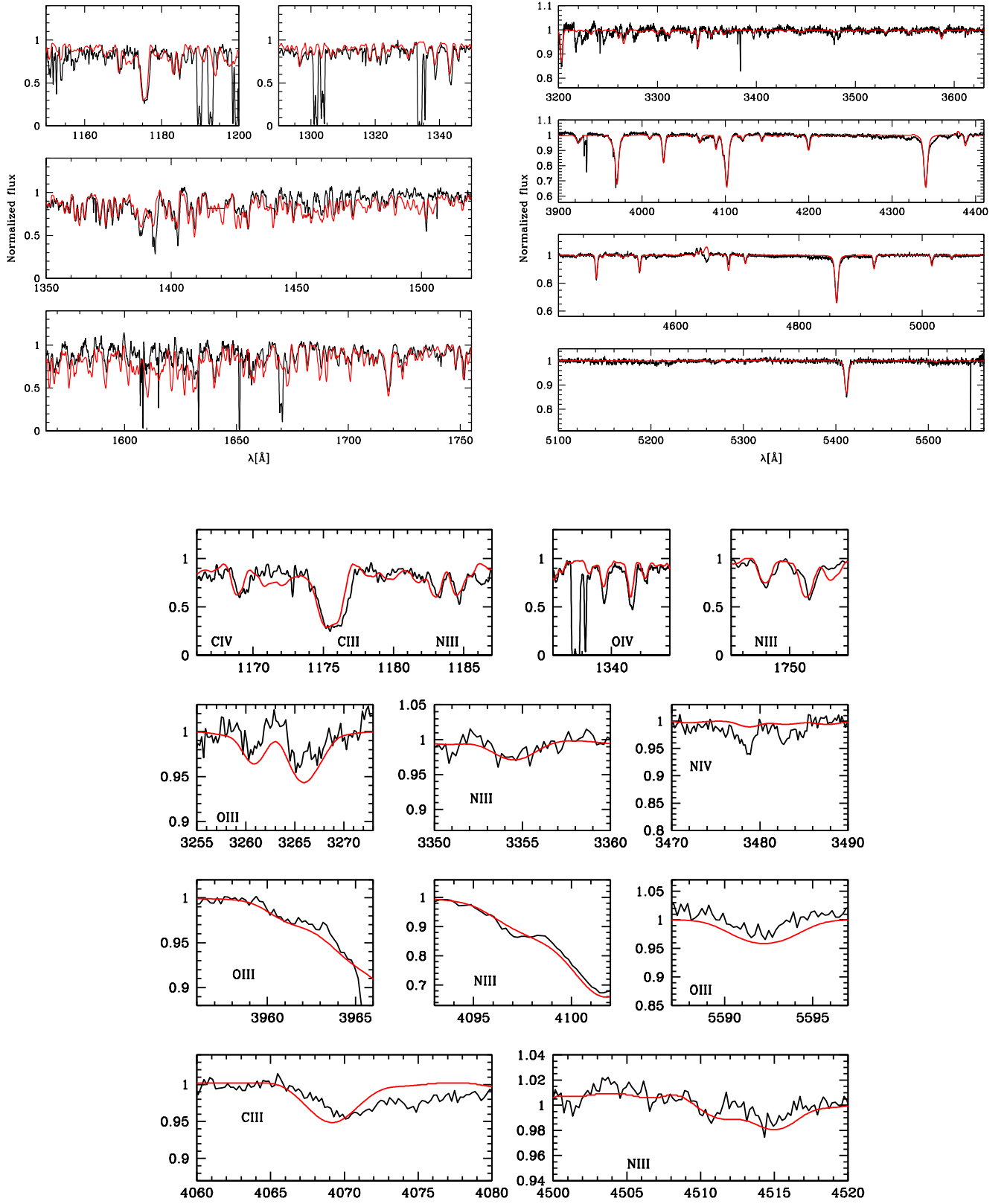


Fig. D.28. Same as Fig. D.2 but for BI 173.

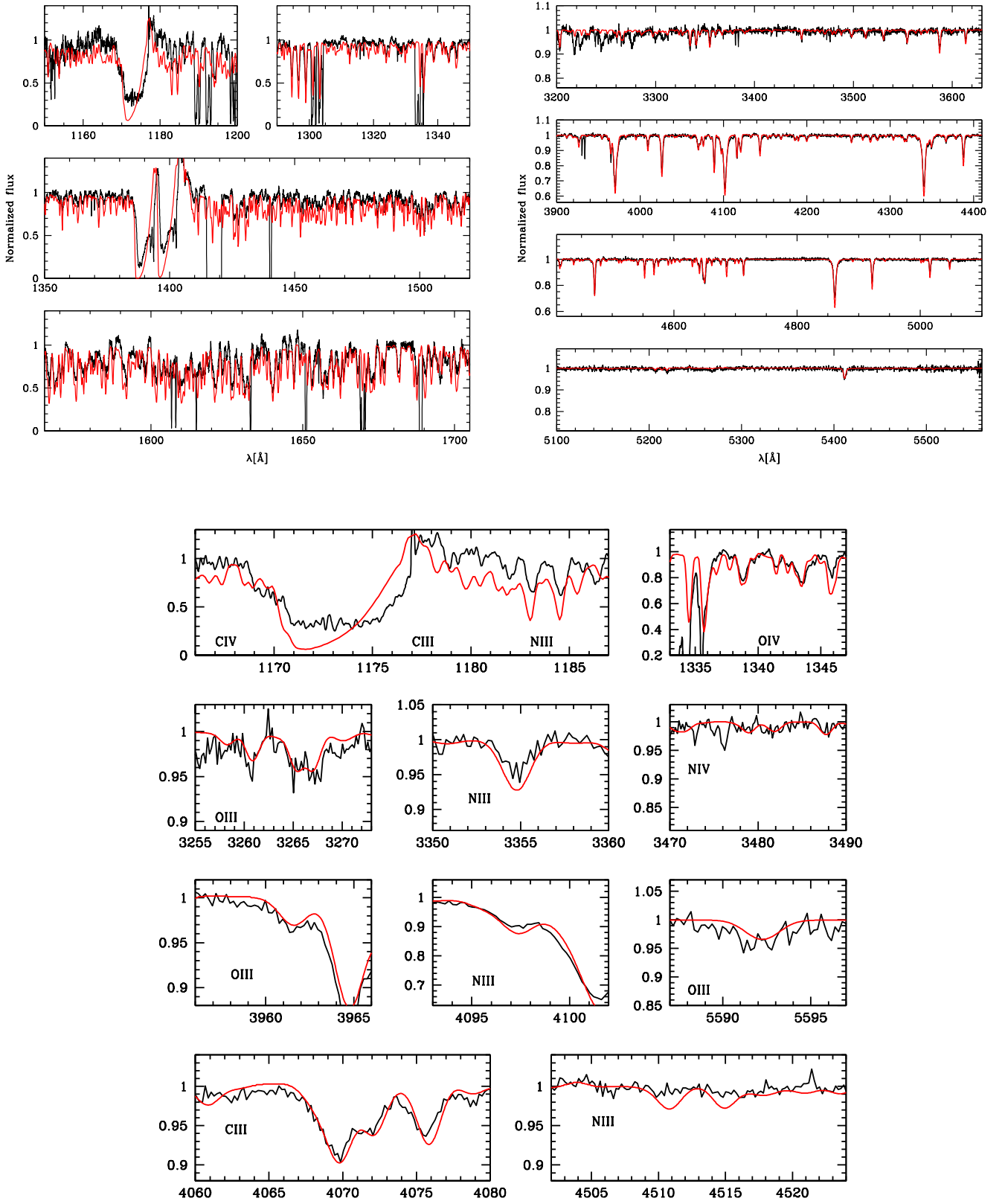


Fig. D.29. Same as Fig. D.2 but for SK -67° 261.

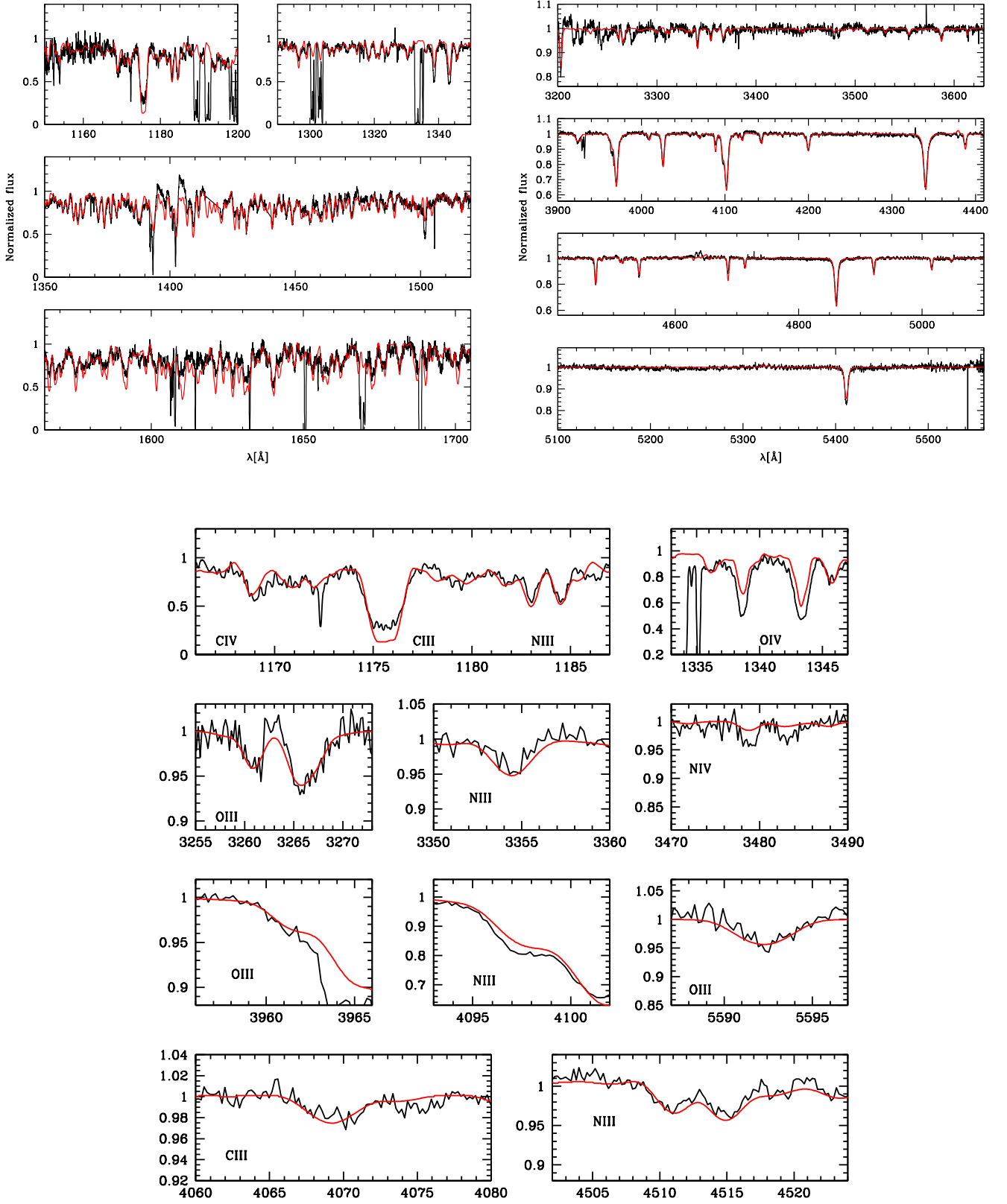


Fig. D.30. Same as Fig. D.2 but for SK -67° 191.

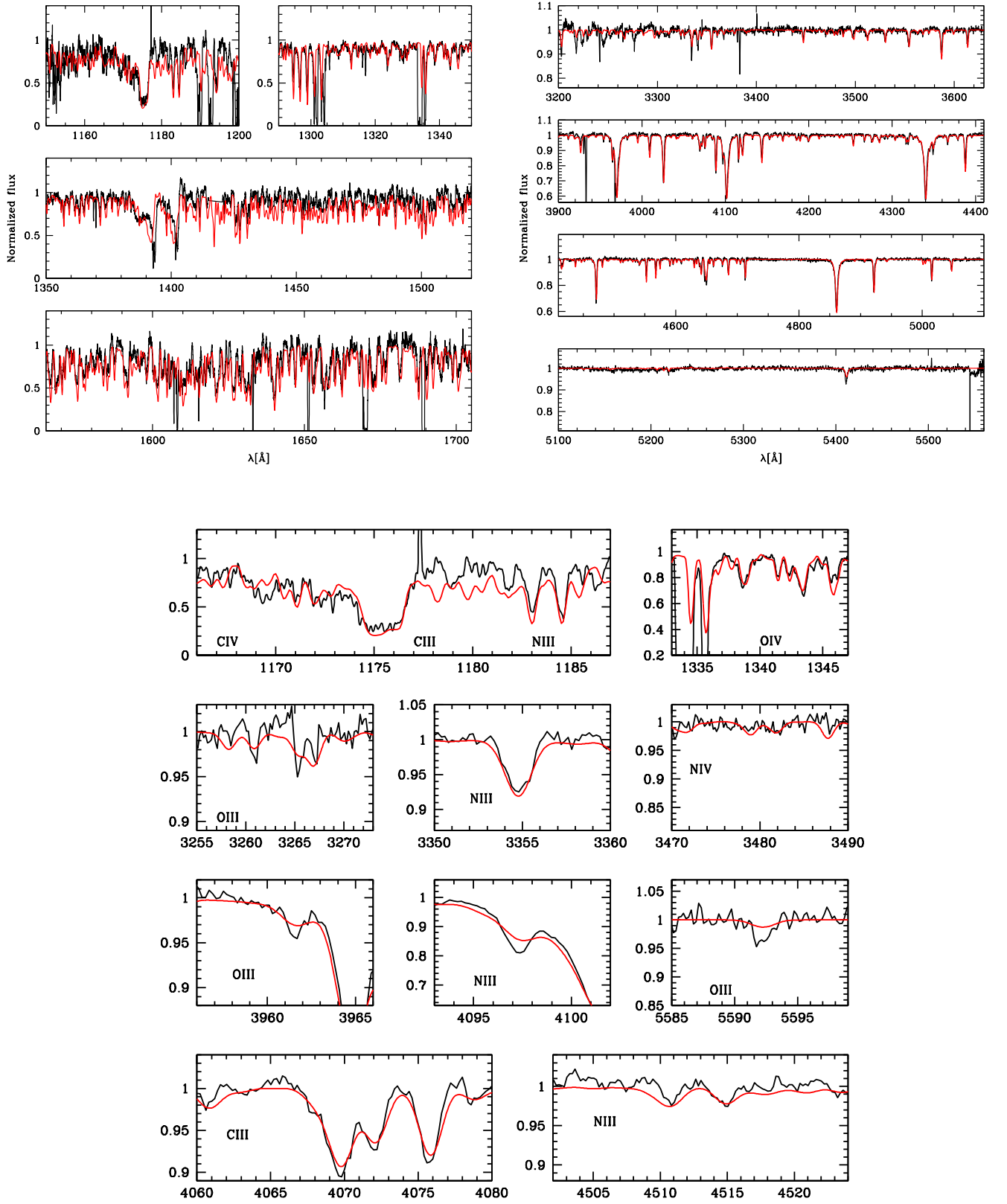


Fig. D.32. Same as Fig. D.2 but for SK -71° 8.

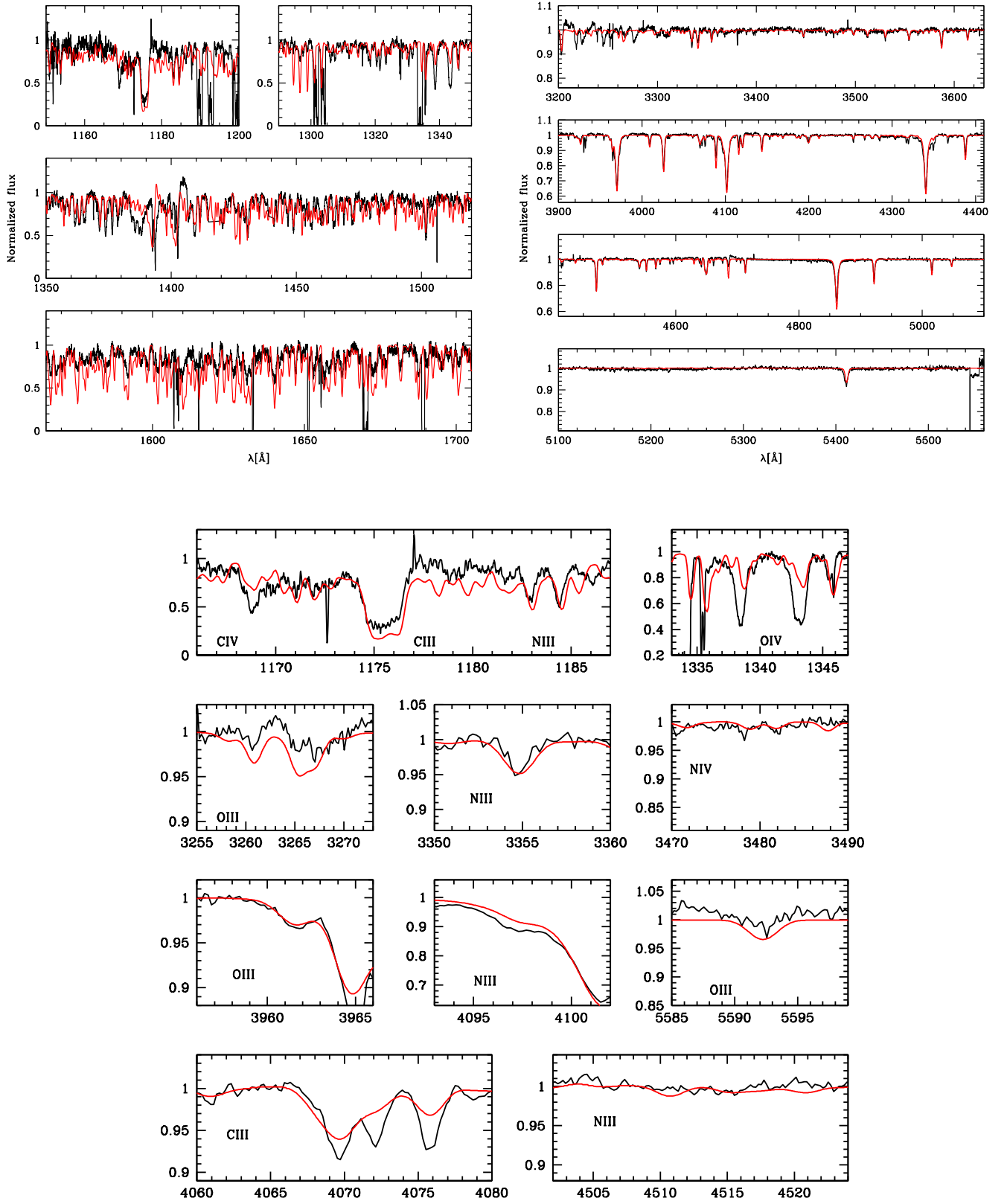


Fig. D.33. Same as Fig. D.2 but for SK -70° 13.

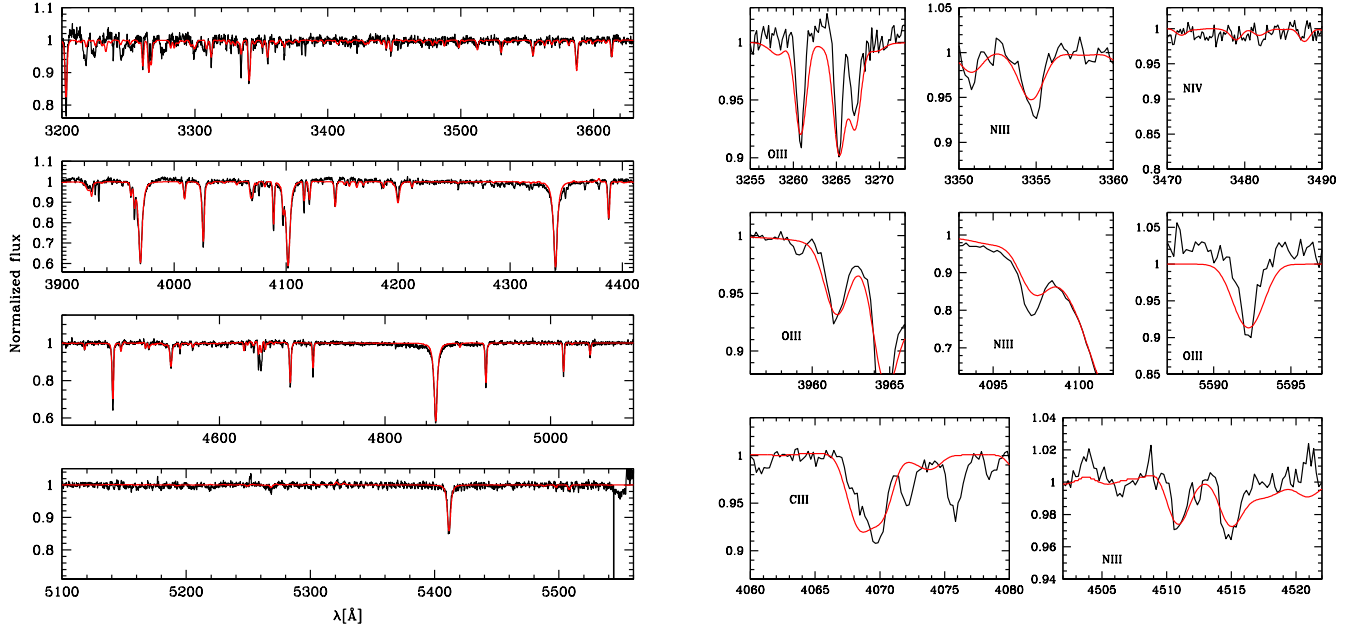
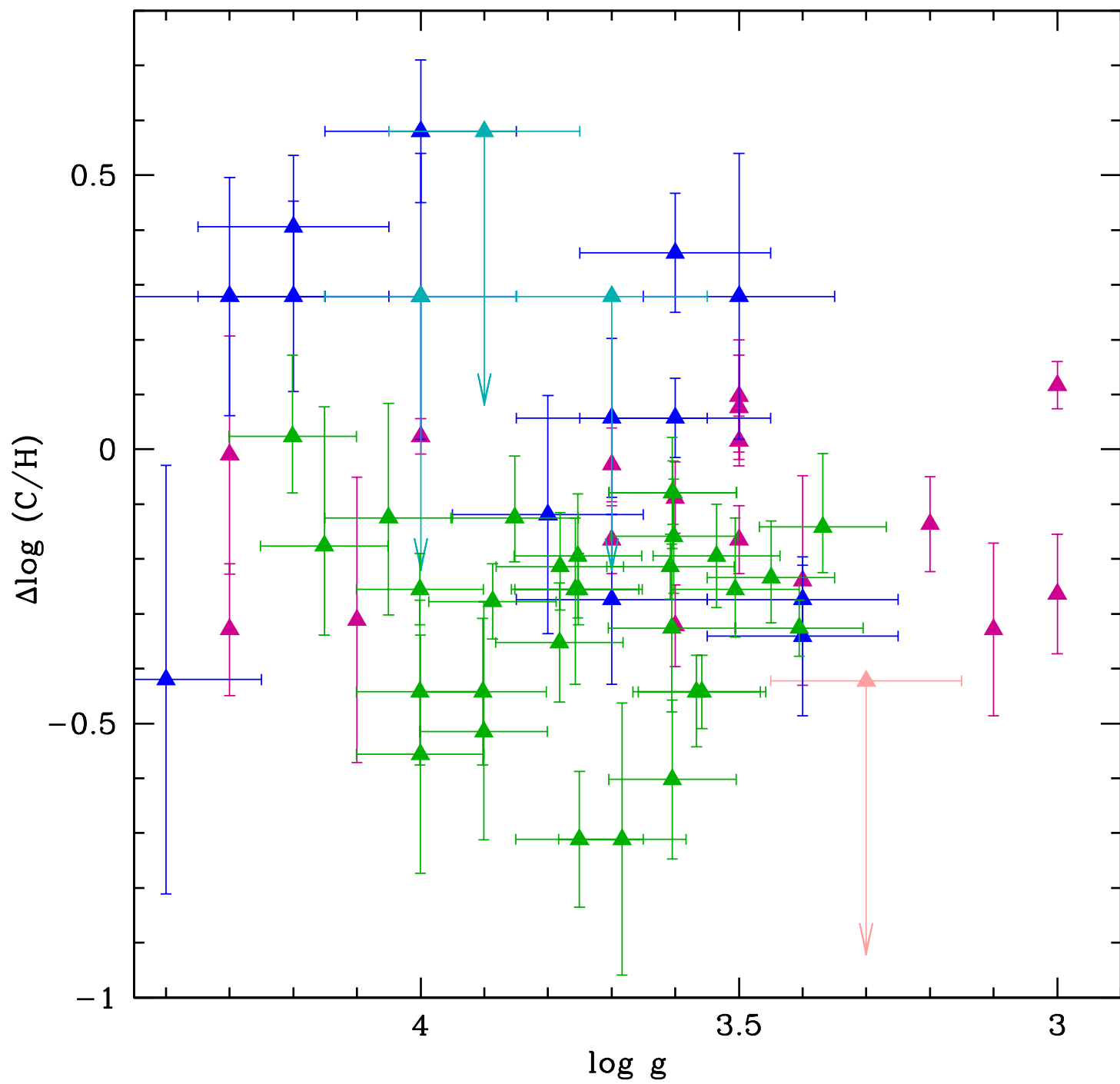
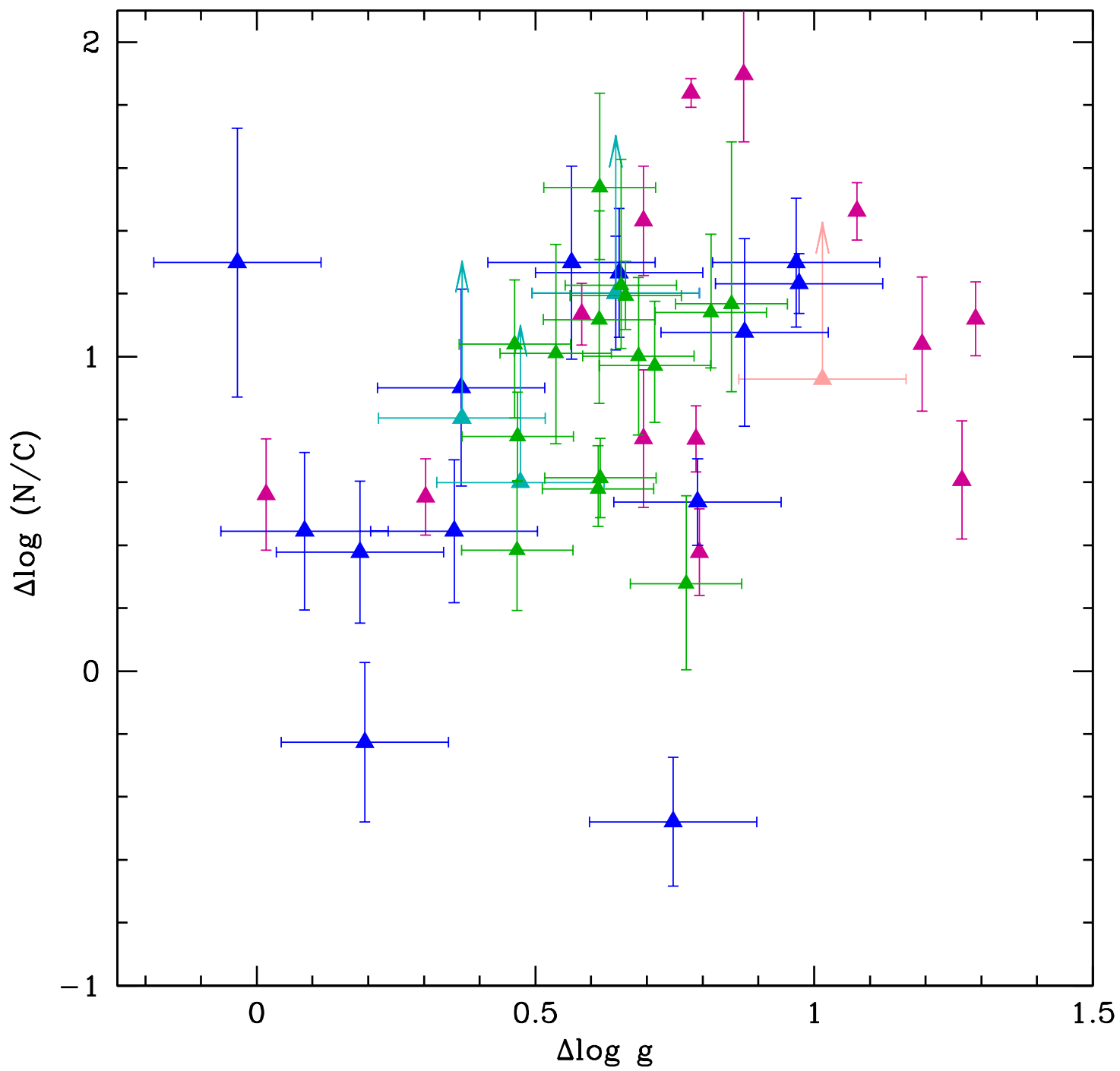
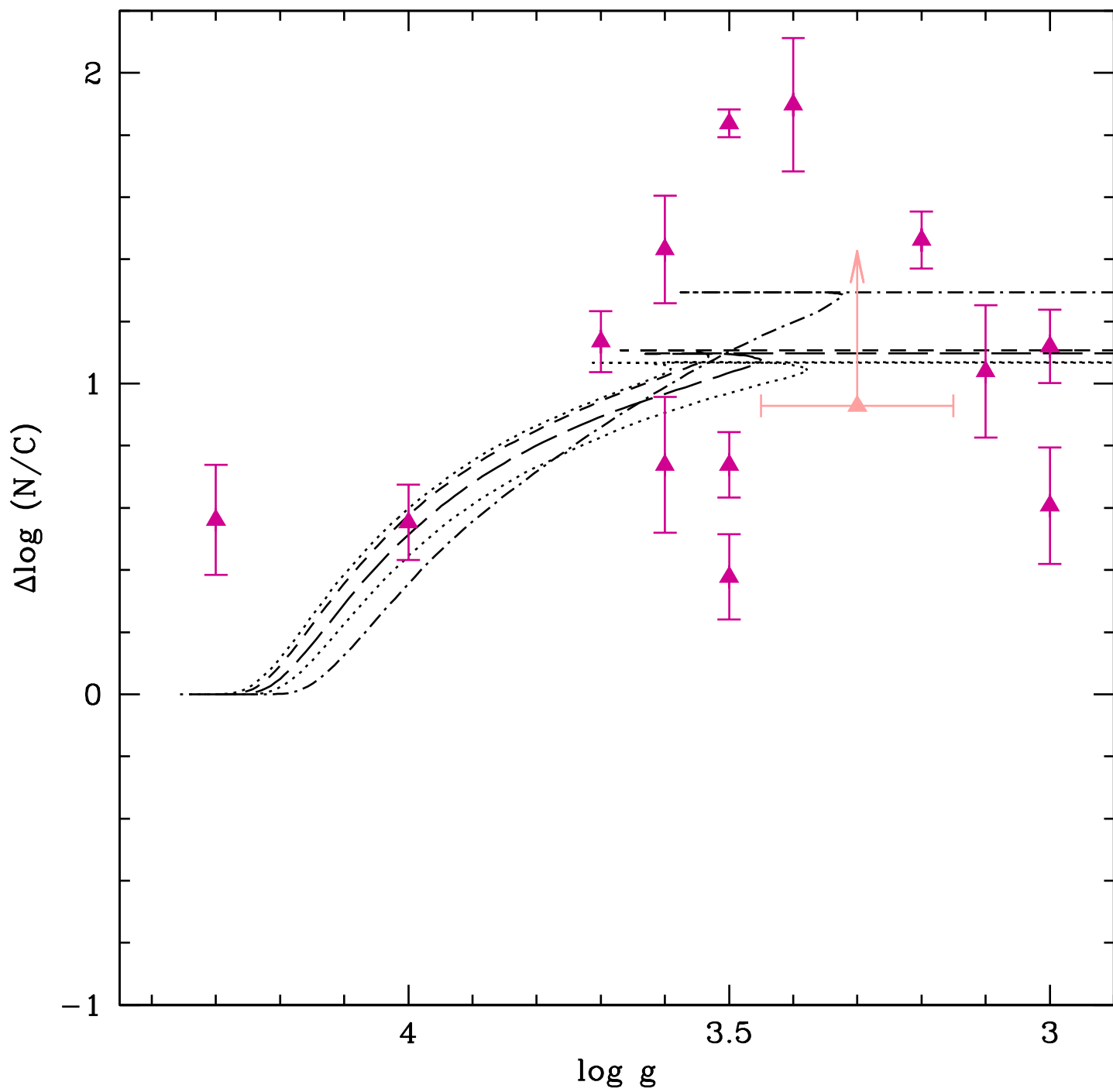
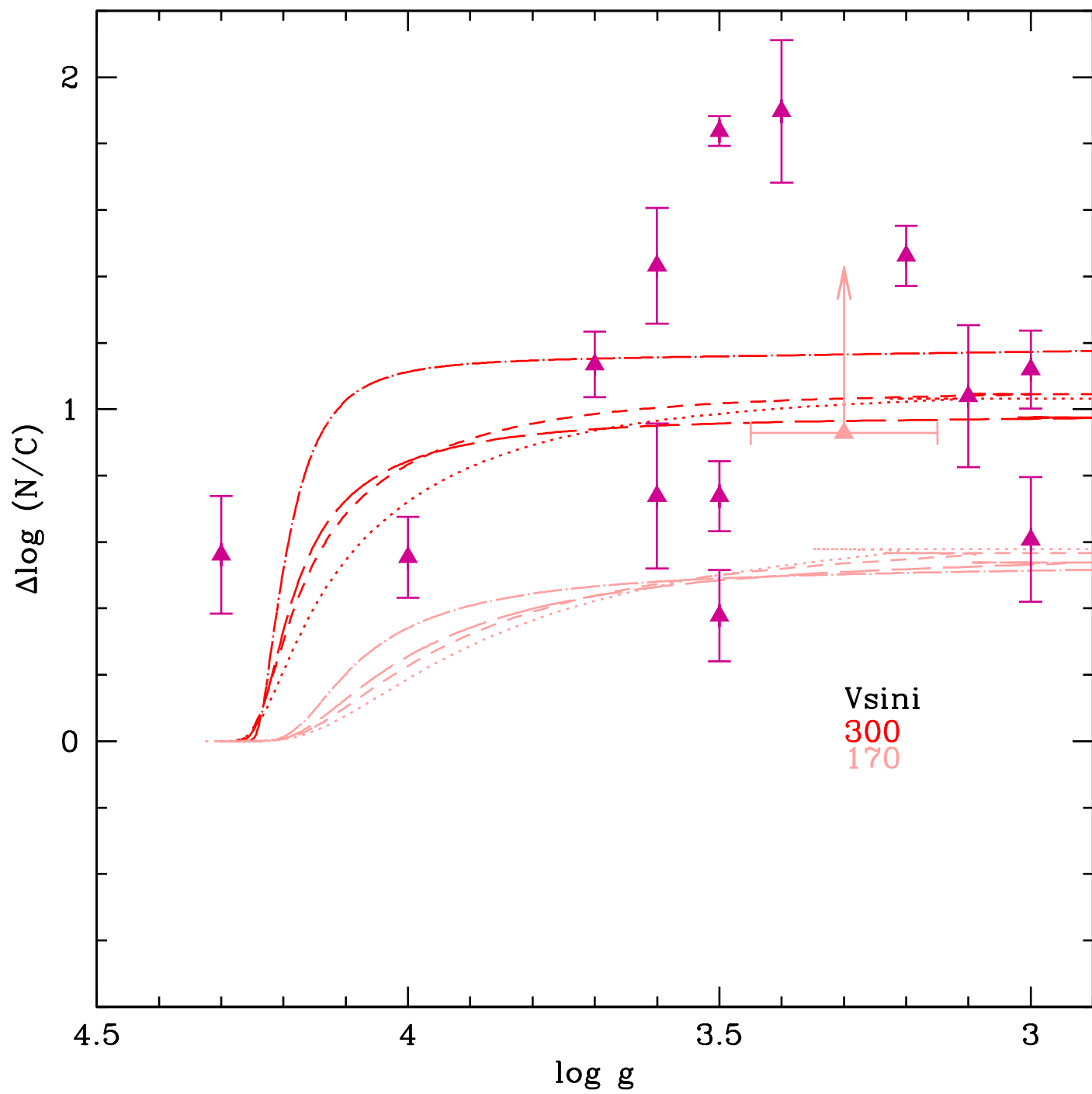


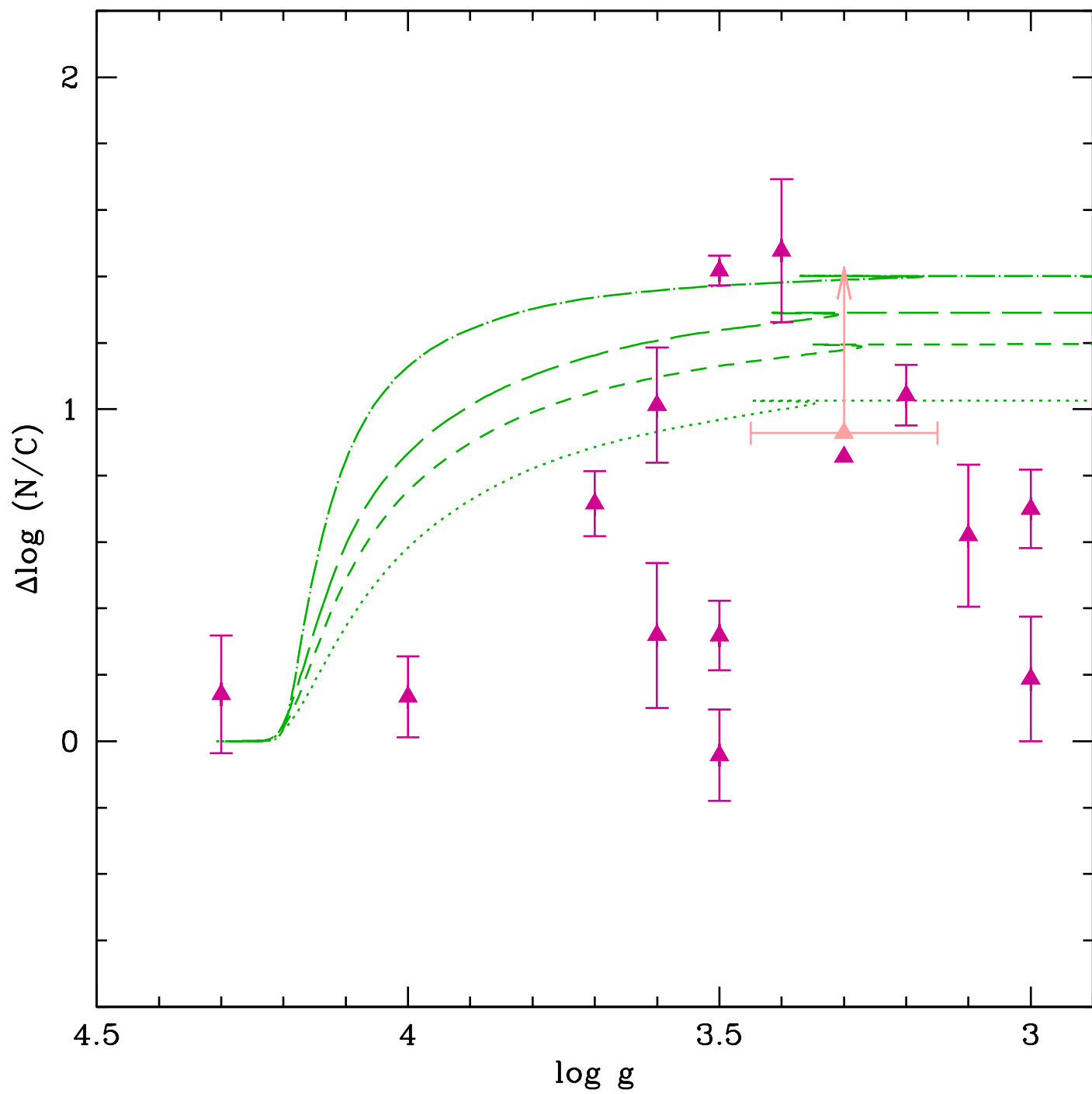
Fig. D.34. Same as Fig. D.2 but for BI 128.

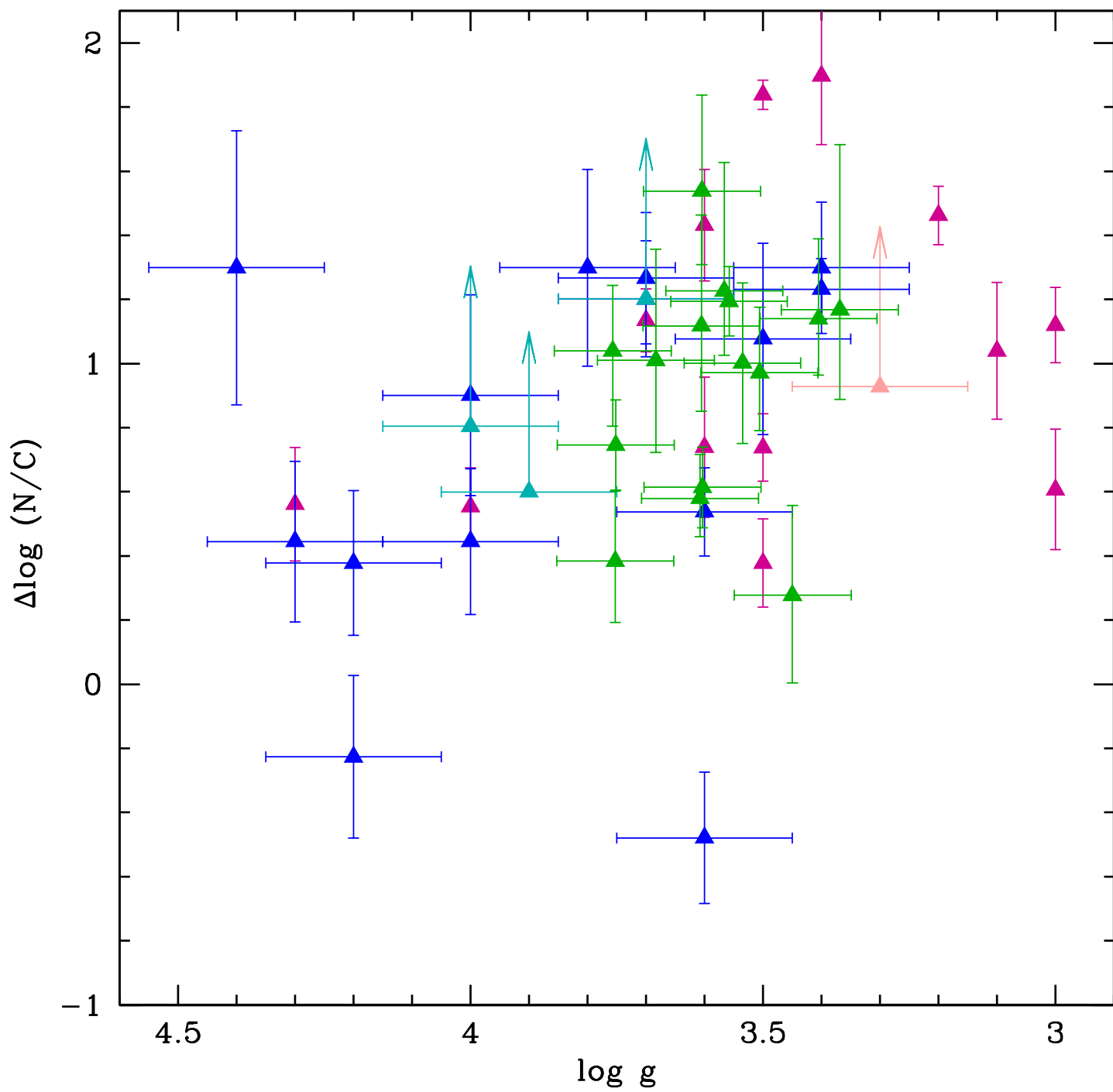


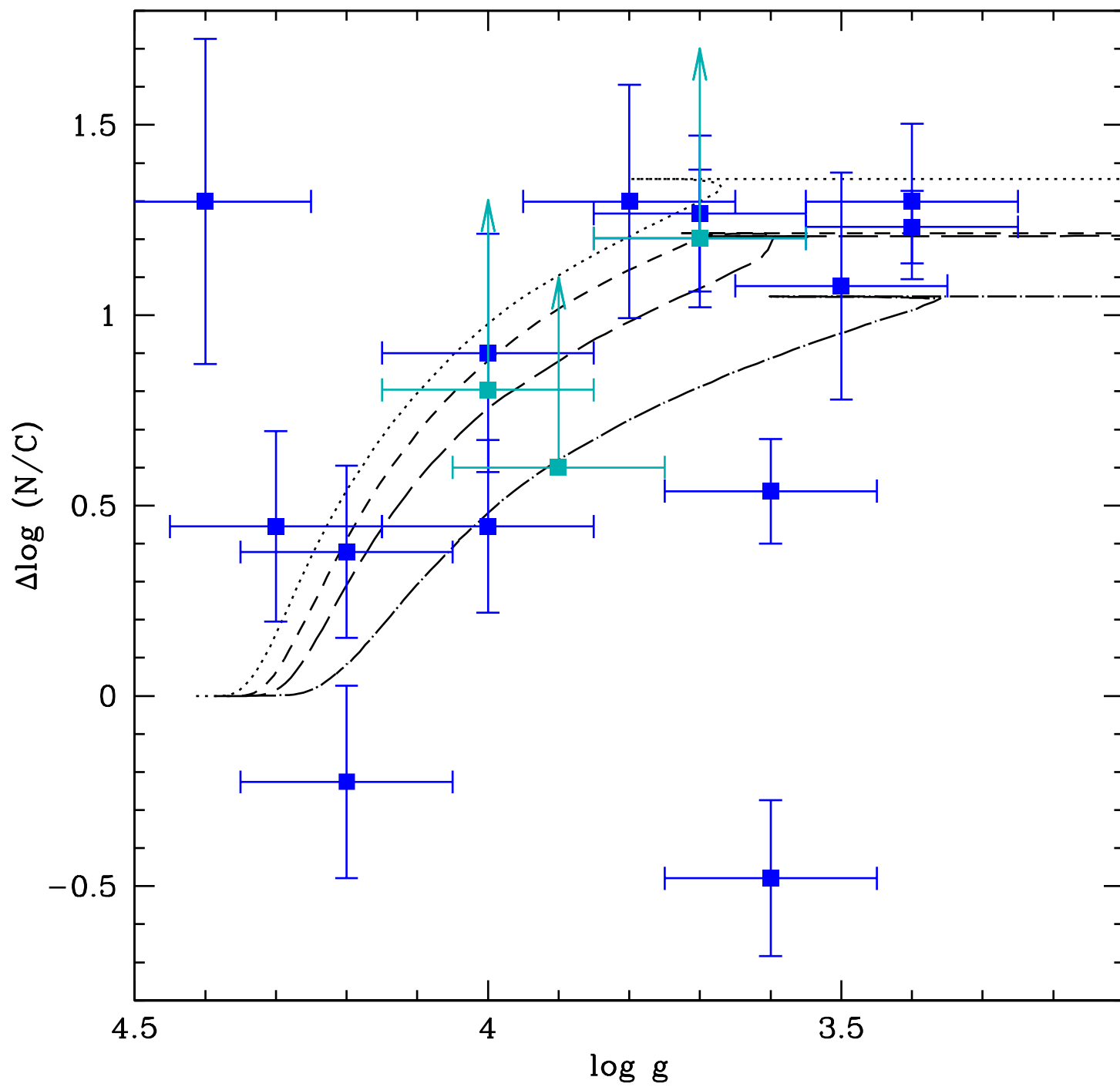


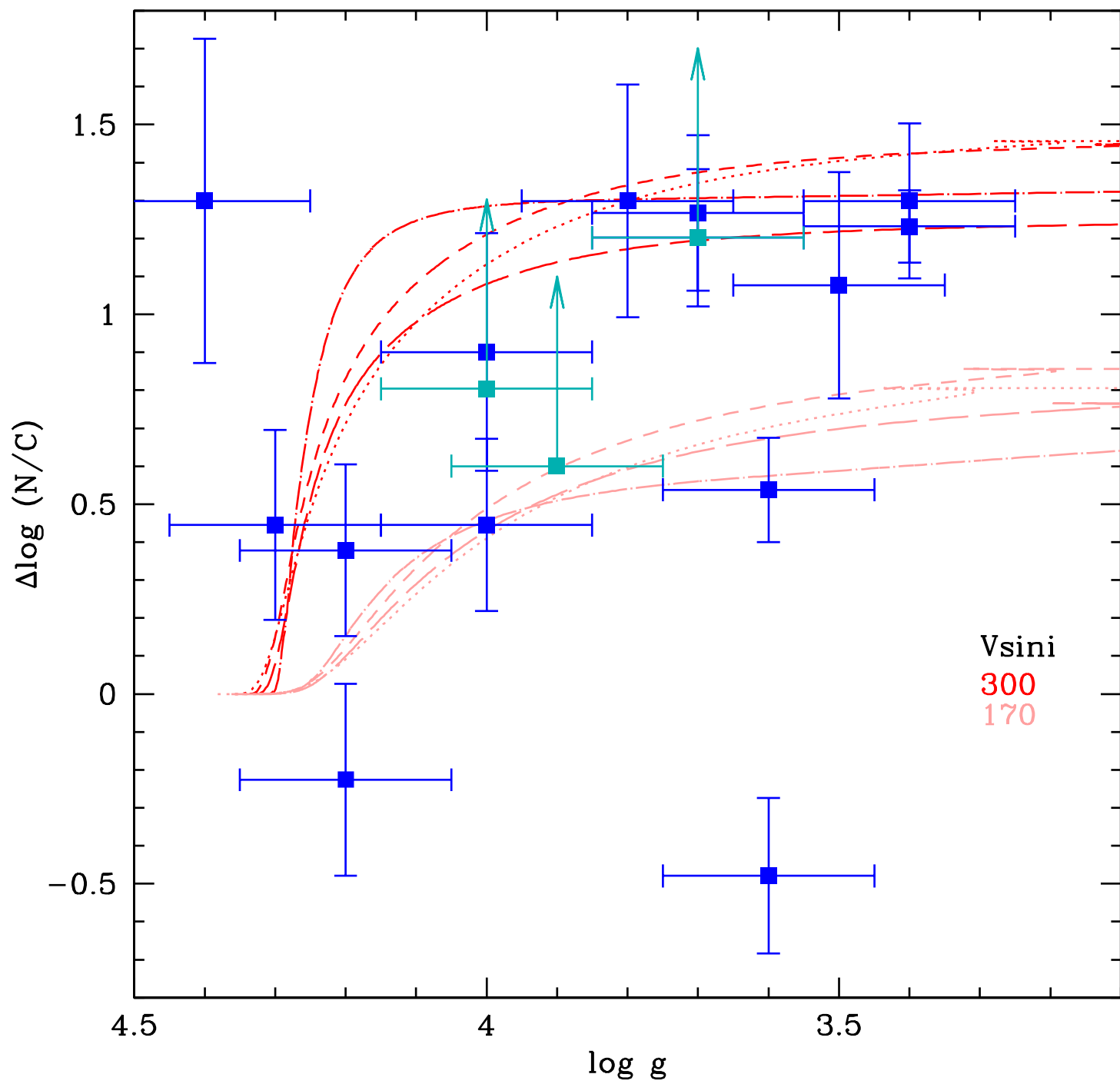


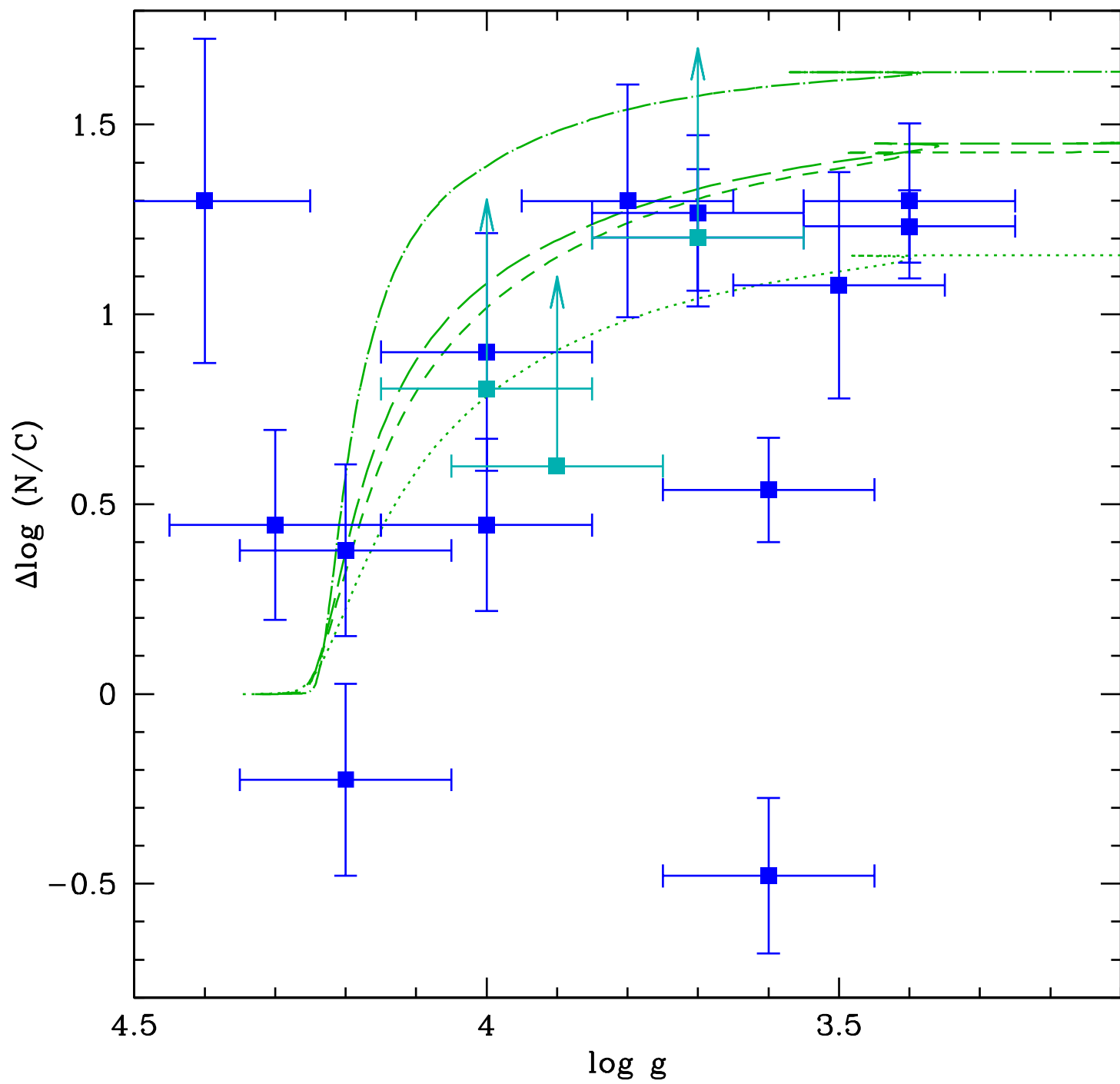


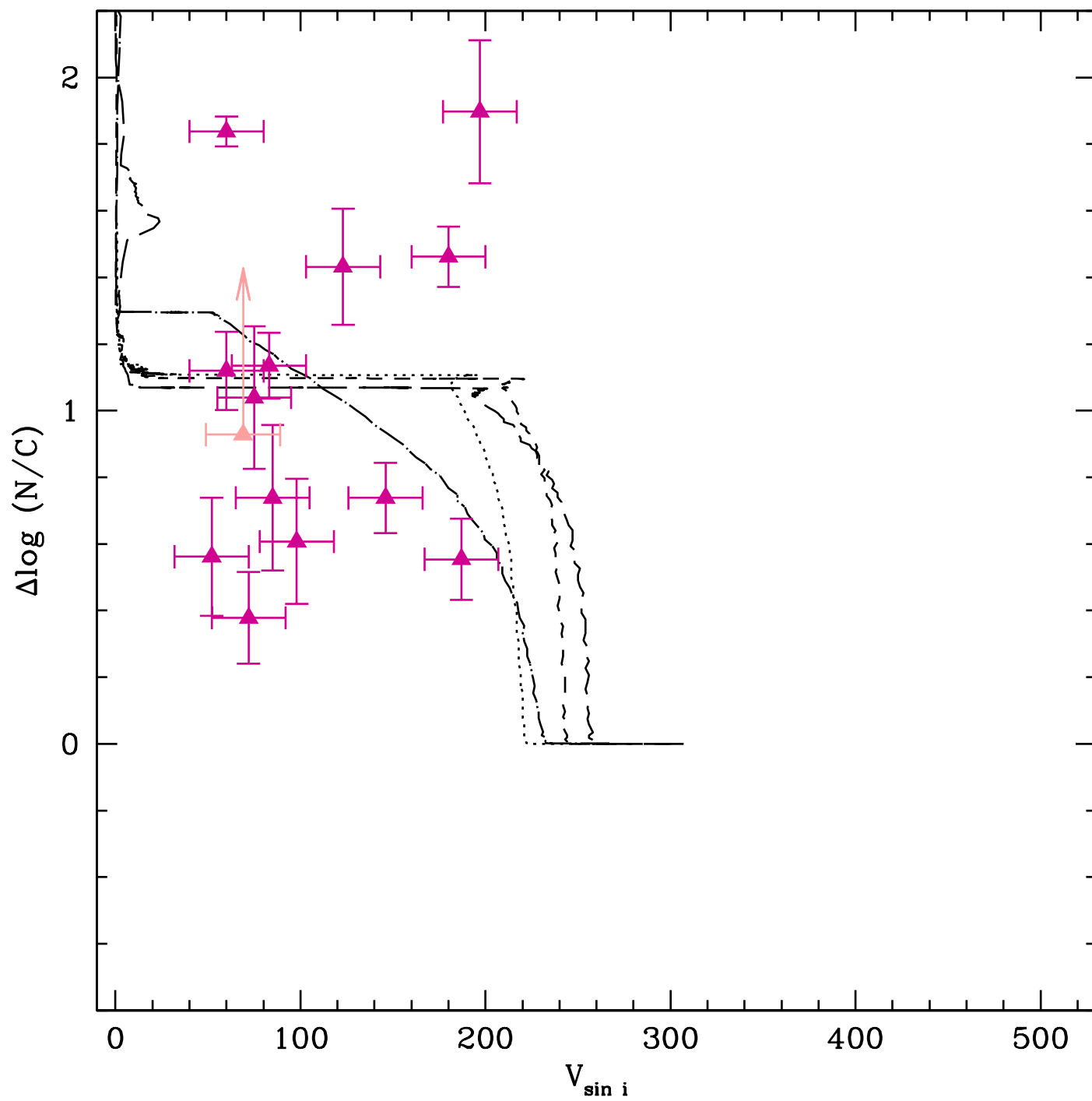


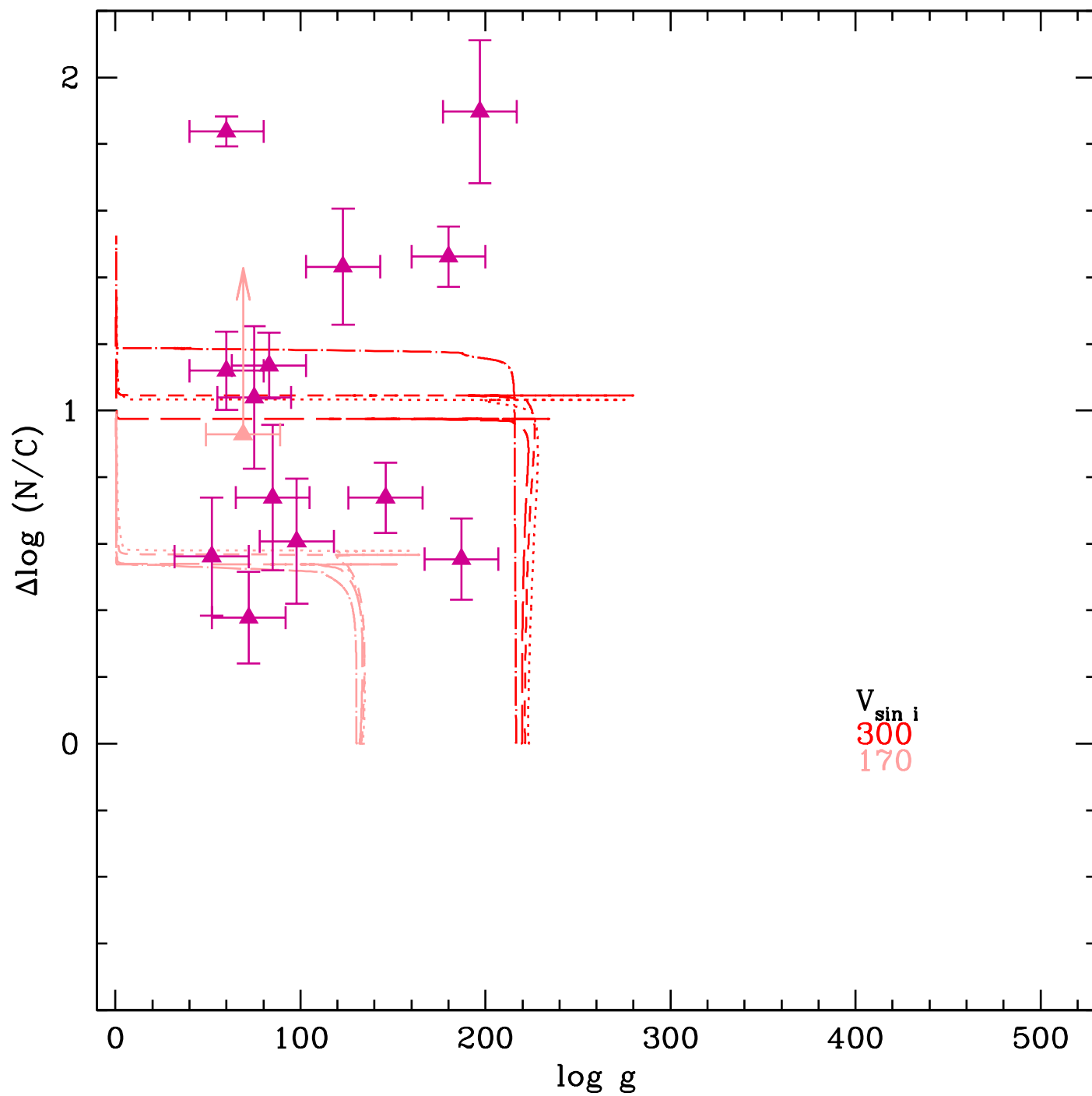


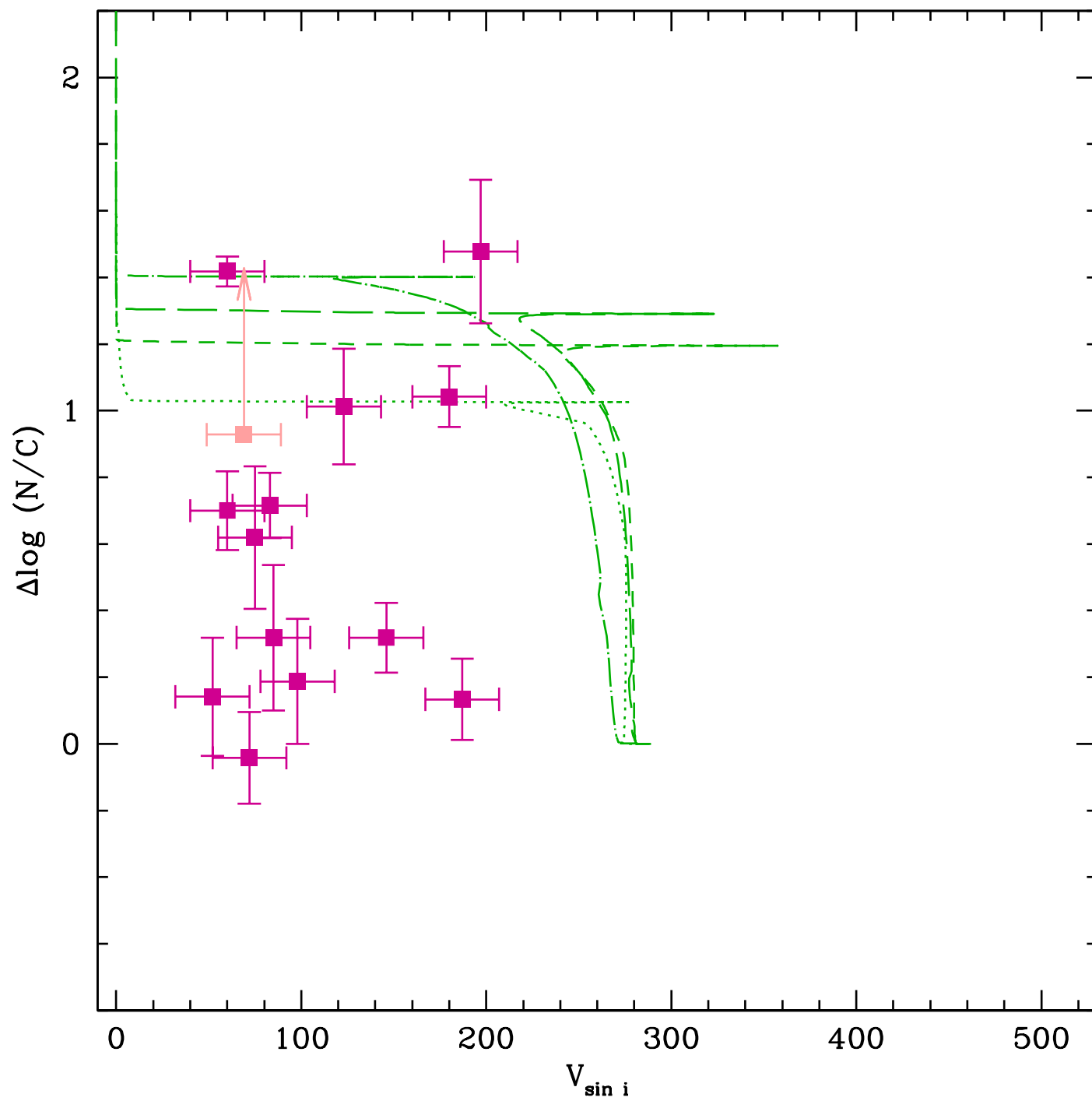


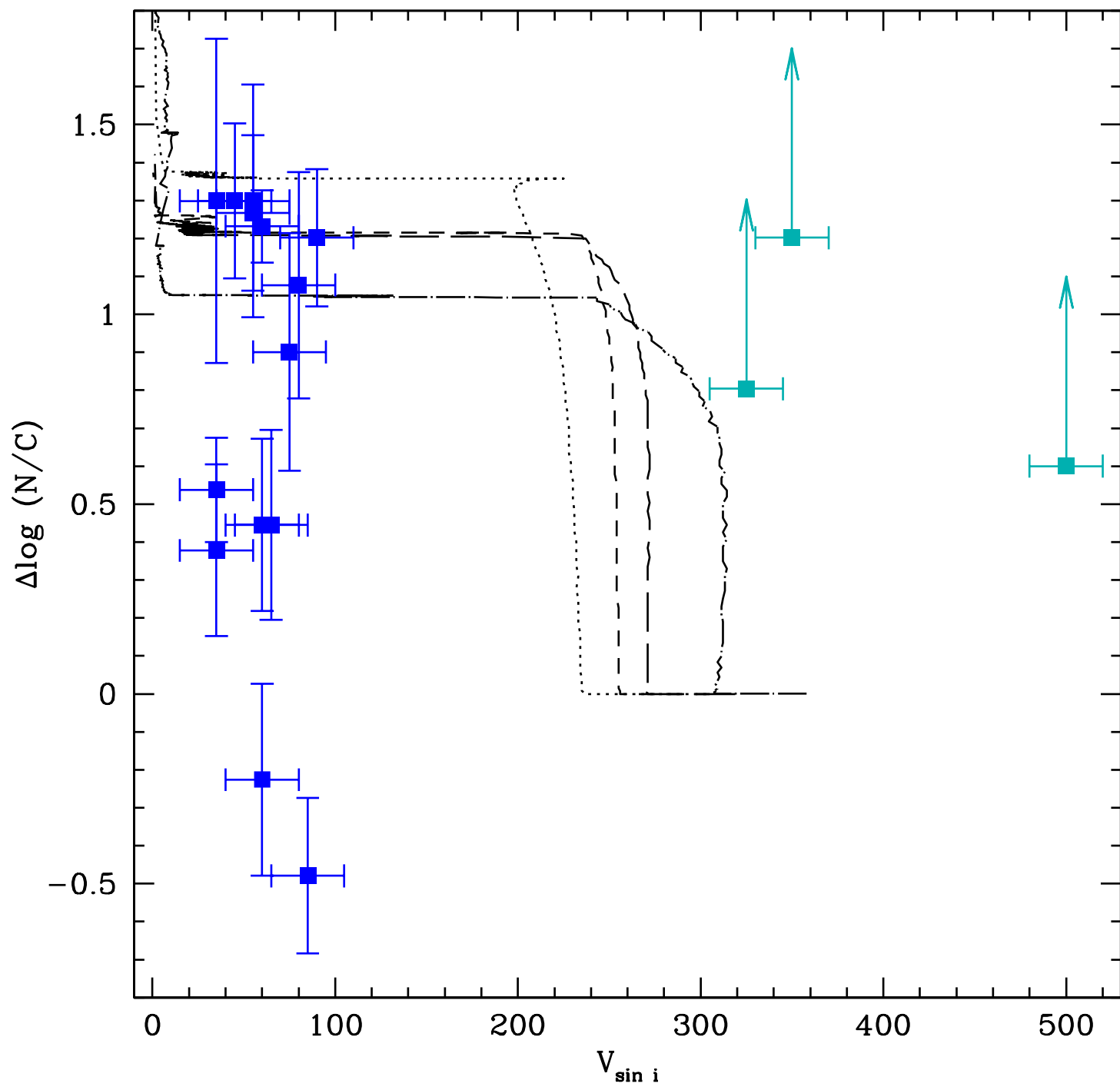


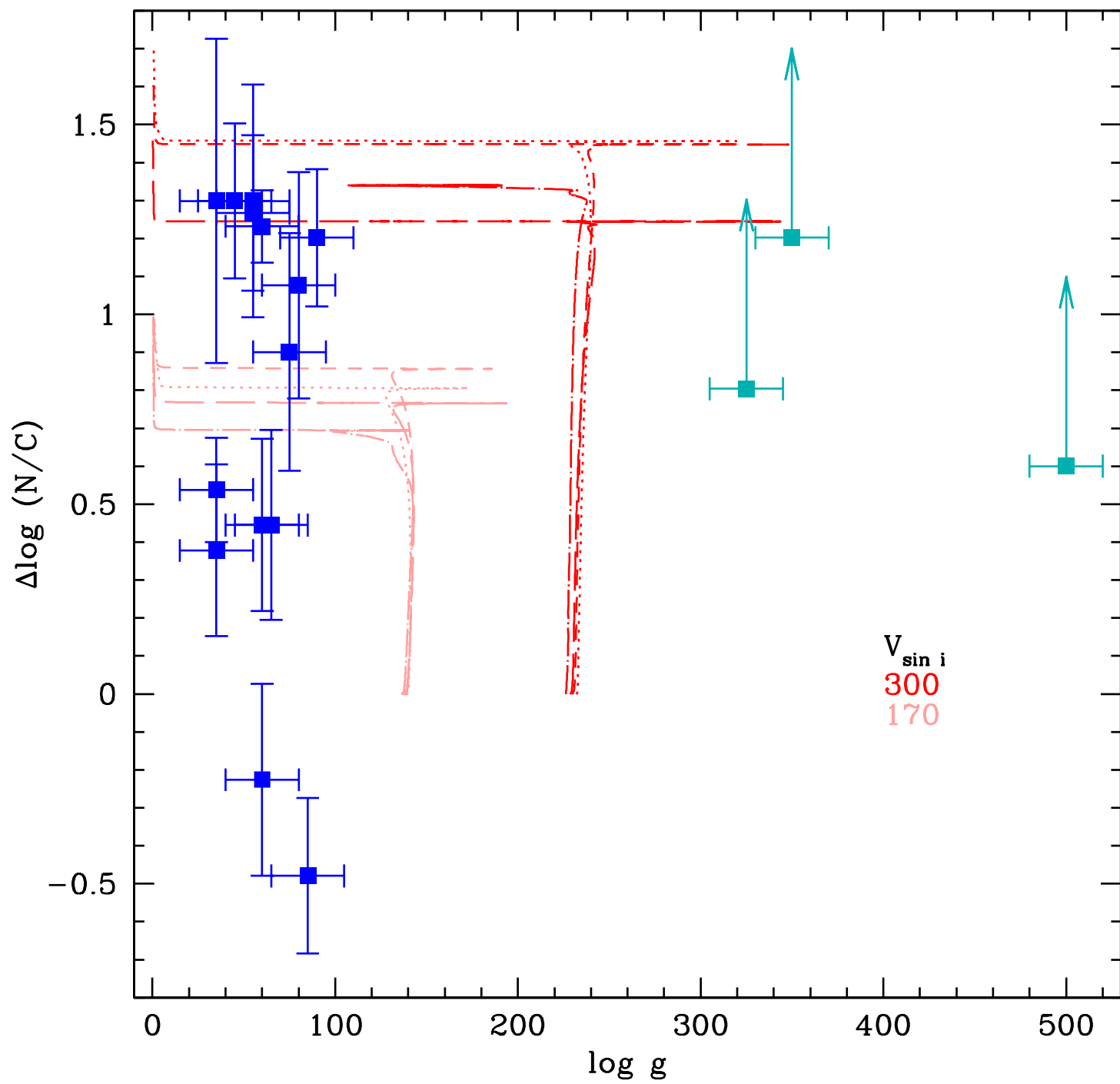


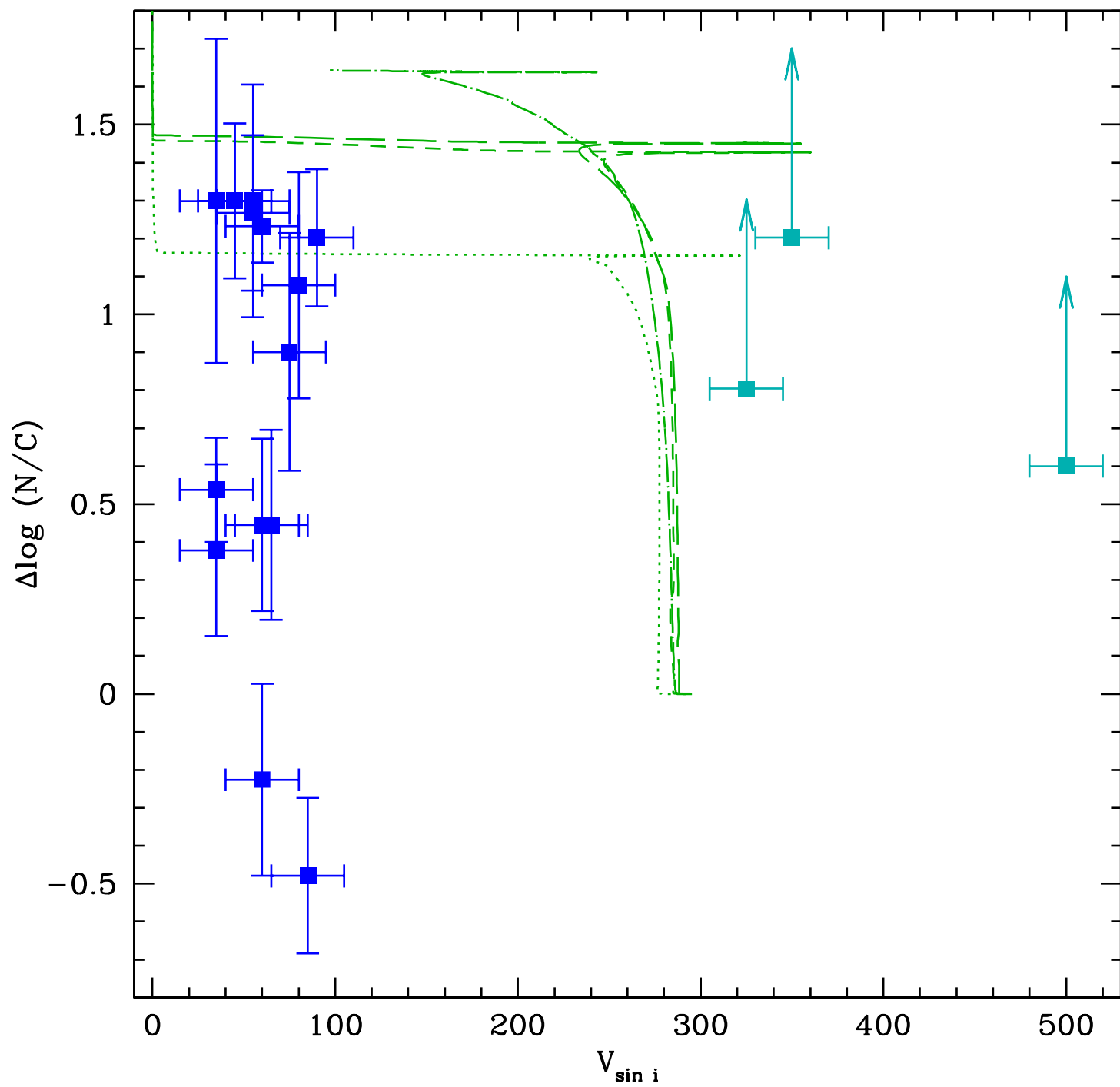


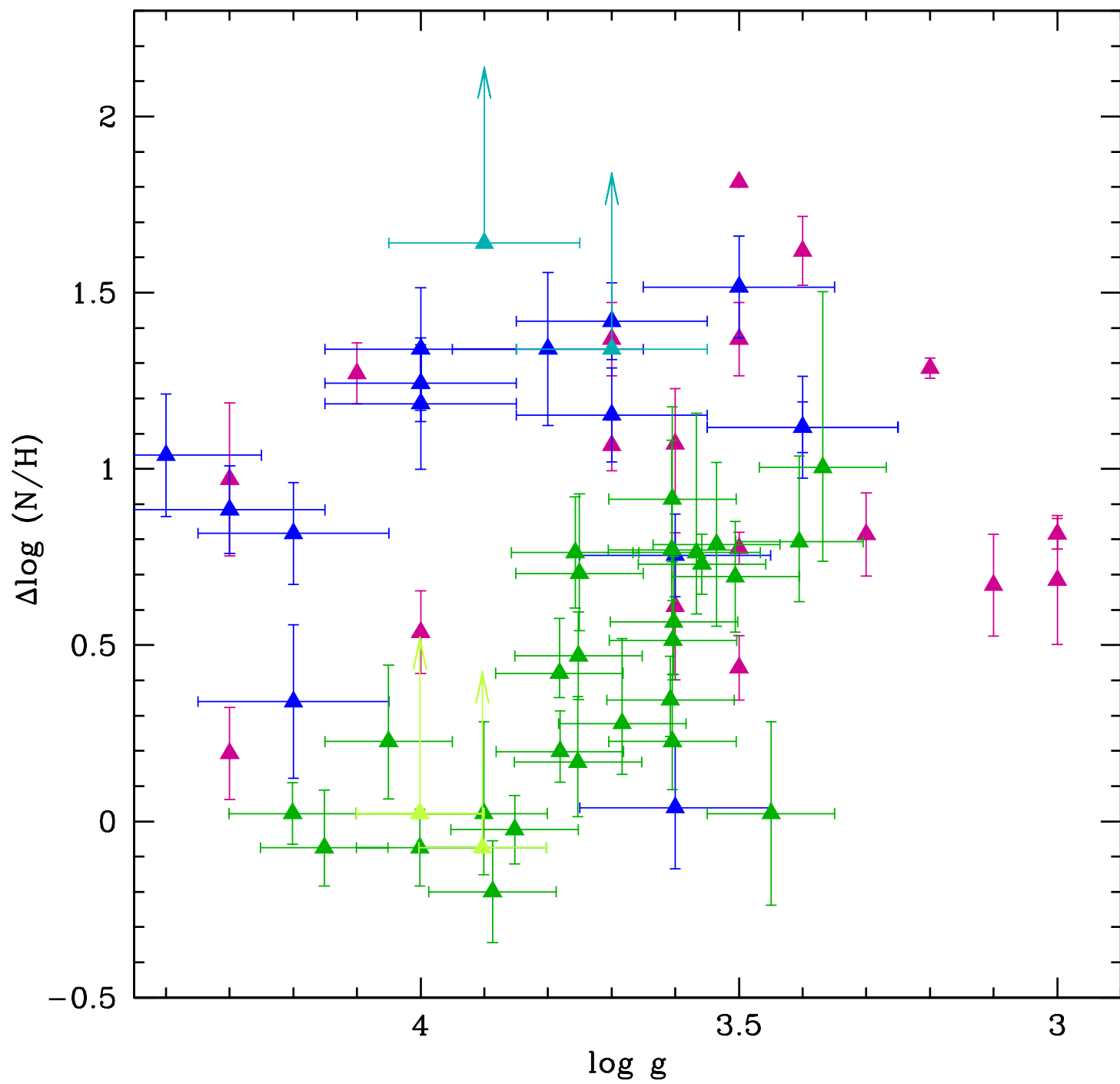


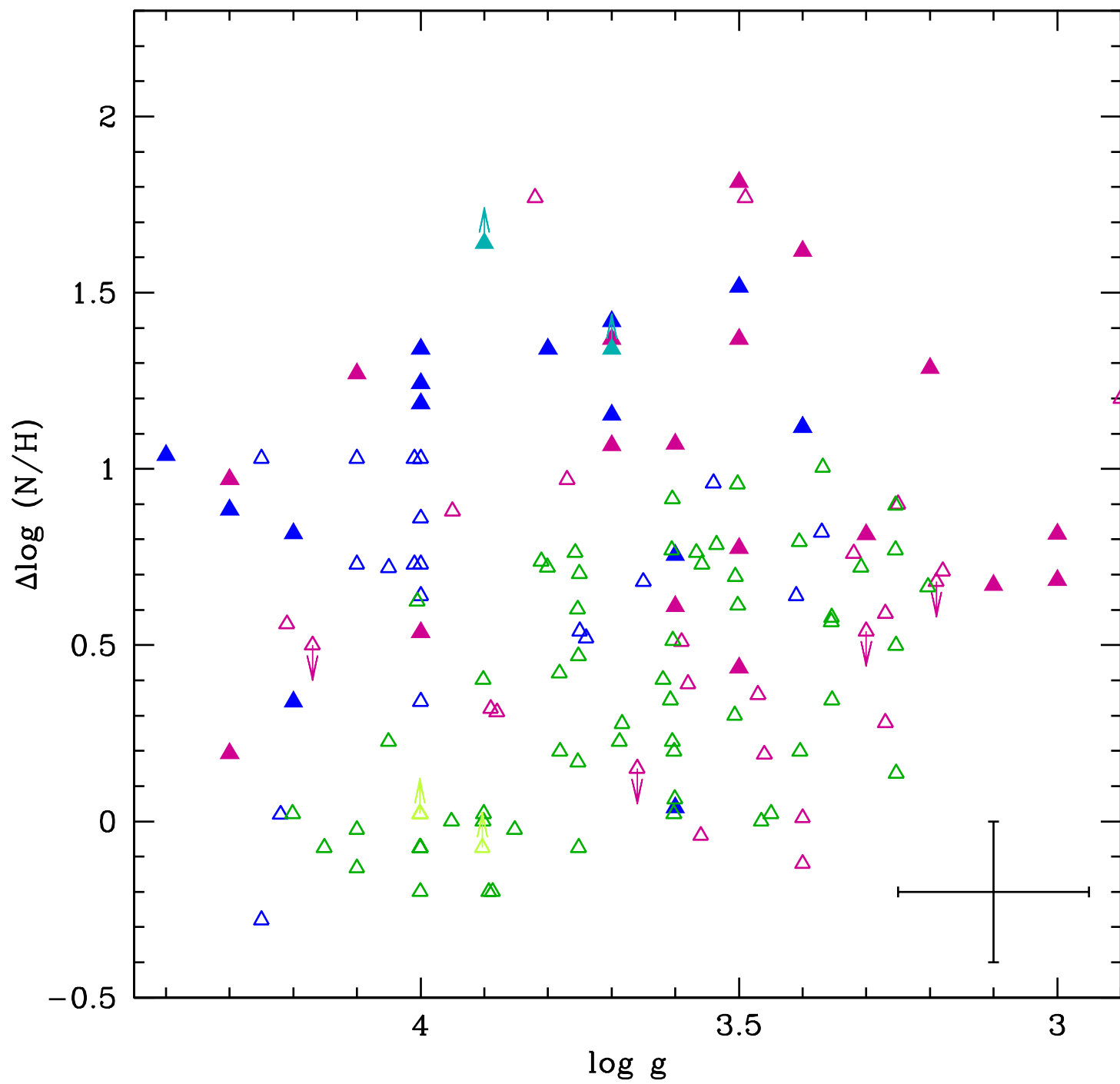


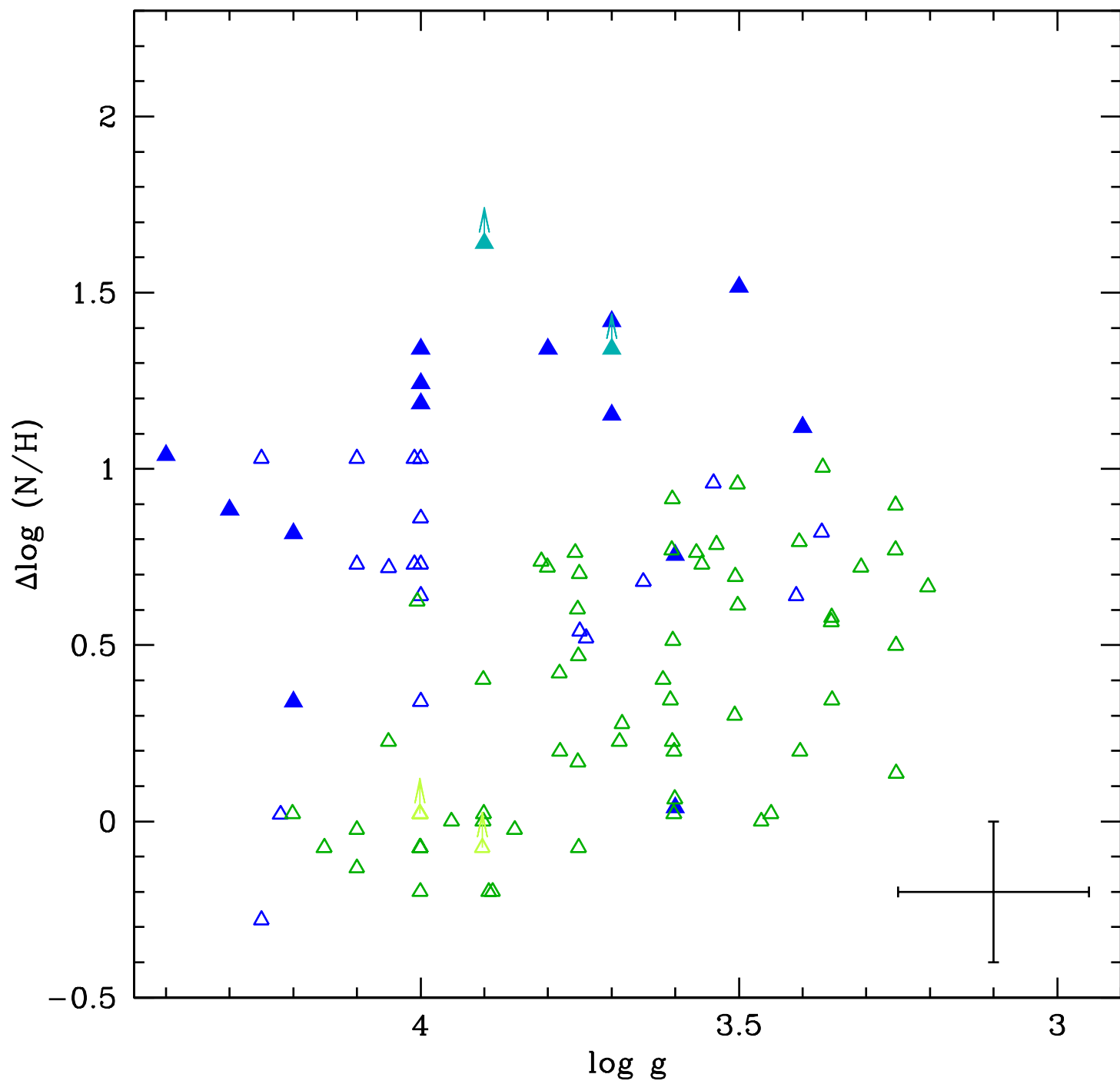


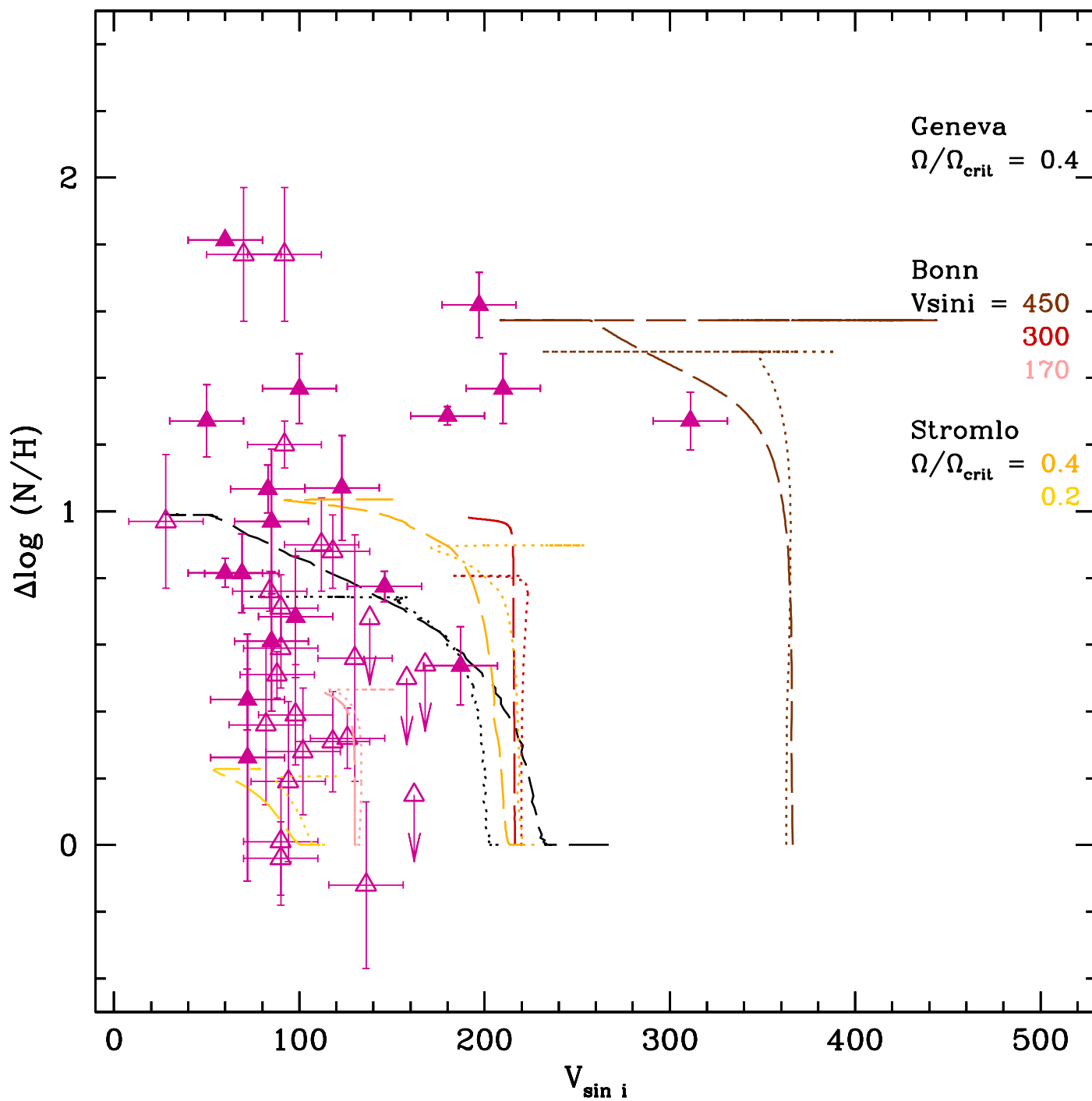


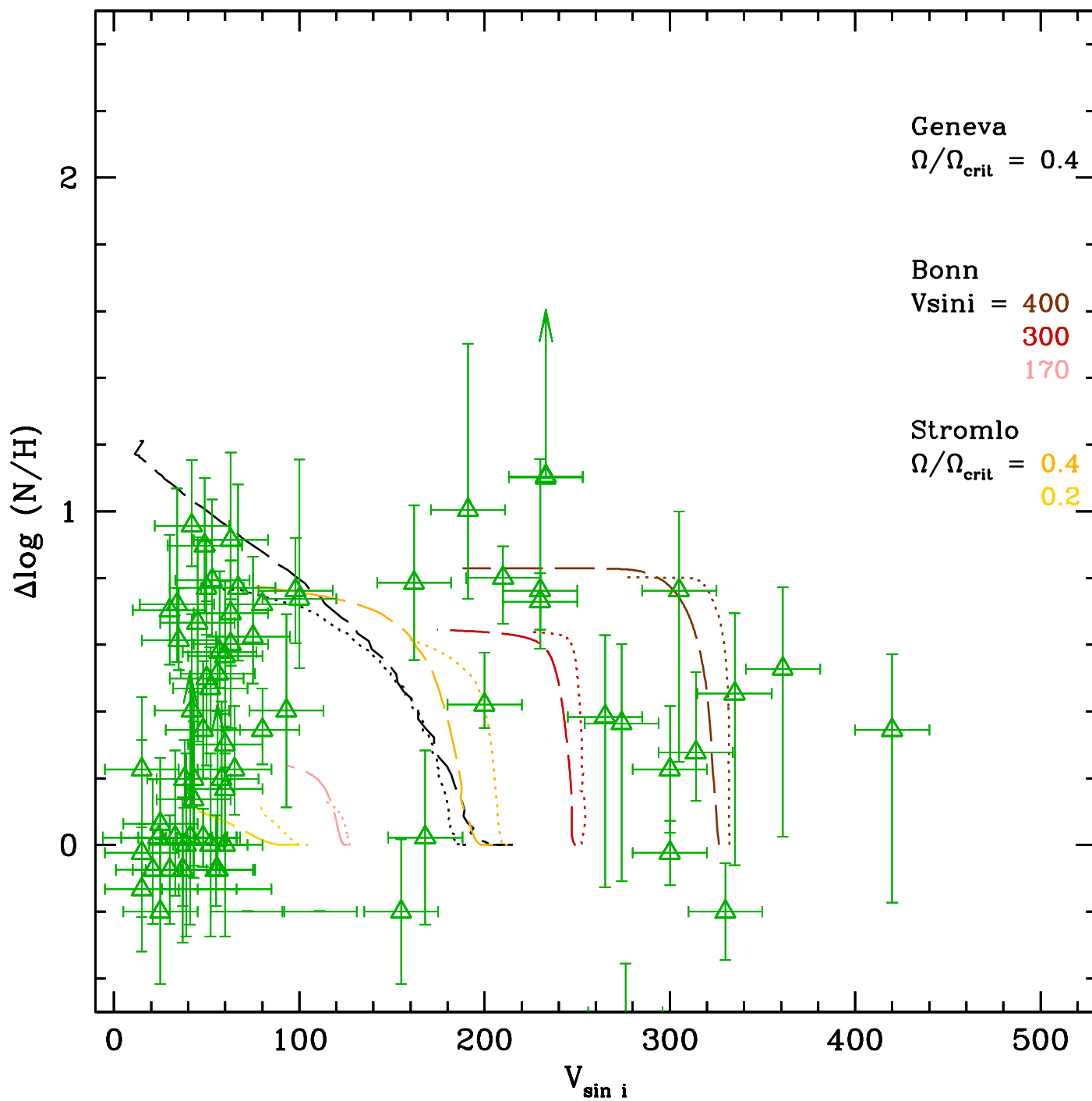


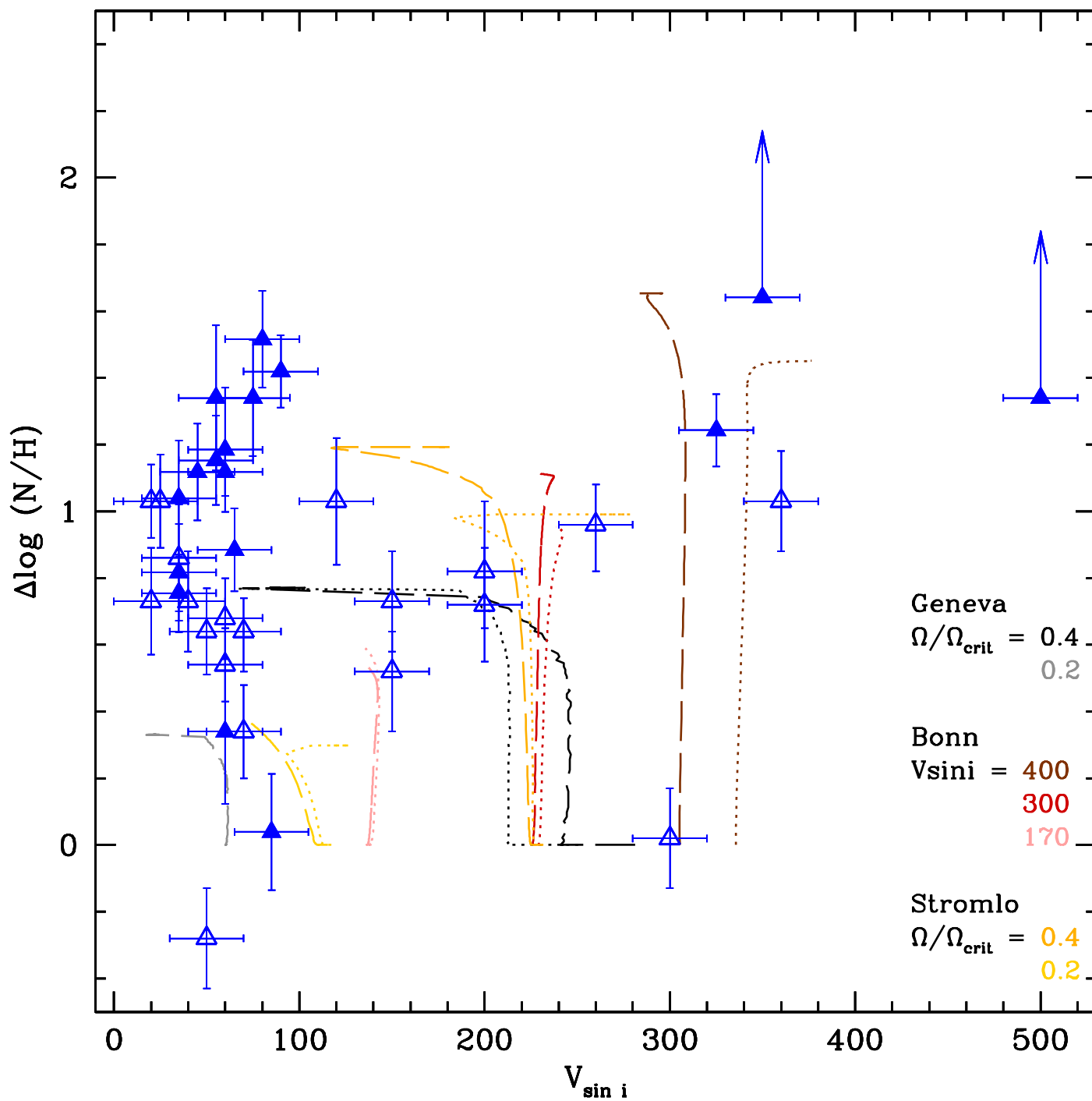


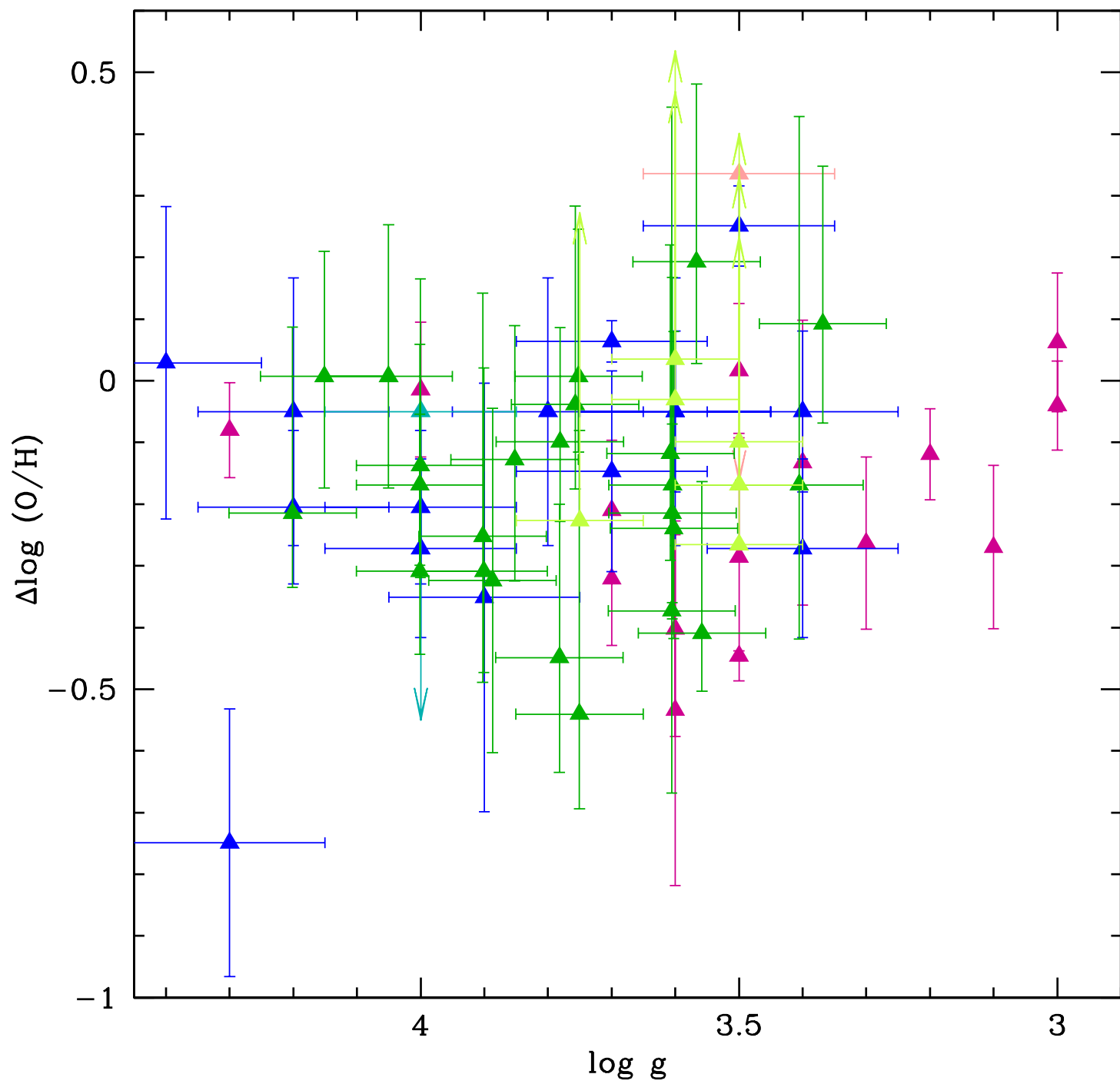


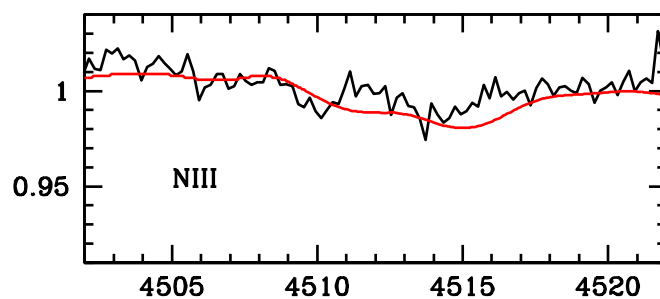
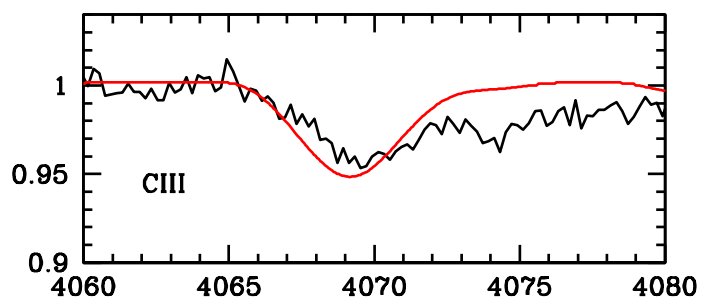
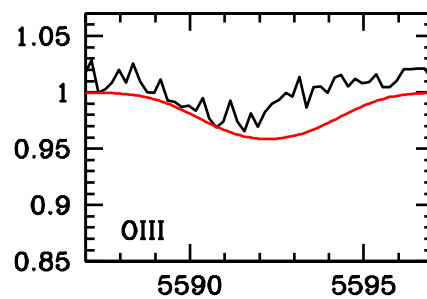
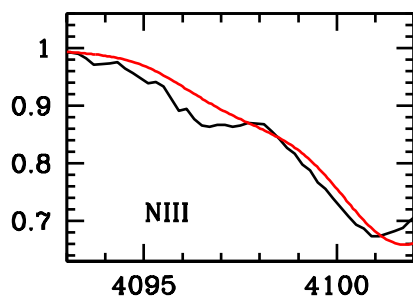
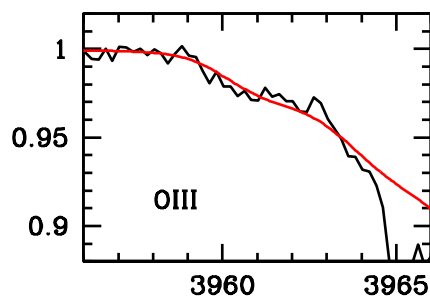
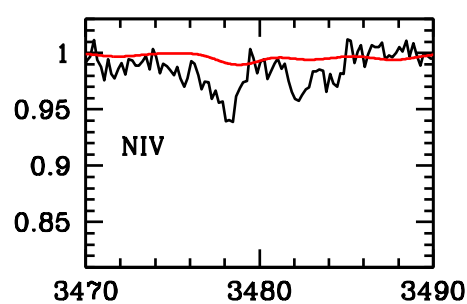
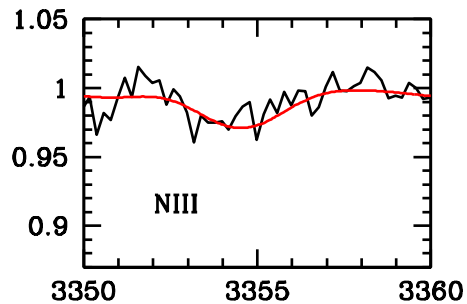
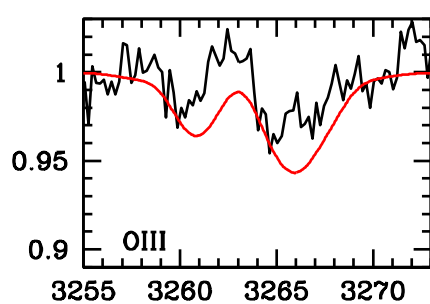
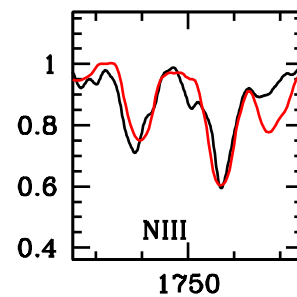
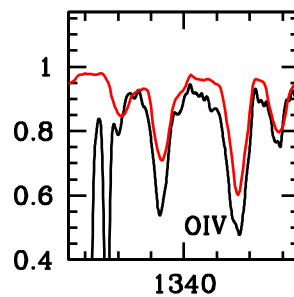
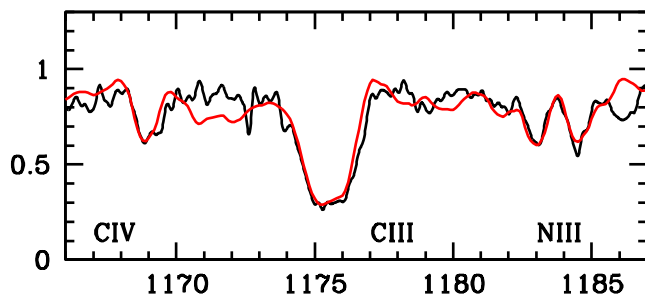












This figure "fit_av207_hst.png" is available in "png" format from:

<http://arxiv.org/ps/2405.01267v1>

This figure "fit_av207_xshooUVB.png" is available in "png" format from:

<http://arxiv.org/ps/2405.01267v1>

This figure "fit_av207_xshooVIS.png" is available in "png" format from:

<http://arxiv.org/ps/2405.01267v1>

